NAVAL POSTGRADUATE SCHOOL
Monterey, California

AD-A153 777

THESIS

A NUMERICAL STUDY OF THE PACIFIC POLAR LOW

by

Richard M. Hodur

December 1984

Thesis Advisors: R. T. Williams
                                    R. L. Elsberry

Approved for public release; distribution unlimited

85 04

REPORT DOCUMENTATION PAGE		READ INSTRUCTIONS BEFORE COMPLETING FORM
1. REPORT NUMBER	2. GOVT ACCESSION NO. AD-A153977	3. RECIPIENT'S CATALOG NUMBER
4. TITLE (and Subtitle) A Numerical Study of the Pacific Polar Low		5. TYPE OF REPORT & PERIOD COVERED Doctoral Dissertation December 1984
		6. PERFORMING ORG. REPORT NUMBER
7. AUTHOR(s) Richard M. Hodur		8. CONTRACT OR GRANT NUMBER(s)
9. PERFORMING ORGANIZATION NAME AND ADDRESS Naval Postgraduate School Monterey, CA 93943-5100		10. PROGRAM ELEMENT, PROJECT, TASK AREA & WORK UNIT NUMBERS
11. CONTROLLING OFFICE NAME AND ADDRESS Naval Postgraduate School Monterey, CA 93943-5100		12. REPORT DATE December 1984
		13. NUMBER OF PAGES 187
14. MONITORING AGENCY NAME & ADDRESS(If different from Controlling Office)		15. SECURITY CLASS. (of this report) UNCLASSIFIED
		15a. DECLASSIFICATION/DOWNGRADING SCHEDULE

16. DISTRIBUTION STATEMENT (of this Report)

Approved for public release; distribution unlimited

17. DISTRIBUTION STATEMENT (of the abstract entered in Block 20, If different from Report)

18. SUPPLEMENTARY NOTES

19. KEY WORDS (Continue on reverse side If necessary and Identify by block number)

Numerical Weather Prediction
Polar Lows
Linear Growth Rates

20. ABSTRACT (Continue on reverse side If necessary and Identify by block number)

A numerical study is performed to test the hypothesis that the Pacific polar low forms primarily through baroclinic instability. Linear growth rates computed for a jet profile typical of conditions during the formation of Pacific polar lows yields a growth rate maximum at 1400 km. Although the horizontal scale of this disturbance agrees with observations of the Pacific polar low, this disturbance is shallower and

DD FORM 1473 1 JAN 73   EDITION OF 1 NOV 65 IS OBSOLETE
S N 0102-LF-014-6601

1

Block 20 (Abstract continued)

forms further north relative to the jet than indicated by observations. Nonlinear simulations of the 1400 km disturbance indicate that the effects of convection and surface heat and and moisture fluxes due to initially large air-sea temperature differences are needed for proper vertical structure, storm position and intensification. Energy budgets of model output indicate that the wave grows through baroclinic instability and that the diabatic effects enhance the baroclinic conversion within the storm.

COPY
INSPECTED
1

Accession For

NTIS GRA&I	☑
DTIC TAB	☐
Unannounced	☐
Justification	

Distribution/
Availability Codes

| | Avail and/or |
| Dist | Special |

A-1

A Numerical Study of the Pacific Polar Low

by

Richard M. Hodur
B.S., Northern Illinois University, 1973
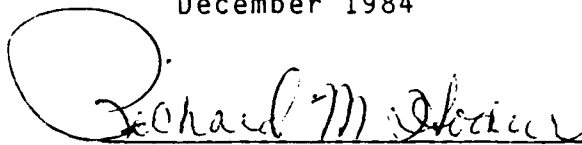M.S., University of Oklahoma, 1975

Submitted in partial fulfillment of the
requirements for the degree of
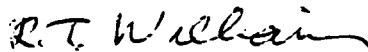
DOCTOR OF PHILOSOPHY

from the
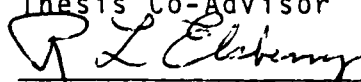
NAVAL POSTGRADUATE SCHOOL
December 1984

Author: _____
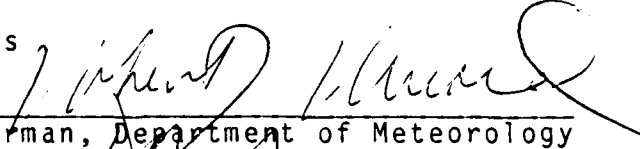
Approved by:

R. T. Williams
Professor of Meteorology
Thesis Co-Advisor

C. H. Wash
Associate Professor of
Meteorology
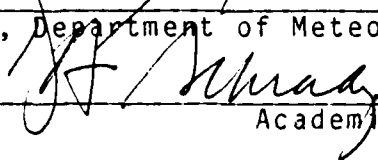
R. L. Elsberry
Professor of Meteorology
Thesis Co-Advisor

D. Salinas
Associate Professor of
Mechanical Engineering

F. D. Faulkner
Distinguished Professor
Emeritus of Mathematics

Approved by: _____
Chairman, Department of Meteorology

Approved by: _____
Academic Dean

3

ABSTRACT

A numerical study is performed to test the hypothesis
that the Pacific polar low forms primarily through baro-
clinic instability./ Linear growth rates computed for a
jet profile typical of conditions during the formation of
Pacific polar lows yields a growth rate maximum at 1400 km.
Although the horizontal scale of this disturbance agrees
with observations of the Pacific polar low, this disturbance
is shallower and forms further north relative to the jet
than indicated by observations. Nonlinear simulations of
the 1400 km disturbance indicate that the effects of convec-
tion and surface heat and moisture fluxes due to initially
large air-sea temperature differences are needed for proper
vertical structure, storm position and intensification.
Energy budgets of model output indicate that the wave grows
through baroclinic instability and that the diabatic effects
enhance the baroclinic conversion within the storm.

4

TABLE OF CONTENTS

5

LIST OF TABLES

LIST OF FIGURES

7

8

11

The second jet, referred to as the genesis jet, is typical of conditions during the genesis period of northeastern Pacific polar lows (Mullen, 1979). Mullen (1979) defined this period to be "at the latest hour, either 0000 GMT or 1200 GMT, before the cloud mass in question showed any discernable comma or hook shape in the infrared (IR) imagery." Mullen composited NMC analyses for 22 northeastern Pacific polar lows. In all cases, the width of the cloud mass at the genesis period was at least 500 km. It was expected that this jet would be appropriate for studying the polar low.

The mean winter and genesis jets of Lau (1978) and Mullen (1979) were transformed to model coordinates in the following manner. First, the channel width of the model was chosen to be 6400 km with the jet core in the center of this channel. Second, at all mandatory levels up to 300 mb in the genesis jet and up to 100 mb in the mean winter jet, wind speeds were tabulated in 250 km increments over an interior 2500 km meridional slice. It was assumed that the zonal wind for both jets decreased linearly to zero at both the north and south walls. The shape of the genesis jet above 300 mb was assumed to resemble that of the mean winter jet. Third, these wind speeds were linearly interpolated on each mandatory pressure surface to the model horizontal grid points. Fourth, one pass with an 81 point smoother-desmoother (Shapiro, 1970) was applied to these fields to

25

II. NUMERICAL PROCEDURES

The NORAPS forecast model has several features which make it applicable for extensive numerical simulations. First, the domain size and the horizontal and vertical resolution in the model may be varied. Second, dynamics and physics appropriate to subsynoptic features are included as described in Appendix A. Exact values for various parameters are given in the description of each model experiment. A map factor of 1 is used over the entire domain for all forecasts. Also the Coriolis force, f, is calculated using the β-plane approximation,

$$f = f_0 + \beta_0 (y-y_0) \qquad (2.1)$$

A. INITIAL DATA

1. Initial Jet Profiles

Two baroclinically unstable jet profiles were chosen for this study. The first jet describes the mean winter conditions over the Pacific. The conditions were derived by Lau (1978), who composited National Meteorological Center (NMC) analyses from 850 to 100 mb for 11 winters in the sector from 150E to 150W and from 20N to 70N. Mullen (1979) included 1000 mb winds estimated by Crutcher and Meserve (1970). It was expected that this jet (referred to hereafter as the mean winter jet) would be appropriate for studying typical oceanic synoptic-scale lows.

also shows how barotropic and baroclinic instabilities contribute to the generation and destruction of the eddy kinetic energy of the most unstable waves.

The second major section, Chapter IV, describes nonlinear model simulations of the polar low. Detailed analyses of wave structure and energy budgets are presented for adiabatic and diabatic simulations. The sensitivity to the air-sea temperature difference is discussed.

To test this hypothesis, the numerical model used in the Fleet Numerical Weather Center's Navy Operational Regional Atmospheric Prediction System (NORAPS) is used (Appendix A). This model includes convective and non-convective precipitation processes and state-of-the-art planetary boundary layer (PBL) physics. In addition, the model may be run with various combinations of grid spacing and resolution. This makes the model quite useful for studying waves of various sizes.

Interpretation of model results is accomplished through budgets of kinetic and available potential energy as given in Robertson and Smith (1983). These equations (Appendix B) are split into zonal and eddy components and the exact form of the available potential energy is used. Since the forecast model uses a closed domain, the eddy components can be directly related to a single wave in the forecast domain.

This study consists of two major sections. The first, Chapter III, describes linear growth rates computed using a linearized version of the NORAPS model. Two sets of initial conditions are used. The first is a mean winter jet and the second is a jet typical of conditions during the development of Pacific polar lows. Small perturbations are introduced into the initial fields and an adiabatic version of the model is integrated while restoring the initial mean zonal fields every time step. The effects of linearized friction and wave-zonal flow interaction are discussed. This section

22

Gall (1976c) demonstrated that convection can serve to increase the vertical extent of medium-scale (2000 km) waves.

Surface fluxes of heat and moisture also must be considered since large air-sea temperature differences are often associated with Pacific polar lows (Mullen, 1979). Large upward fluxes of heat can reduce the low-level static stability which, as explained above, can result in baroclinically unstable 1000 km waves. The role of surface fluxes in strengthening disturbances has been discussed by Petterssen (1956), Danard and Rao (1972) and Forbes and Merritt (1984).

Based on the observational and analytic studies described above, the major hypothesis of this study is that Pacific polar lows are formed primarily through baroclinic instability. They are a preferred mode, especially in winter, because of the unique vertical temperature profile forced by a polar air mass moving over relatively warm water. The upward sensible heat flux in the polar air reduces the low-level static stability and therefore, R_i. This is precisely what is needed to set up baroclinically unstable waves on the scale of the Pacific polar low according to the theoretical studies discussed above. It is also hypothesized that surface fluxes and latent heat release through convection modify the baroclinic wave by further intensifying it and increasing its vertical extent.

tends to shift the maximum growth rate to shorter wave-
lengths (Gambo, 1970a; Tokioka, 1970; Mansfield, 1974; Gall,
1976a; Duncan, 1977; Staley and Gall, 1977). However, the
role of baroclinic instability is still in doubt since short
baroclinic waves tend to be quite shallow, as opposed to the
observed deep structure of the Pacific polar low. In addi-
tion, Sardie and Warner (1983) used a quasi-geostrophic
model to show that the maximum growth rate for conditions
typical of those during the formation of the Pacific polar
low is found at a wavelength of 2700 km.

The presence of convection suggests that it may be a
significant factor in the development of the Pacific polar
low. Rasmussen (1979) has shown that CISK is capable of
producing "mini-hurricanes" similar to the Atlantic polar
low. However, CISK requires a pre-existing circulation
which must be explained. Also, CISK requires a small
vertical wind shear, a condition not often met during the
development of the Pacific polar low (Mullen, 1979).

Therefore, it appears that some combination of
baroclinic instability and diabatic processes, such as
convection, are responsible for the development of the
Pacific polar low. It has been shown that R_i coupled with a
CISK-type latent heating shifts the most unstable wavelength
from the synoptic-scale to 1000-2000 km waves (Gambo, 1976;
Rao and Ferreari, 1979; Sardie and Warner, 1983). Also,

surface (Reed, 1979). The Pacific polar low tends to form
north of the polar jet in a strong baroclinic zone within
a polar air mass. The overall appearance of this system
resembles that of typical synoptic-scale extratropical
systems, but of smaller scale.

The purpose of this study is to investigate the
reasons for the growth of the Pacific polar low. It has
been proposed by Reed (1979) and Mullen (1979) that either
barotropic instability, Conditional Instability of the
Second Kind (CISK) or baroclinic instability may be respon-
sible, either singly or in some combination. Although the
conditions for barotropic instability are often met in the
Pacific during polar low formation (Mullen, 1979), Gall
(1976a) showed that barotropic effects are about an order of
magnitude smaller than baroclinic effects for wavenumber 15.

Many analytic studies support the argument that
baroclinic instability is responsible for the growth of
the Pacific polar low. The earliest studies of baroclinic
instability (Charney, 1947; Eady, 1949) indicate that
4000 km waves are most unstable and observations verify that
this scale dominates in extratropical regions. However,
more recent analytic studies show that the growth rate
spectrum is very sensitive to the Richardson number (R_i),
which is the ratio of the static stability to the square of
the vertical wind shear. Reduced R_i in the lowest levels

19

I. INTRODUCTION

The availability of global satellite photographs on a
daily basis has exposed meteorologists to weather disturb-
ances which were previously not known to exist. In
particular, systems called "polar lows" (Harley, 1960)
have been found to exist primarily over the oceans in the
winter seasons (Reed, 1979; Rasmussen, 1979). These storms,
which have horizontal scales of only 500-1500 km, can be
quite violent and occasionally exhibit thunder, lightning,
hail and hurricane-force wind gusts (Stevenson, 1968;
Suttie, 1970; Lyall, 1972).

It has been suggested that two distinctly different
types of polar lows exist (Rasmussen, 1981; Locatelli
et al., 1982; Sardie and Warner, 1983). The first of
these is the Atlantic polar low, which typically has a
spiral structure and occasionally an "eye" similar to that
found in tropical storms. This disturbance exhibits a
horizontal scale of 500-1000 km and maximum amplitude at
the surface. In addition, it tends to form within a polar
air mass north of the polar jet in an area with weak or
negligible baroclinity. The second type is the Pacific
polar low. This disturbance exhibits wavelengths of 1000-
1500 km and is often a deep system, occasionally exhibiting
height perturbations at 300 mb larger than those at the

18

ACKNOWLEDGEMENTS

θ_V = virtual potential temperature

θ_0 = water temperature

ω = vertical p-velocity = dp/dt

Subscripts

B = bottom of layer

c = cloud value; center of grid

m = mean PBL value

n = value for neutral PBL

r = reference state

s = surface value

T = top of layer

o = central latitude; 45N

R_{iB} = bulk Richardson number

R_{ic} = critical bulk Richardson number

t = time

T = temperature

T_{std} = standard atmosphere temperature

u = component of wind in x-direction

u_* = friction velocity

v = component of wind in y-direction

V = two dimensional velocity vector = $u\,\hat{i} + v\,\hat{j}$

W_e = entrainment velocity

x = east-west coordinate

X = east-west domain extent

y = north-south coordinate

Y = north-south domain extent

z_o = roughness length

α = inflow angle

β = df/dy

∇ = two dimensional del operator = $\partial/\partial x\,\hat{i} + \partial/\partial y\,\hat{j}$

ϕ = geopotential

K = R/C_p

ρ = density

π = terrain pressure

σ = vertical coordinate = p/π

$\dot{\sigma}$ = vertical σ-velocity = $d\sigma/dt$

θ = potential temperature

LIST OF SYMBOLS

C_D = drag coefficient

C_u = friction coefficient

C_{un} = neutral value of friction coefficient

C_θ = heat transport coefficient

$C_{\theta n}$ = neutral value of heat transport coefficient

d_1 = depth of layer of negative heat flux at top of PBL

f = Coriolis parameter

F_u = friction force in x-direction

F_v = friction force in y-direction

g = gravitational acceleration = $9.8 ms^{-1}$

h = height of PBL

h_e = equilibrium height of PBL

k = von Kàrman constant = 0.35

K_H = horizontal eddy diffusion coefficient

l_x = east-west domain extent

l_y = north-south domain extent

M_t = moisture convergence

p = pressure

q = mixing ratio

q^* = saturation mixing ratio

q_{std} = standard atmosphere saturation mixing ratio

Q^* = diabatic heating rate

R = specific gas constant for air = 287.04 J kg^{-1} K^{-1}

14

13

eliminate any small perturbations which may have been
introduced in the tabulation or interpolation of the data.
Cross-sections of the mean winter and genesis jets are shown
in Fig. 2-1.

2. Initialization

The equations used in the initialization are greatly
simplified since initially, all x-derivatives are zero and
v=0 over the entire domain. The initial north-south surface
pressure gradient is computed geostrophically from the v-
equation of motion in σ coordinates,

$$\frac{\partial \ln \pi}{\partial y} = - \frac{fu}{RT} \tag{2.2}$$

subject to the boundary condition that the gradient of π is
zero across the boundaries. A constant surface temperature
of 282 K is used and the 1000 mb u-components in Fig. 2-1
are specified. The areal mean surface pressure is specified
as 1013.25 mb. Initial geopotentials on pressure surfaces
are computed geostrophically using

$$\frac{\partial \phi}{\partial y} = - fu \tag{2.3}$$

subject to the boundary condition that the gradient of ϕ is
zero across the boundaries. The mean height of each level
is computed as follows. Temperatures for both the mean
winter and genesis cases, as given by Mullen (1979), are
tabulated and interpolated to grid points in the manner
described in the previous section for the zonal wind.

26
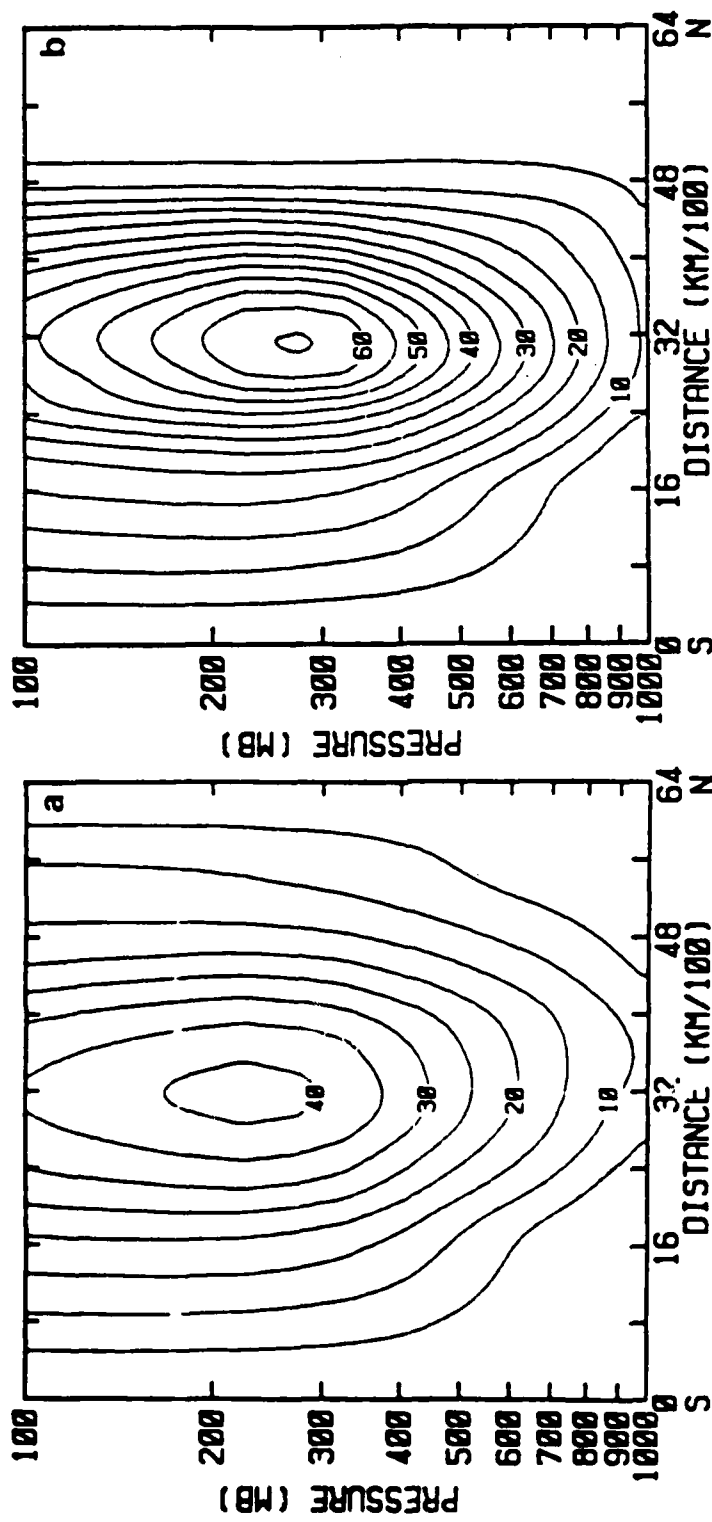
Fig. 2-1. Initialized north-south cross-sections of zonal
wind (m/s) for (a) mean winter and (b) genesis
jets. Contour interval is 5 m/s.

Heights are computed hydrostatically and the areal mean is found by averaging over each level.

The initial fields are then interpolated linearly with respect to $p^{0.2051}$ to the model σ coordinates. When the model is integrated with these fields, a north-south pressure oscillation, or "sloshing" of 3-4 mb is observed. To achieve a better balance in the initial fields, new height fields are computed using the v-equation of motion in σ coordinates,

$$\frac{\partial \phi}{\partial y} = - fu - RT \frac{\partial \ln \pi}{\partial y} \qquad (2.4)$$

subject to the boundary condition that the gradient of ϕ is zero across the boundaries. Eq. (2.4) must be solved by an iterative process, since the temperature appears on the right side. On the first pass, the temperatures obtained from Eq. (2.3) are used. On each succeeding pass, temperatures obtained from the previous iteration are used. The procedure is repeated for five iterations. By balancing the fields directly on the model σ coordinates, the pressure sloshing was reduced to less than 0.1 mb. After the initialization, the genesis fields exhibit superadiabatic lapse rates since no formal constraint is imposed. For the genesis case, the model is integrated for 12 h neglecting friction and diabatic effects to achieve a balanced state without superadiabatic layers present. Cross-sections of

28

the initialized temperatures for the mean winter and genesis cases are shown in Fig. 2-2.

The final prognostic variable to be initialized is the moisture. For both jet profiles, the zonal mean winter relative humidity fields for the northern hemisphere from London (1957) are used. Values are tabulated and interpolated in the same manner as for the zonal wind. The 1000 mb relative humidity given by Mullen (1979) for the genesis stage of the polar lows is used. A cross-section of the initial relative humidity is shown in Fig. 2-3.

The remaining variable to be specified is the sea-surface temperature (SST). All experiments apply for over-water conditions. The specific SST distribution is described with each experiment. There is no east-west gradient in the SST and the values are fixed throughout the forecast. The surface moisture is the saturation value corresponding to the SST.

B. ENERGY BUDGET

An energy budget is useful for studying the development and maintenance of the atmospheric disturbance. It is common practice to decompose the energy equations into equations for zonal and eddy components of the flow. This is particularly useful in this study, as a perturbation grows in a zonal flow. Energy transfers within the eddy, and interactions between the eddy and the zonal flow, will
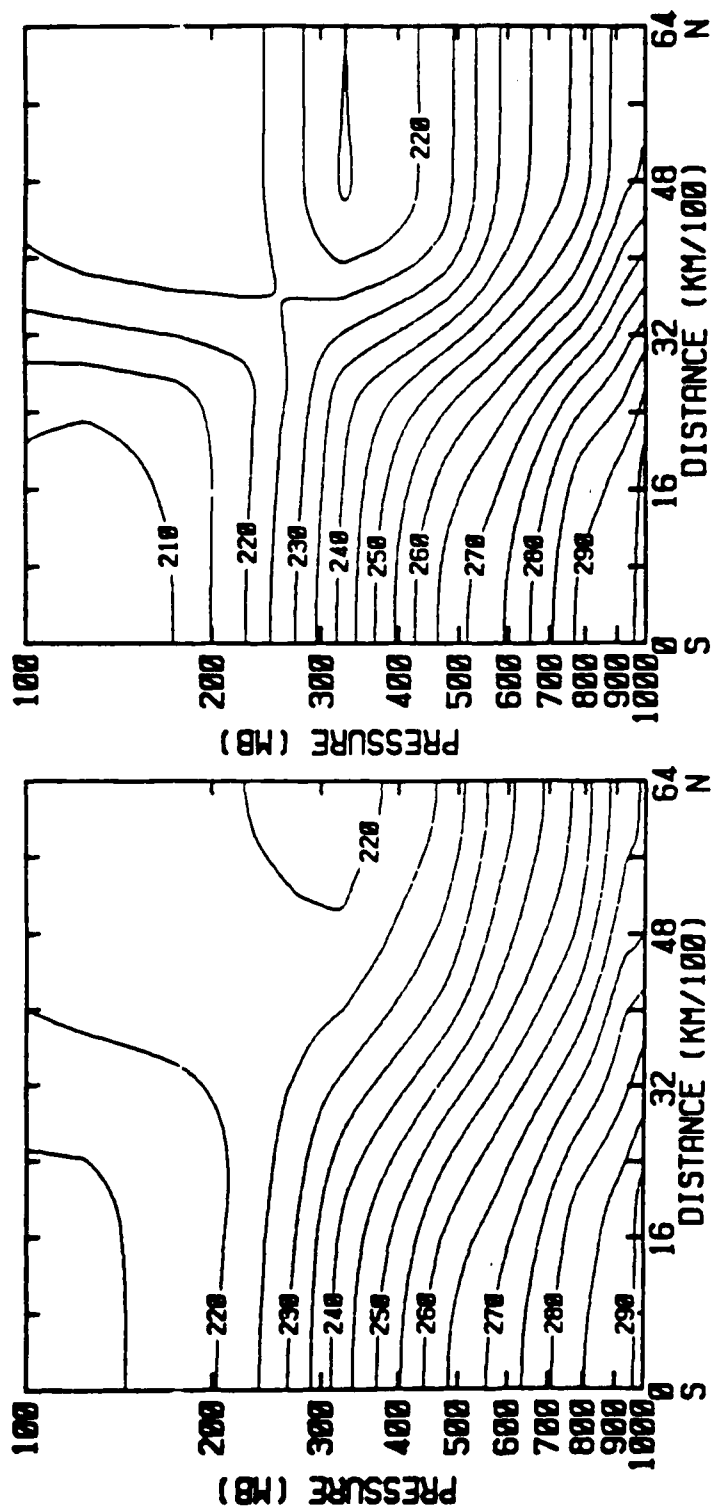
Fig. 2-2. Initialized north-south cross-sections of temperature (K) for (a) mean winter and (b) genesis jets. Contour interval is 5 K.

30
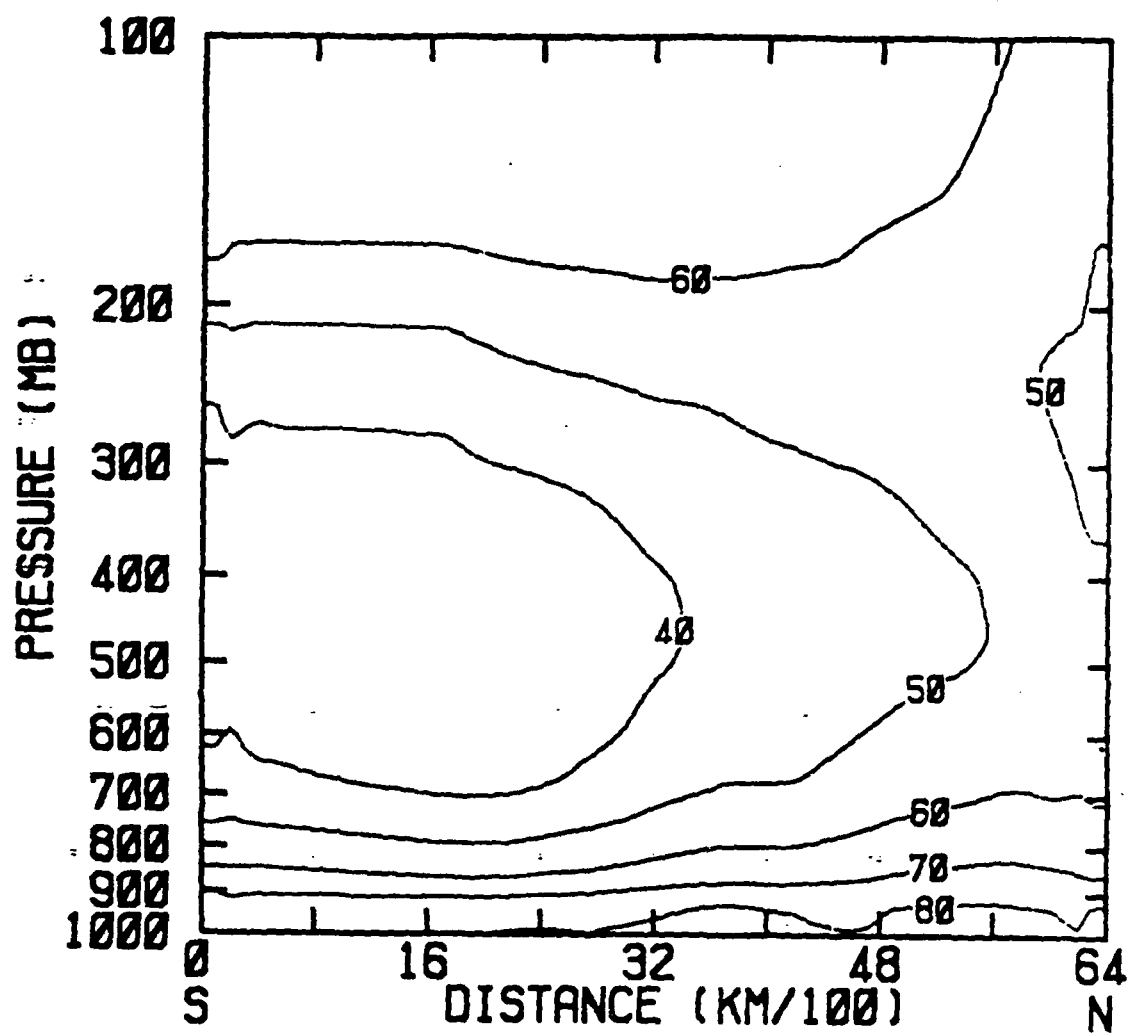
Fig. 2-3. Initial north-south cross-section of relative
humidity (%). Contour interval is 10%.

31

be studied. The effects of friction and diabatic processes
also will be described in terms of the energy budgets.

Many earlier studies have used the energy equations
developed by Lorenz (1955), which include an approximate
form of the available potential energy. Gall and Johnson
(1971) demonstrated that this form of the equations can
produce erroneous generation of eddy available potential
energy. For this reason, an exact formulation of the energy
equations, as derived by Robertson and Smith (1983), is used
in the study. A description of the budget equations is
given in Appendix B.

The energy budget terms are calculated using output
fields from the forecast model. All fields are saved each
6 h and are time-averaged during the model integration for
a one-hour period centered on the output time. Therefore,
a 12 h forecast field represents the average of all forecast
times between 11.5 and 12.5 hours. All fields are inter-
polated linearly with respect to ln p from the model σ
coordinates to constant pressure surfaces. There are 22
constant pressure surfaces in 50 mb increments starting at
25 mb and extending down to 1075 mb. Only those points at
or above the surface are used in the budget calculations.
That is, any mean quantity at 1025 mb is calculated using
only those points for which the surface pressure $\geq$ 1025 mb.

The transformation of the vertical velocity from the model σ coordinates to pressure surfaces necessitated the saving of several fields. This transformation is obtained by substituting Eq. (A-1) into $\omega = dp/dt$, which yields,

$$\omega = \pi\dot{\sigma} + \sigma\,\frac{\partial\pi}{\partial t} + \sigma V \cdot \nabla\pi \qquad (2.5)$$

The first term on the right side of Eq. (2.5) is simply the model vertical motion at the interfaces of the model layers. These fields are interpolated directly to the pressure surfaces. The last two terms are calculated at the middle of each model σ layer and are interpolated directly from these levels to the pressure surfaces. As a check, ω was also calculated kinematically using the time-averaged velocity fields on pressure surfaces. Differences in the budget results were less than a few percent.

The computation of the reference pressure is done as follows. First, $\ln p$ is interpolated linearly with respect to θ from the model σ coordinates to isentropic surfaces at 1 K intervals. All isentropic surfaces below the earth's surface are assigned a value of $\ln \pi$. Second, the areal mean pressure (i.e., the reference pressure, p_r) is calculated on each isentropic surface. Third, $\ln p_r$ is interpolated to pressure surfaces linearly with respect to θ. Cross-sections of the initial efficiency factor for both jet structures are shown in Fig. 2-4.

33
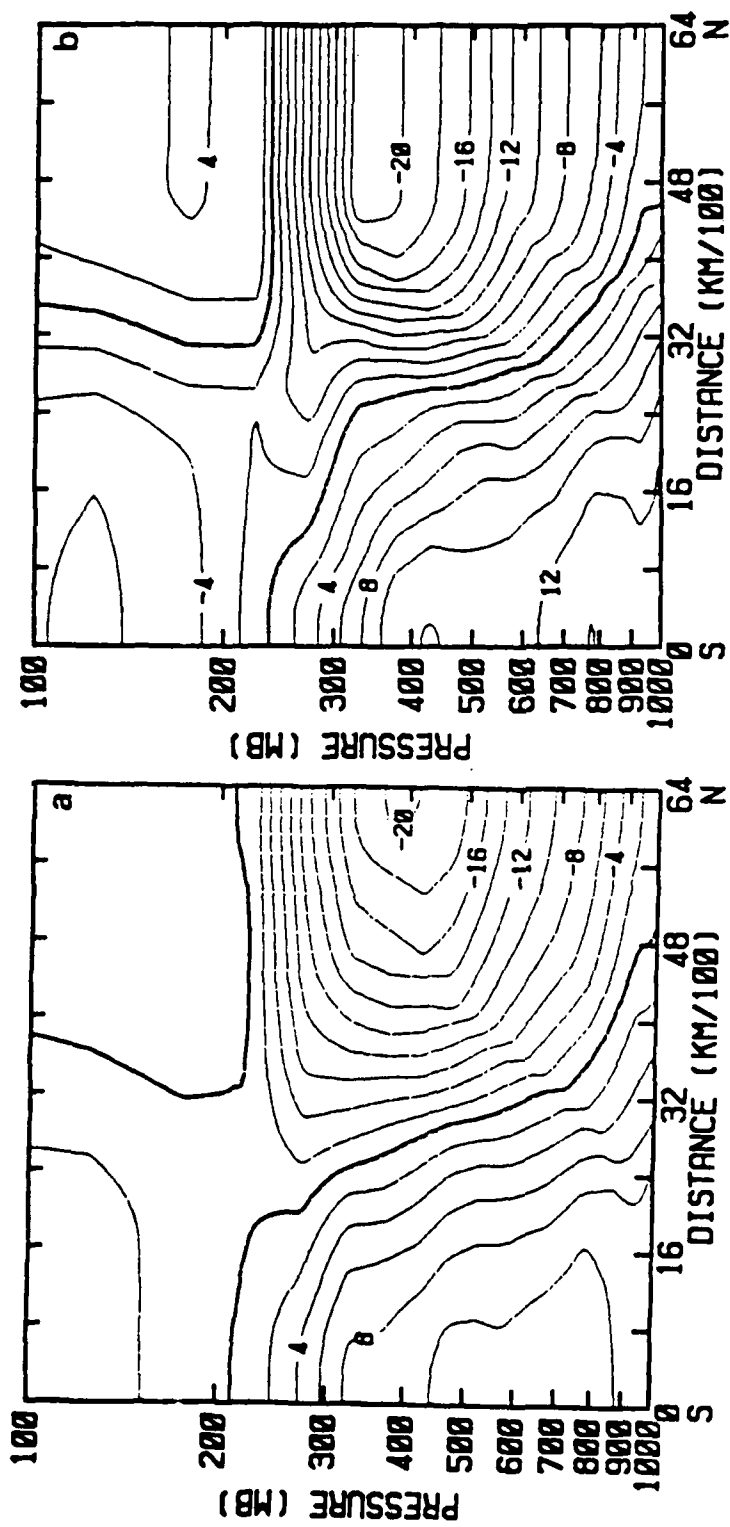
Fig. 2-4. Initial north-south cross-sections of the efficiency factor E (x 10⁻²) for (a) mean winter and (b) genesis jets. Contour interval is 2.

34

No horizontal interpolation is necessary for the model output fields. All horizontal derivatives are computed in a manner consistent with the model finite differencing on the scheme C grid. Centered differencing is used for vertical derivatives. The time change in energy is computed using a centered difference over a 12-h interval.

III. LINEAR GROWTH STUDIES

The concept of using the perturbation technique to study wave growth in a zonal flow was introduced by Charney (1947) and Eady (1949). These studies indicated that the most unstable wavelength for mean atmospheric conditions was about 4000 km. In general, this agrees with observations which show that the extratropical regions are dominated by waves of this size. However, more recent studies by Simons (1972) and Gall (1976a) indicate that the most unstable wavelength depends critically on the mean flow structure. Gall (1976a) showed with the linearized equations that wavenumber 15 was most unstable for mean winter conditions. However, wavenumber 15 failed to dominate over longer wavelengths due to wave-zonal flow interaction and surface friction effects for finite amplitude.

The purpose of this chapter is to study the growth rates for the mean winter and genesis jets described in Chapter II. First, linear growth rates will be computed for both jets and the energetics and structure of the most unstable waves will be examined. Second, the effect of wave-zonal flow interaction will be determined. Third, the effect of linearized surface friction on the growth rates will be examined.

A. EXPERIMENTAL DESIGN

A reduced version of the numerical model described in
Appendix A is used to study the linear growth rates of
perturbations in the mean winter and genesis jets. Two
simplifications are made to the model in these experiments.
First, the physical processes are not included. Second,
after each time step, the zonal averages of u, v, T and π
are replaced with the initial zonal averages of their
respective values, which eliminates interactions between the
growing waves and the zonal flow. These simplifications
transform the nonlinear model into a linear model with
respect to interaction with the mean flow. The nonlinear
interactions between waves are still included.

The Cartesian grid has a horizontal resolution of 100 km
with 94 grid intervals in the x-direction and 64 intervals
in the y-direction. Therefore, the east-west extent of the
grid is 9400 km or 1/3 of the global circumference at 45N.
Since the genesis jet exhibited the largest growth rates for
the shortest waves, another version of the model was run for
the genesis case only. This version uses 75 km resolution
with 94 intervals in the x-direction and 85 intervals in the
y-direction. The east-west extent of this grid is 7050 km
or 1/4 of the global circumference at 45N. The model
vertical levels are given in Table A-1.

Initial v-component perturbations are introduced for model wavenumbers 1-10. These correspond to earth wavenumbers 3-30 (4-40) in increments of 3(4) for the 100(75) km grid. The perturbation, which is constant in the vertical, is given by,

$$v' = V \sin \left(\frac{2 \pi x}{l_x}\right) \sin^2 \left[\frac{(y - y_c) \pi}{l_y}\right] \qquad (3.1)$$

The y-structure is chosen so v'=0 on the north and south boundaries. The initial amplitude of the perturbations is 0.1 m s^{-1} for the mean winter jet. However, the initial amplitude for the genesis jet was set to 0.01 m s^{-1} because it exhibited such high growth rates. This insured a longer period over which to compute the linear growth rate. As noted by Gall (1976a), the imposition of the initial perturbation leads to generation of gravity waves. Due to the presence of these waves, it was estimated that the growth rate was computed to within an accuracy of 0.05 day^{-1} in this study.

The technique used to evaluate the linear growth rate is similar to that used by Gall (1976b), who inserted only one wave per forecast. Therefore, Gall required many forecasts to achieve the growth rate spectrum for the given zonal flow. In this experiment, 10 wavenumbers are included initially, so that interactions between waves may alter the growth rates of some of the waves. However, these nonlinear

38

interactions will remain small since the perturbations are small. As a check, the model was run with only one wave-number in the initial fields for two different wavenumbers. The growth rates computed from these runs were identical to those computed when all 10 wavenumbers were included, which verified that the nonlinear effects were small.

The growth rates and phase speeds were computed as follows. A double Fourier decomposition of the v-component in the lowest model layer was calculated every 12 h to get the amplitude and phase of each of the 10 waves. During the period of linear growth, the growth rate for each wave was computed as

$$\mu C_i = \frac{\partial(\ln v')}{\partial t} = \frac{\ln v'_e - \ln v'_s}{\Delta t} \qquad (3.2)$$

where the subscripts s and e refer to the start and the end of the linear growth period. Phase speeds were also calcu-lated for each 12-h period, and were averaged during the period of linear growth for each wave.

B. WAVE GROWTH

1. Linear Growth Rates and Wave Structure

The growth rates computed for the mean winter and genesis jets are shown in Fig. 3-1. There are two major differences between the curves. First, the genesis jet exhibits much larger growth rates, especially for

39
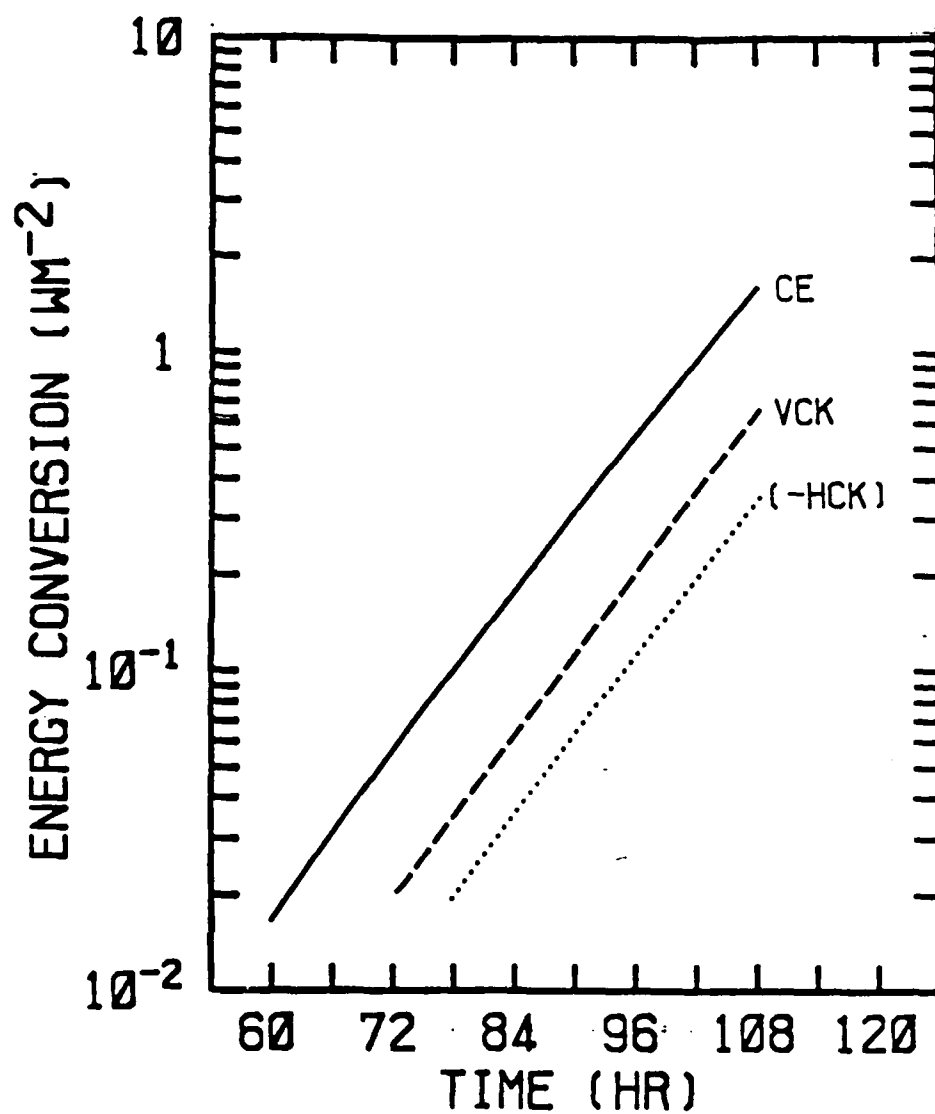
Fig. 3-8.   Similar to Fig. 3-7 except for wavenumber 8 in genesis jet.
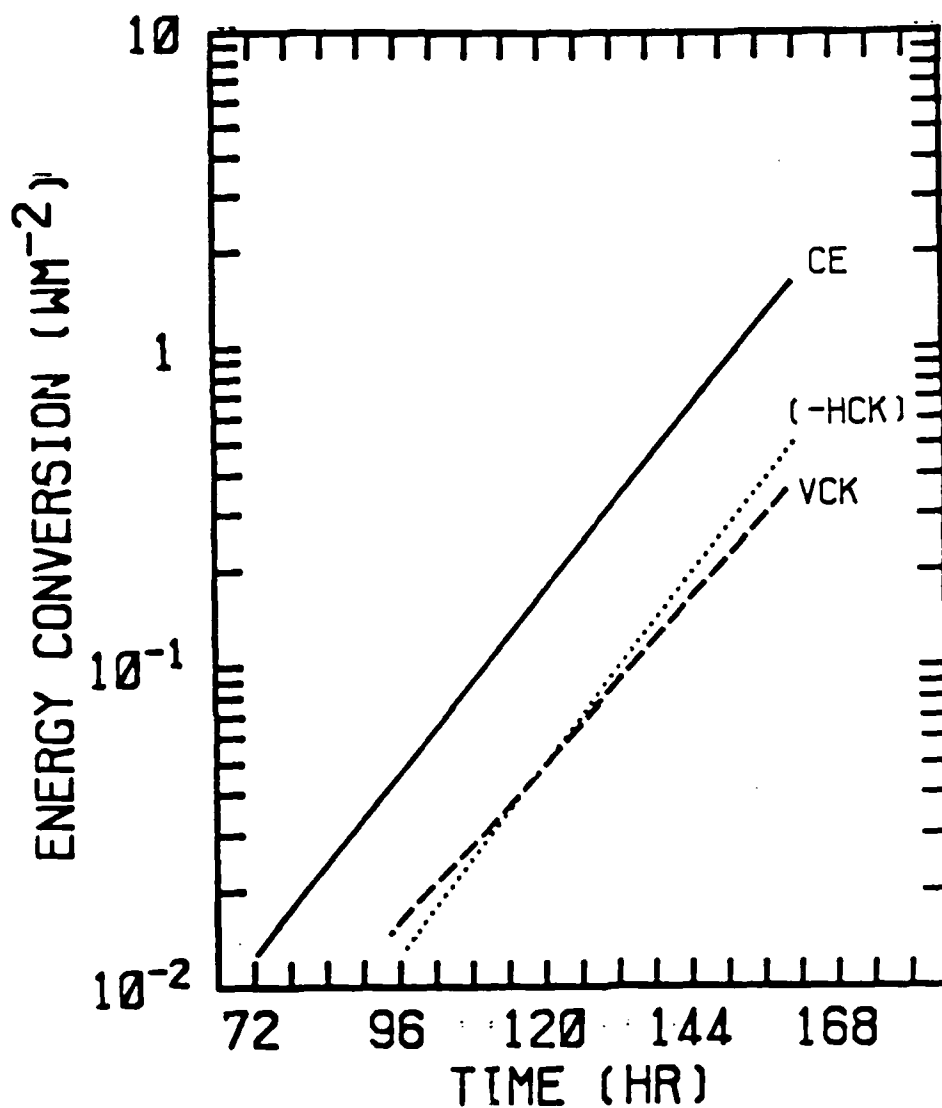
Fig. 3-7. Time variation of CE, (-HCK) and VCK for wave
number 12 in mean winter jet. See text for
description of terms.

previous experiments, the physical processes are neglected and the zonal averages of u, v, T, and π are restored each time step.

The time evolution of the terms CE, HCK and VCK for W12, G8 and G40 are given in Figs. 3-7, 3-8 and 3-9, respectively. For W12, CE is the dominant term, which shows that the growth of this wave is primarily through conventional baroclinic instability. HCK and VCK are 5-6 times smaller than CE, which indicates that barotropic and vertical shear effects are small. Also, HCK and VCK tend to cancel since they are nearly the same size but of opposite sign. For G8, CE is again the dominant term. VCK is positive and about one-third of CE, which suggests that Kelvin-Helmholtz instability may play a secondary role is the development of this disturbance. The HCK is again negative, but is only about half the magnitude of VCK. For G40, both CE and VCK are positive and nearly equal in magnitude, which shows that this wave draws as much energy from KZ as from AE. Term HCK is negative and an order of magnitude less than CE and VCK.

It is apparent from Figs. 3-7, 3-8 and 3-9 that the length of time of linear growth of G40 is significantly less than that of the longer waves G8 and W12. While the linear growth rates extended past 120 h for G8 and W12, they only continued to about 60 h for G40. The reasons for the rapid stabilization of this wave will be discussed in the following section.

51

$\partial \bar{u}/\partial y < 0$, a positive (negative) correlation between u' and

v' leads to an increase (decrease) in KE. Generally,

troughs which tilt opposite the horizontal wind shear are

are barotropically unstable. VCK represents the term

$(-\overline{u'\omega'}\partial \bar{u}/\partial p)$ and therefore represents the same type of

motion as HCK but in the vertical plane. If the wind

increases with height, a positive (negative) correlation

between u' and ω' will lead to an increase (decrease) in KE.

This is referred to as Kelvin-Helmholtz (shearing) instabil-

ity which can become significant for $R_i < 1$ (Orlanski,

1968). The term VCK is not included in quasi-geostrophic

models such as the one used by Sardie and Warner (1983).

The most unstable mode for the mean winter jet is

wavenumber 12, referred to as W12, which corresponds to a

wavelength of about 2400 km. For the genesis jet, the most

unstable waves are wavenumbers 8 (G8) and 40 (G40), which

correspond to wavelengths of about 3500 and 720 km,

respectively. Three different model domains are used to

separately simulate these waves (Table 3-1). As in the

Table 3-1. Number of grid intervals and horizontal
resolution for waves W12, G8 and G40.

Wave	x-intervals	y-intervals	Horizontal Resolution (km)
W12	24	64	100
G8	35	64	100
G40	18	160	40

speeds in the genesis case. For the mean winter jet, the maximum phase speed occurs at wavenumber 9, and there is a general decrease in phase speed for shorter waves. For the genesis jet, the maximum phase speed is also at wavenumber 9 with a similar decrease in phase speed for the shorter waves. The lower phase speeds for the shorter waves are because these shallow systems have a lower steering level.

2. Energy Conversions

The most unstable mode for the mean winter jet and the two most unstable modes for the genesis jet are now examined in more detail. For each of these waves, the model is configured to allow just that wave in the domain, so the process(es) leading to its development can be isolated. In particular, the baroclinic conversion (CE) between eddy available potential energy (AE) and eddy kinetic energy (KE) and the conversion (CK) between zonal kinetic energy (KZ) and KE are examined.

The baroclinic term, CE, is the correlation between vertical velocity and temperature perturbations, $(\overline{\omega'T'})$. KE increases for rising warm air and sinking cold air at the same elevation, and vice versa. The conversion CK is separated into the horizontal (HCK) and vertical (VCK) components. Since v=0 in this linear study, HCK represents the barotropic term $(\overline{u'v'}\,\partial\bar{u}/\partial y)$ which is the correlation of u and v component perturbations multiplied by the meridional gradient of the mean zonal wind. North of the jet, where

49
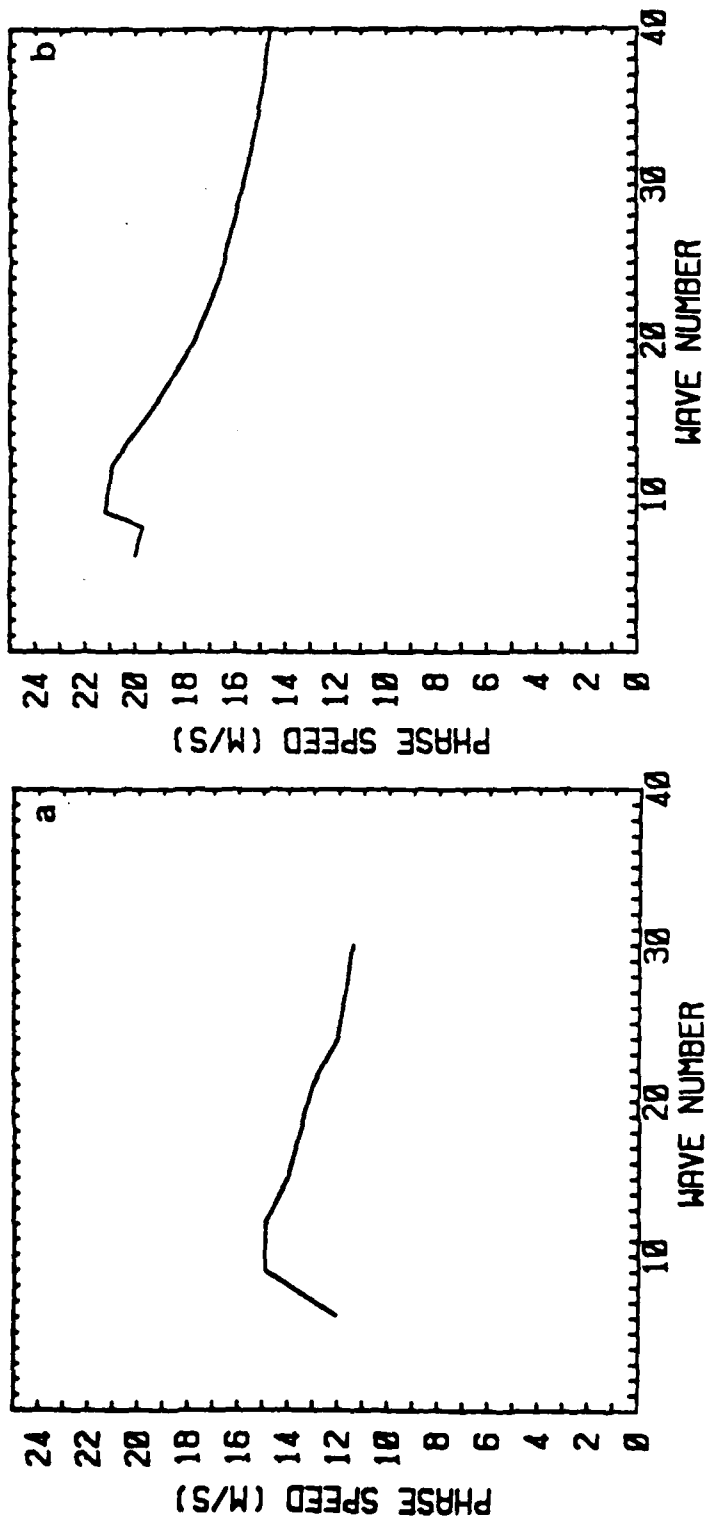
Fig. 3-6. Phase speeds (m/s) for perturbations in (a) mean winter and (b) genesis jets.
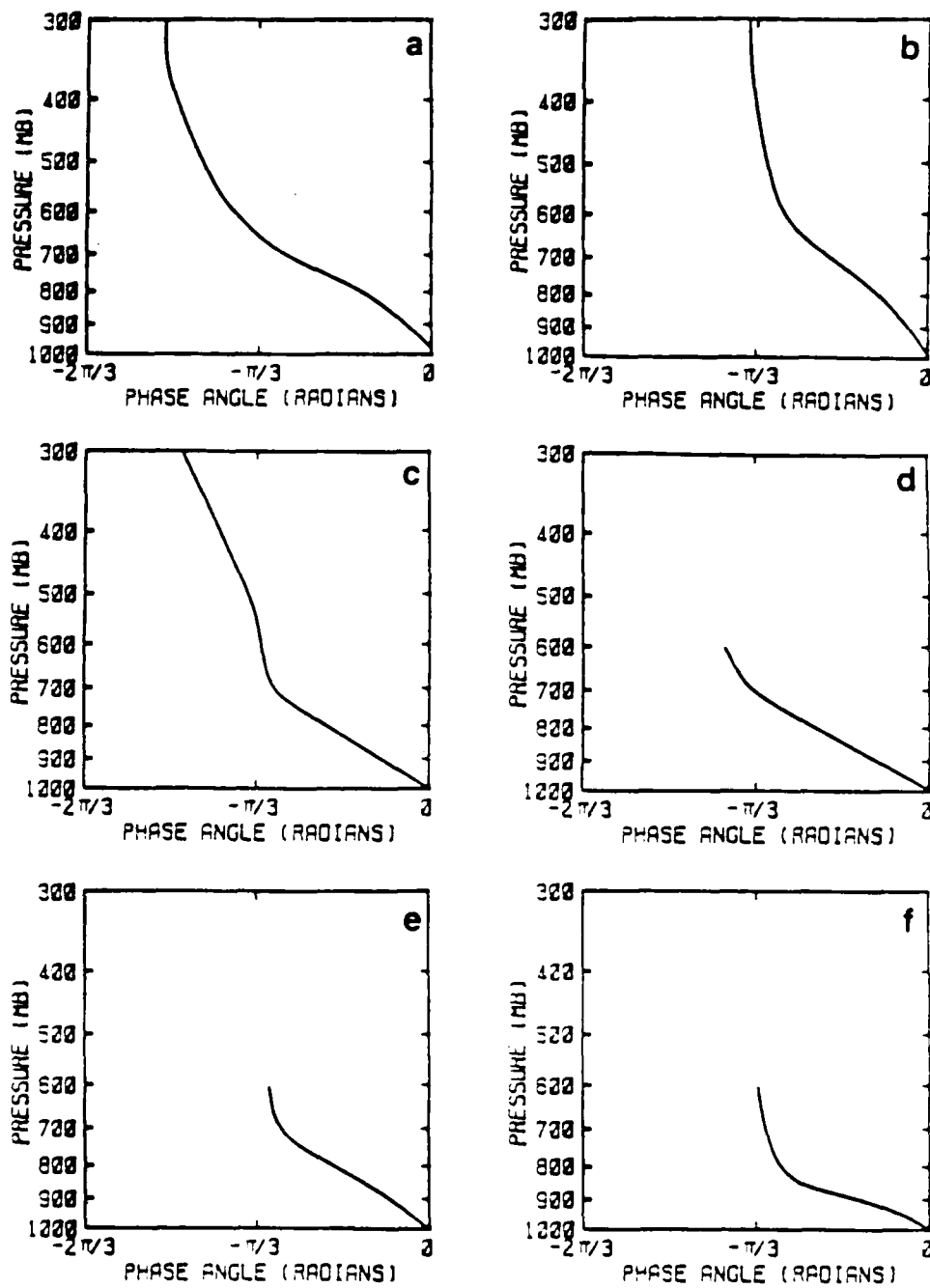
Fig. 3-5.   Phase angles for wavenumbers (a) 6, (b) 12,
             (c) 18, (d) 24, (e) 30 and (f) 40 for the genesis
             jet.
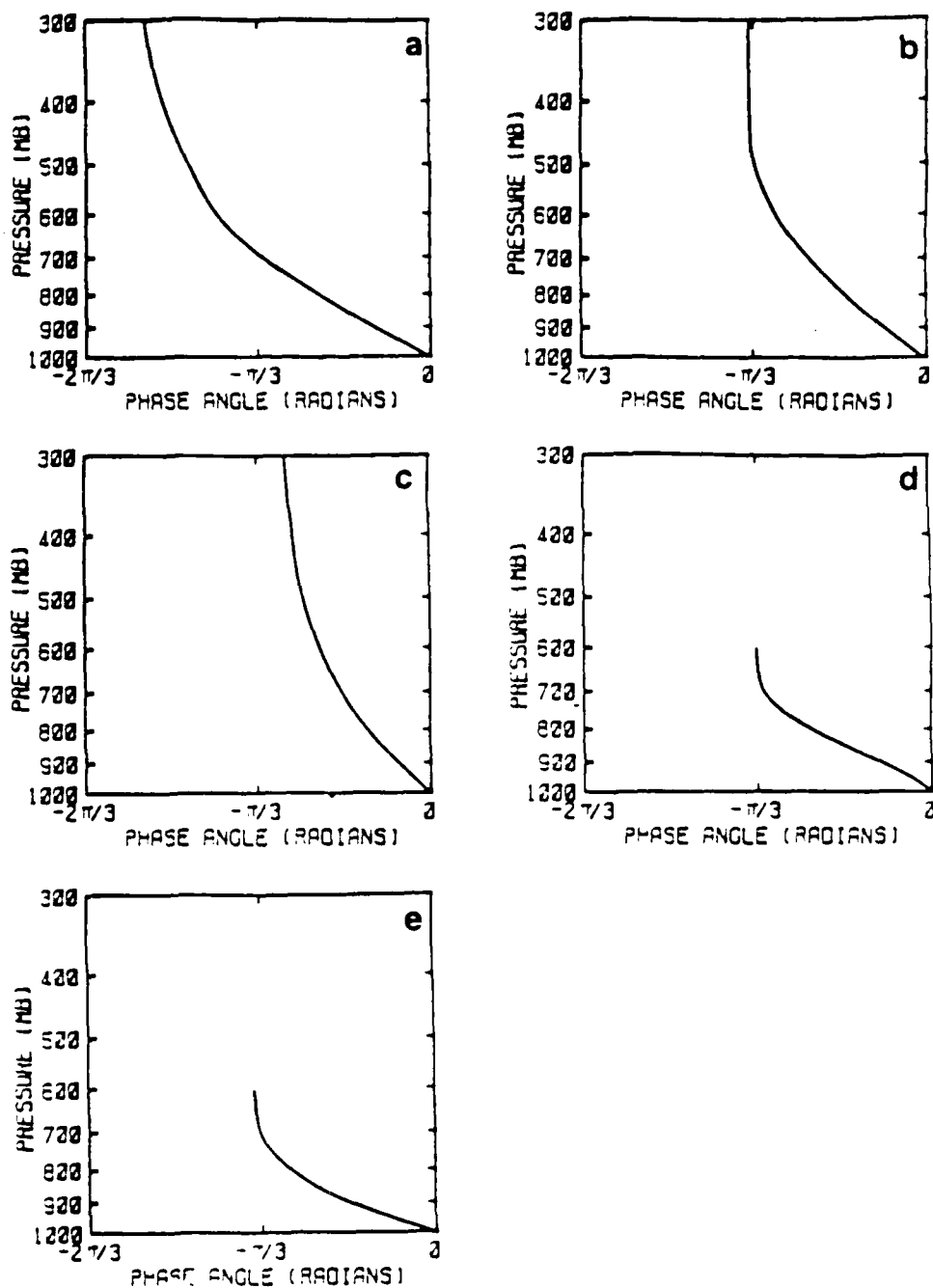
Fig. 3-4. Phase angles for wavenumbers (a) 6, (b) 12, (c) 18, (d) 24, and (e) 30 for the mean winter jet.

46

wavelength of maximum growth to shorter wavelengths. The
differences between the growth rates presented here for
the mean winter and genesis jets is evidence of this.
Staley and Gall (1977) also found that wavelengths less
than 3000 km (wavenumber >10) are confined below 500 mb
and exhibit their maximum amplitude at the surface.

The phase structure of wavenumbers 6, 12, 18, 24 and
30 for the mean winter jet and wavenumbers 6, 12, 18, 24, 30
and 40 for the genesis jet are shown in Figs. 3-4 and 3-5.
For both jets, wavenumber 6 has a pronounced tilt to the
west with height between the surface and 700 mb and a
reduced westward tilt up to 300 mb. For wavenumbers 12 and
18 in the mean winter case and wavenumber 12 in the genesis
case, a moderate westward tilt is observed in the lowest
400 mb with little or no tilt above. For the remaining
shorter waves, a very strong westward tilt is found in the
lowest 200-400 mb. This tilt becomes more pronounced for
increasing wavenumber. Since a westward tilt is associated
with baroclinic processes, these results suggest that baro-
clinic instability is exhibited by all waves, but is
confined to the lowest few hundred millibars for wavenumbers
greater than 12.

The phase speeds for the perturbations in the mean
winter and genesis jets are shown in Fig. 3-6. Phase speeds
in the genesis jet case are 30-40% higher than those in the
mean winter jet as would be expected from the larger wind

45
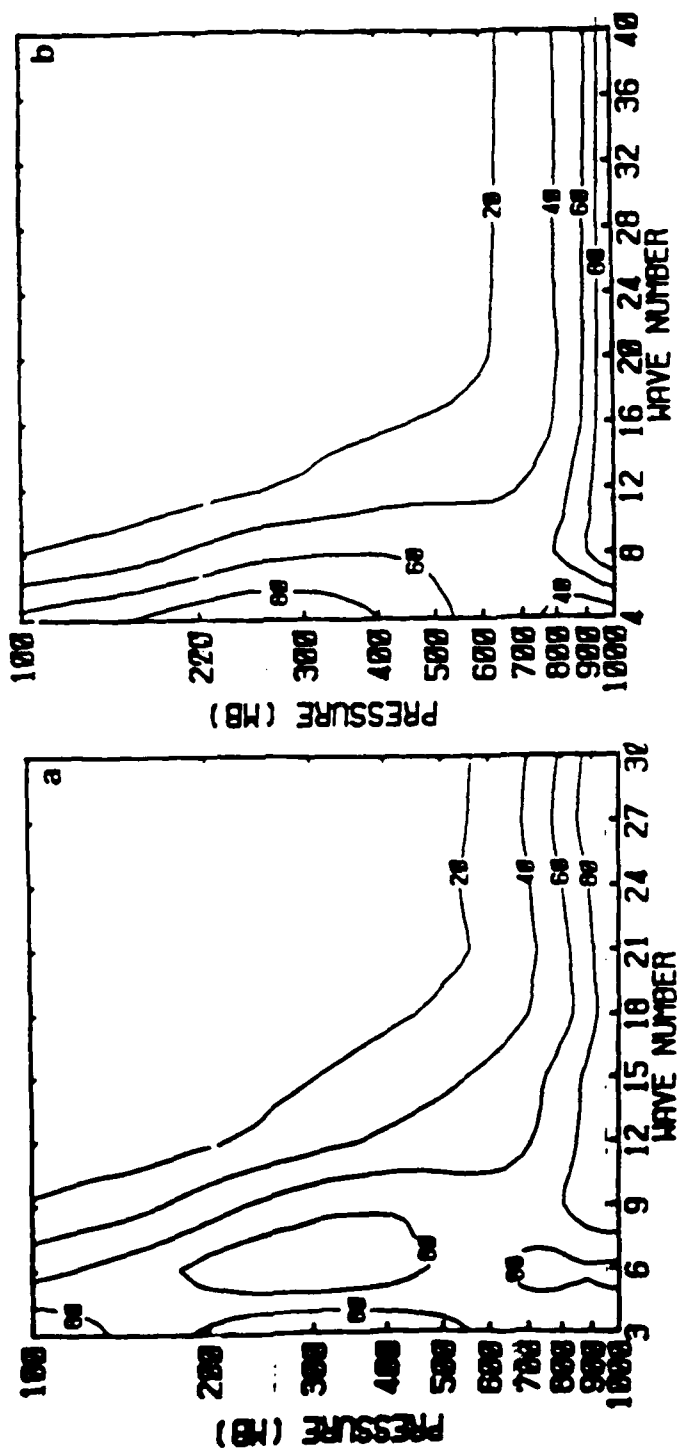
Fig. 3-3. Amplitudes of waves at 120 h for (a) mean winter and at 60 h for (b) genesis jet. Amplitudes have been normalized so that the largest amplitude for a given wavenumber is 100. Contour interval is 20.

44

that small, low-level static stability and/or an increase in the low-level wind shear (i.e., a small R_i) tends to shift the maximum growth rate to shorter wavelengths. It can be seen from Fig. 3-2 that the mean winter case has $R_i < 10$ over a large depth of the troposphere in the vicinity of the jet and in the low levels poleward of the jet. The genesis jet case exhibits the same pattern with $R_i < 2$ in the low-levels poleward of the jet core. In fact, many values are less than 1. This difference in R_i is consistent with the large difference in growth rates between the mean winter and genesis jet cases for wavenumbers greater than 21.

The normalized amplitude of the waves during the period of linear growth is similar for the mean winter and the genesis jet cases (Fig. 3-3). Wavenumber 6 has a maximum amplitude in the lowest layer and also near 300 mb. The shorter waves (wavenumber > 15) are confined to the lower troposphere with the maximum amplitude in the lowest layer. The amplitude of these short waves decreases to 20% of the near-surface values at 570 mb for the mean winter jet and at 650 mb for the genesis jet.

These results are consistent with those of Staley and Gall (1977), who used a 4-level quasi-geostrophic model to study the effect of wind shear and static stability on baroclinic development. They found that decreasing the low-level static stability (i.e., decreasing R_i) shifts the

43

Fig. 3-2. Initial zonally-averaged Richardson number for (a) mean winter and (b) genesis jets. Contour interval is 2. Values above 10 are not contoured.

42

wavenumbers greater than 20. Second, the most unstable wavelength is markedly different for the two jets. For the mean winter jet, wavenumber 12 is most unstable, with a growth rate of 0.59 day^{-1}. For the genesis jet, wavenumber 40 is most unstable with a growth rate of 1.82 day^{-1}, and a secondary maximum of 1.29 day^{-1} at wavenumber 8. Wavenumbers larger than 40, which were not tested here, may exhibit even larger growth rates.

The growth rates for the genesis jet were relatively easy to determine. However, growth rates for the mean winter jet for wavenumbers greater than 24 were more difficult to estimate. These waves exhibited little or no growth for up to 7 days and then experienced rapid growth. The longer waves (wavenumbers $\leq$ 24) generally began exponential growth between days 2 and 3 of the forecasts. It was judged that the eventual growth of the shortest waves was due to nonlinear interactions with the longer waves, which by day 7 had reached amplitudes > 5 m s^{-1}. Model runs including only wavenumber 28, or including only wavenumber 40 verified that the linear growth of these waves are quite small for the mean winter jet.

One explanation for the shorter wavelength disturbance in the genesis jet is illustrated by the Richardson number (R_i) distributions for both jets (Fig. 3-2). R_i is the ratio of the static stability to the square of the vertical wind shear. Staley and Gall (1977) demonstrated

41
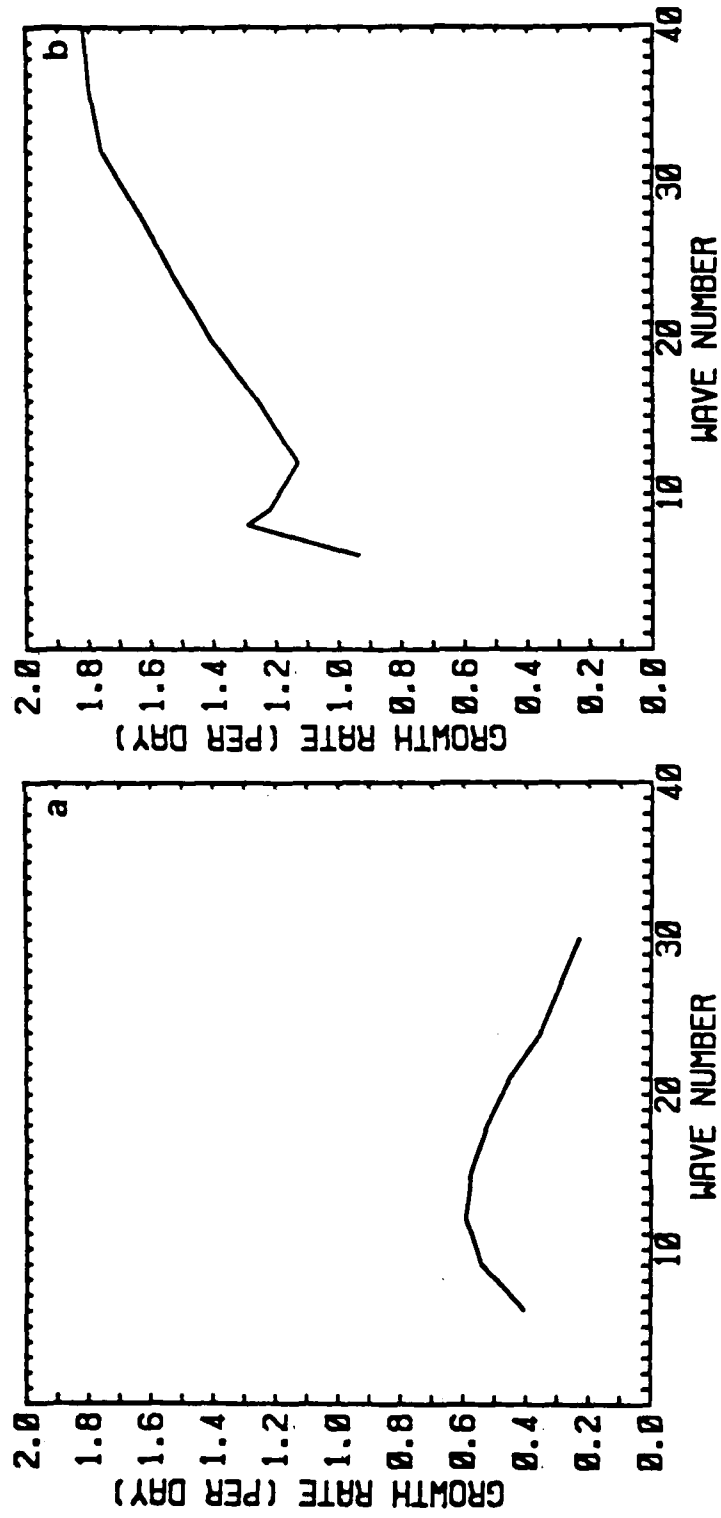
Fig. 3-1. Linear growth rates for (a) mean winter and (b) genesis jets for set A experiments.

40
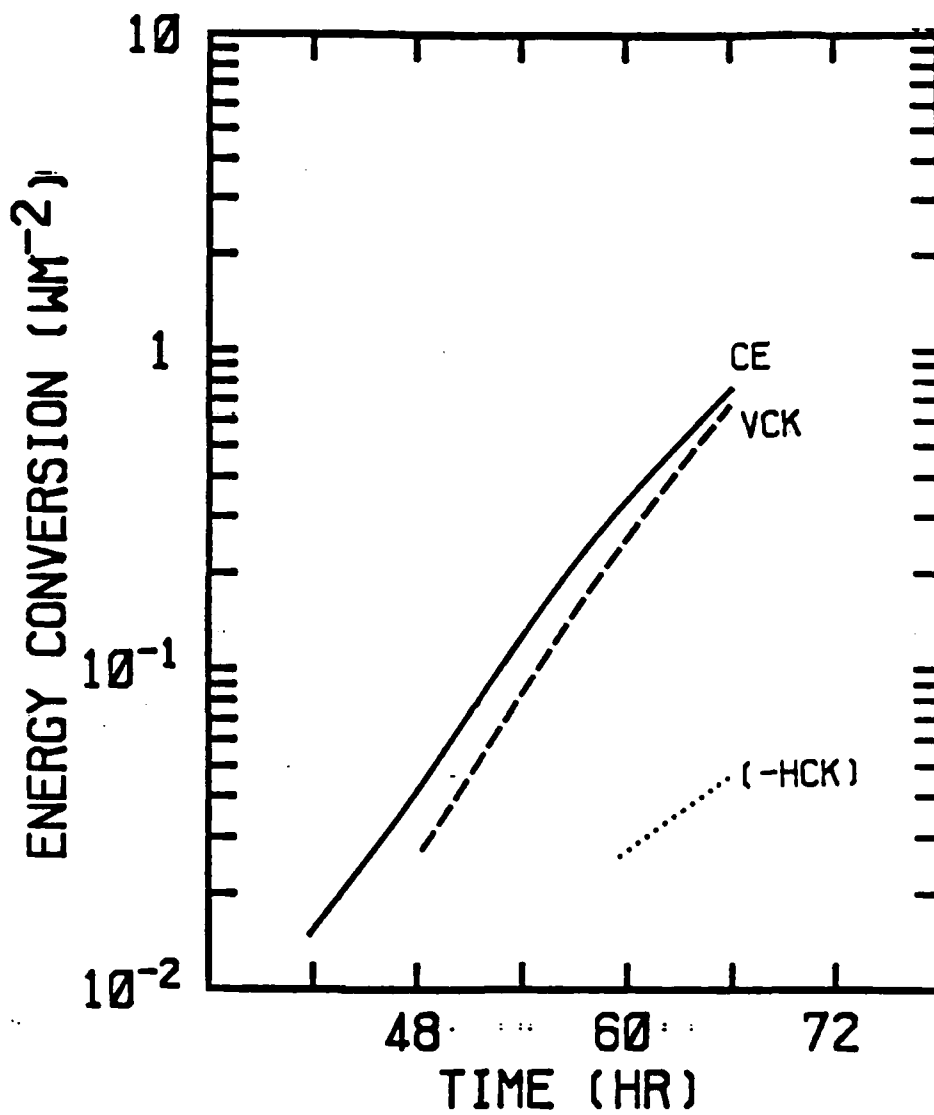
Fig. 3-9. Similar to Fig. 3-7 except for wavenumber 40 in genesis jet.

54

East-west cross sections of vertical velocity, temperature and trough position for W12, G8 and G40 are given in Figs. 3-10, 3-11 and 3-12, respectively. Very similar structures are observed for W12 and G8. For both of these waves, the trough tilts to the west with height with the maximum slope from 800 to 600 mb. The warmest air is found ahead of the trough with a slight tilt to the east with height below 700 mb and a slight tilt to the west with height above 700 mb. The maximum upward motion is found at 750 mb. A broad area of relatively weak subsidence occurs behind the W12 and G8 troughs.

The structure of the G40 wave is significantly different from W12 and G8 in that the warmest air slopes to the west with height, as does the trough. Therefore, only a shallow layer (about 250 mb thick) of warm air is found above the position of the surface low with relatively cold air above 750 mb. The upward motion above the position of the surface low leads to the generation of KE below 750 mb (i.e., CE > 0) and a destruction of KE above 750 mb. This is consistent with the shallow nature of this wave.

The relatively large values of VCK for G8 and especially for G40 are due to the strong vertical wind shear in the genesis jet. Since VCK>0 and $\partial \bar{u}/\partial p<0$, this implies a positive correlation exists between u' and ω'. Fields of u'
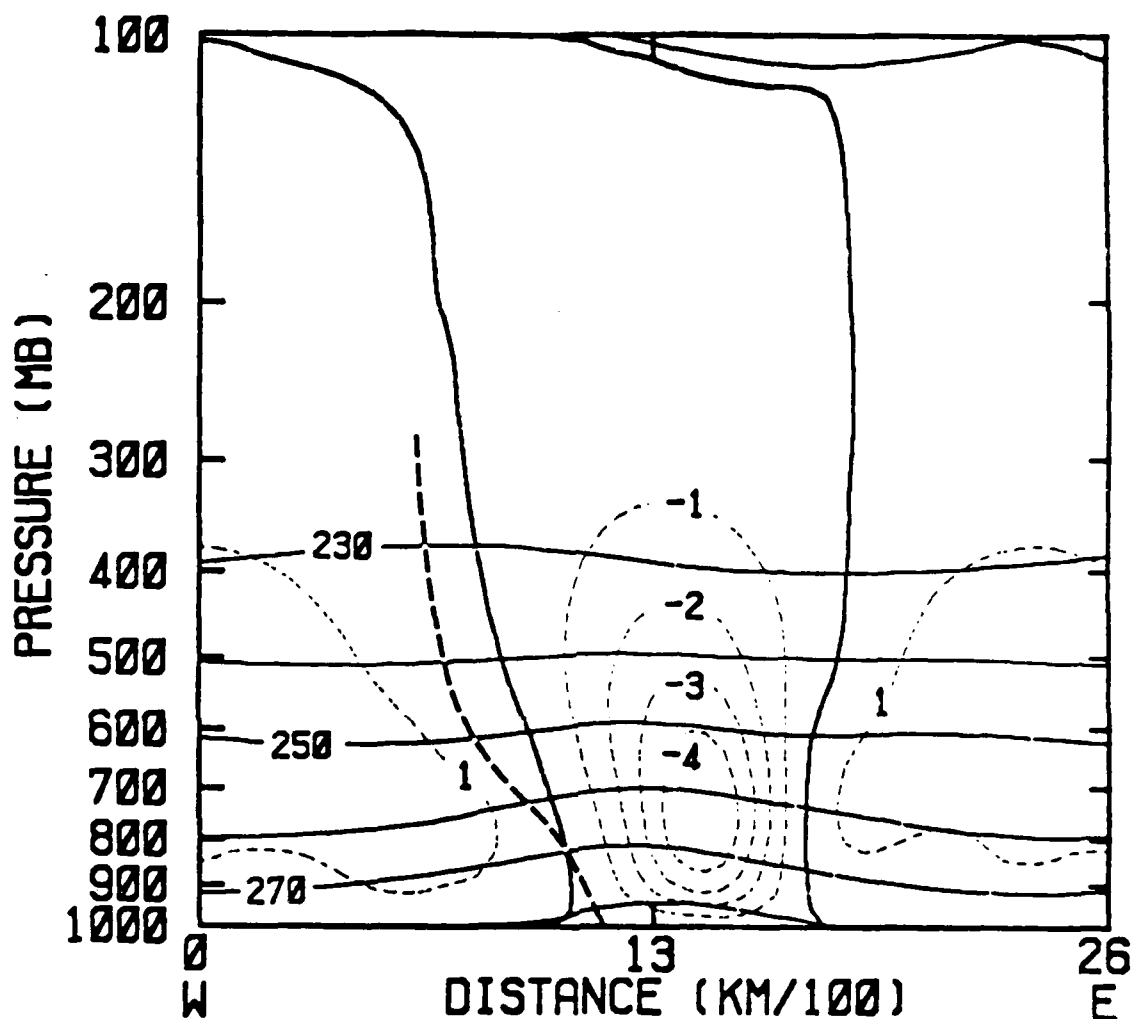
Fig. 3-10. East-west cross-section of ω (dashed line; heavy dark line is zero contour), T (solid line) and trough position (heavy dashed line) for wave-number 12 in mean winter jet. Contour interval is 1 μbar/s for ω and 10 K for T. 200 km of right side of domain is the same as leftmost 200 km due to periodicity.

56
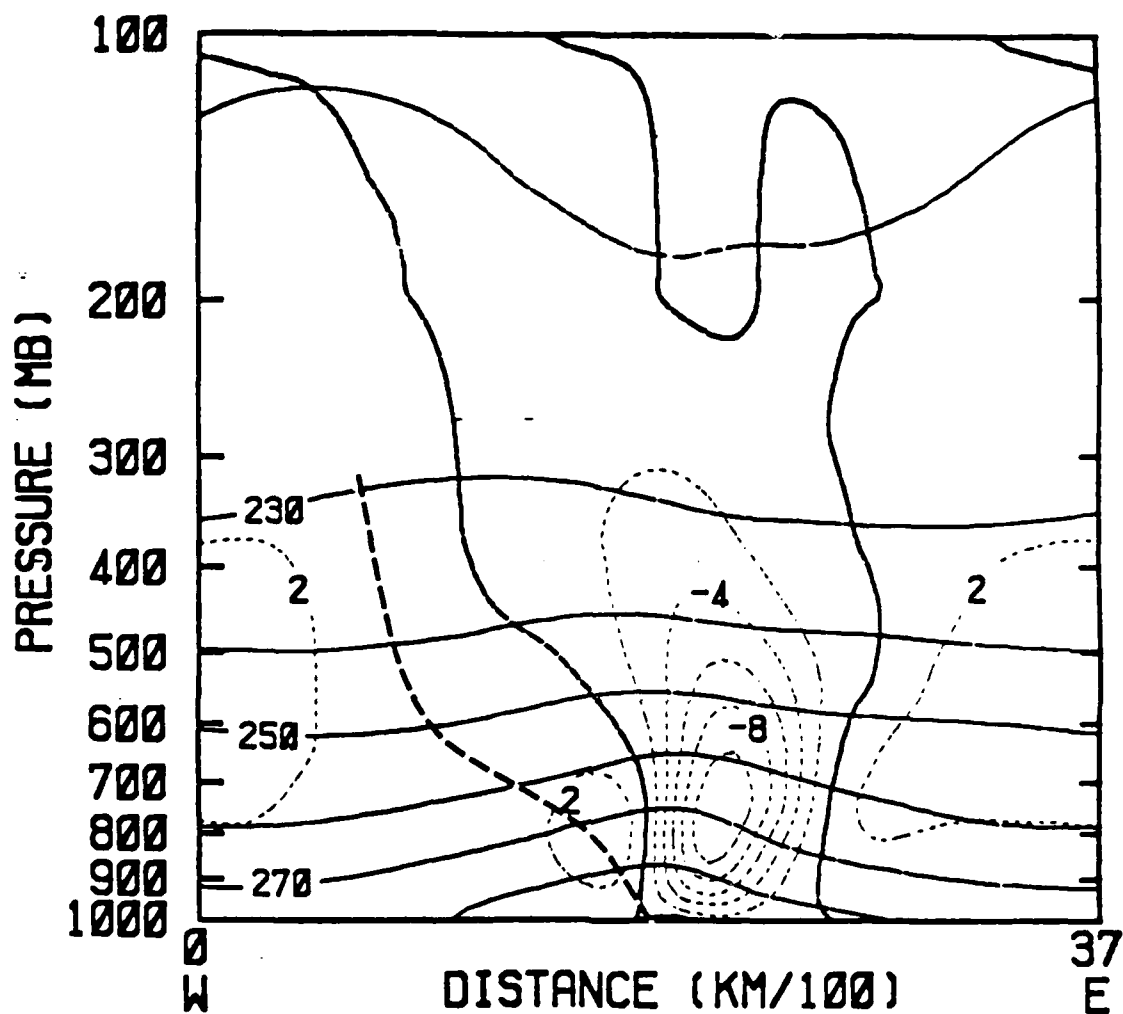
Fig. 3-11. Similar to Fig. 3-10 except for wavenumber 8 in genesis jet. Contour interval is 2 µbar/s for ω and 10 K for T.
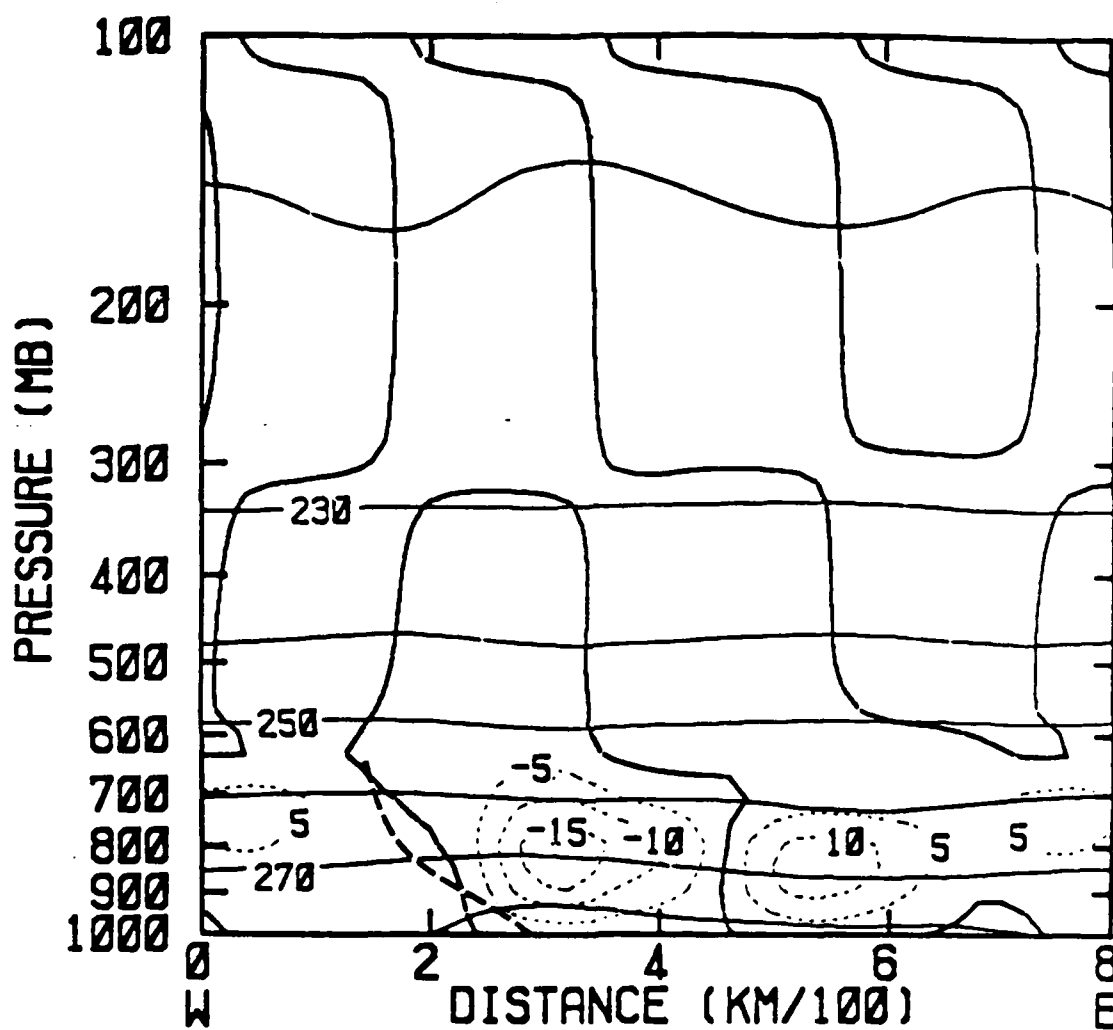
Fig. 3-12. Similar to Fig. 3-10 except for wavenumber 40 in genesis jet. Contour interval is 5 μbar/s for ω and 10 K for T. 80 km of right side of domain is the same as leftmost 80 km due to periodicity.

58

and ω' for G40 (Fig. 3-13) exhibit a pattern of upward motion in areas of east winds and downward motion in areas of west winds.

Orlanski (1968) showed that Kelvin-Helmholtz instability can dominate over conventional baroclinic instability for small R_i. Stone (1966) showed that helical circulations parallel to the zonal flow dominate for $0.95 < R_i < 0.25$ (symmetric instability), whereas the circulations are perpendicular to the zonal flow for $R_i < 0.25$ (Kelvin-Helmholtz instability). A north-south cross-section of v and ω through G40 is given in Fig. 3-14. Strong vertical shear in the v-component coupled with the horizontal gradient of ω leads to a circulation in the vertical plane *about a horizontal axis near 800 mb.* Since this is a north-south cross-section, this circulation is parallel to the zonal flow and suggests that symmetric instability is present. However, the u' and ω' fields in G40 (Fig. 3-13) suggest that this disturbance is strongly tilted by the horizontal wind shear and therefore this helical circulation may also be driven by the Kelvin-Helmholtz instability. R_i values computed in the lowest level range from 0.03-2.0, which indicates that either type of motion is possible. At any rate, the presence of this helical circulation is consistent with the results of Stone (1966) and Orlanski (1968). Therefore, based on the energy conversions and wave structure, it is concluded that G40 is a "mixed" baroclinic
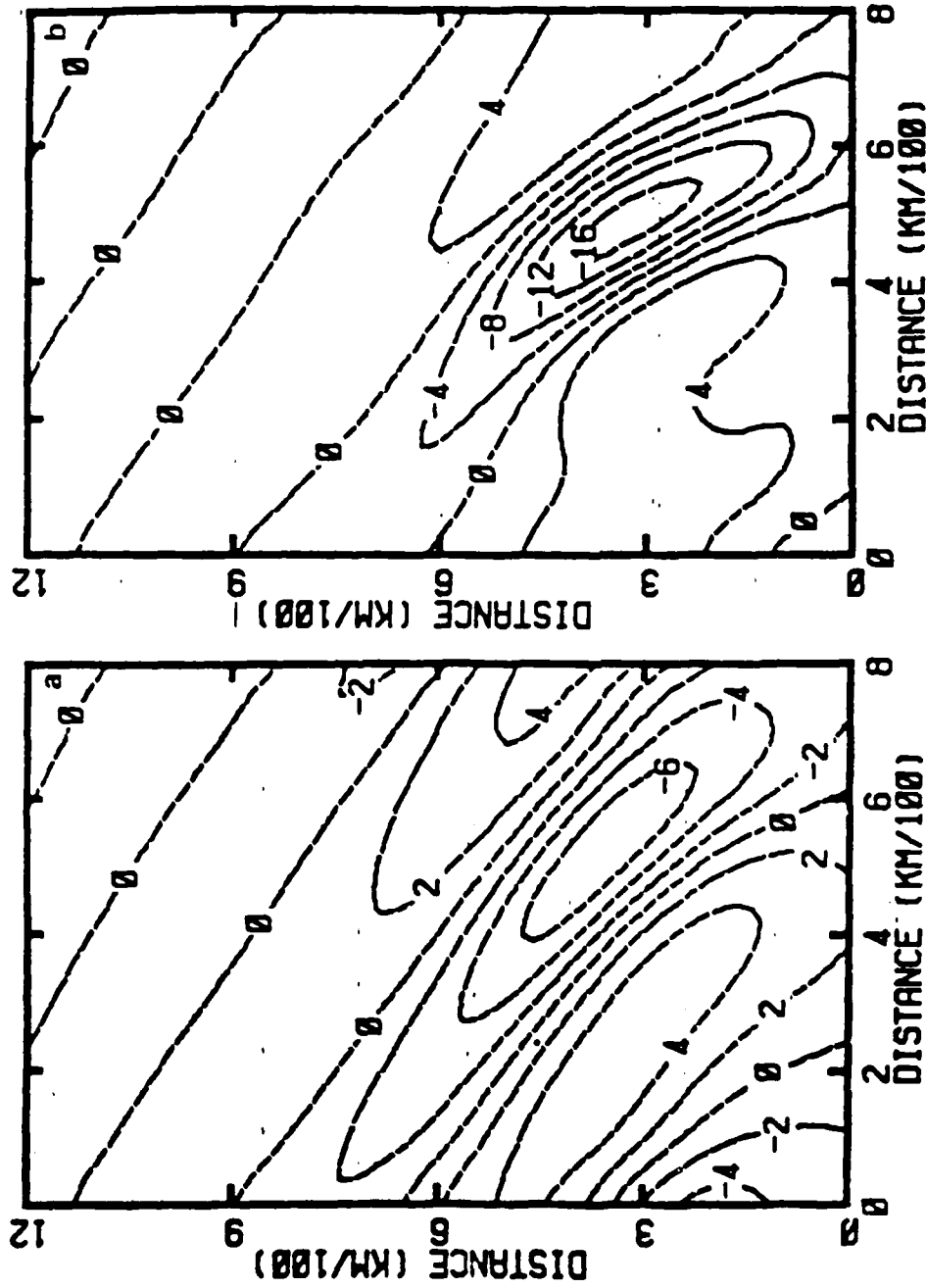
Fig. 3-13. Fields of (a) u' and (b) ω' at 925 mb for wavenumber 40. Contour interval is 2 m/s for u' and 4 μbar/s for ω'. Figures represent a subsection of the forecast domain. Southern boundary of figures is at the center of the forecast domain. 80 km of right side of domain is the same as the leftmost 80 km due to periodicity.

60
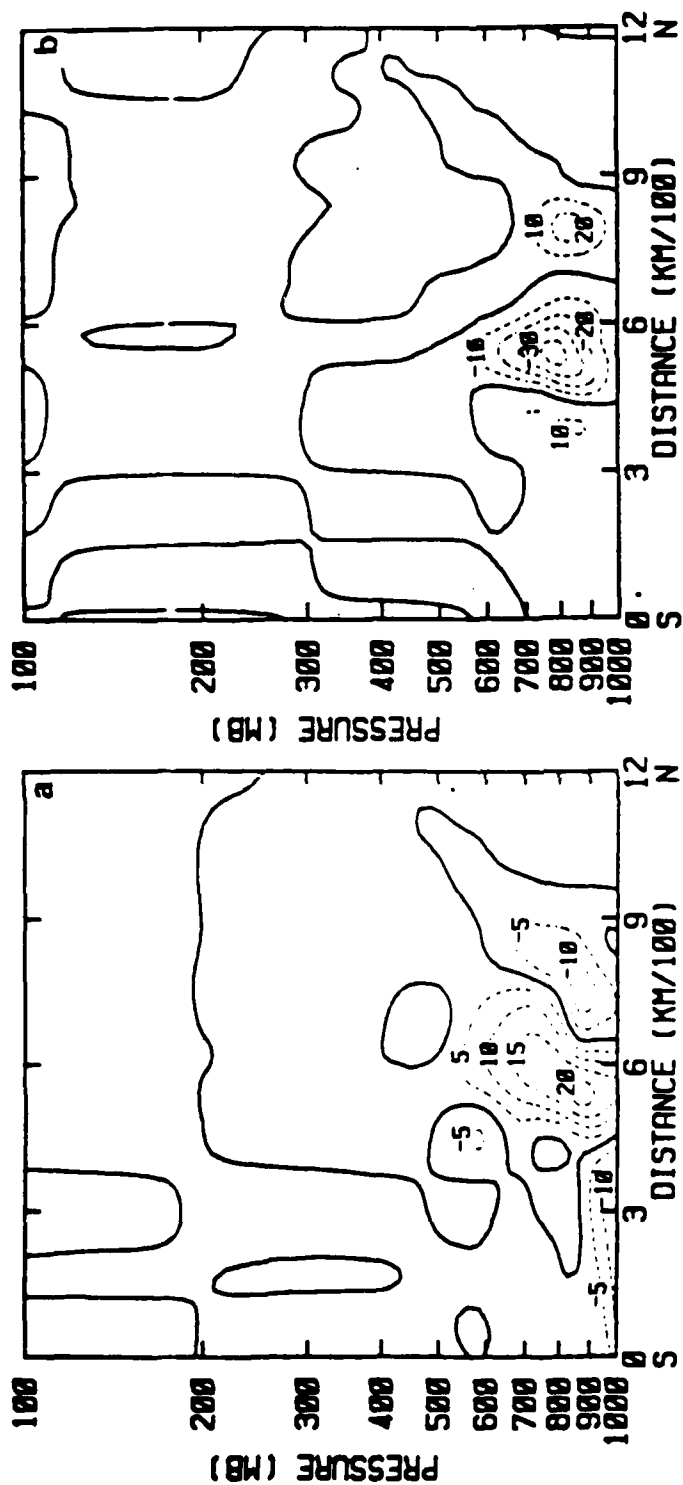
Fig. 3-14.   North-south cross-sections of (a) v-component and (b) ω for wave-number 40 in genesis jet. Contour interval is 5 m/s for v and 10 μbar/s for ω. Heavy solid line is zero contour in both cross-sections. Figures represent a subsection of the forecast domain. Southern edge of figures are 240 km south of the center of the forecast domain.

wave. That is, energy is gained from both KZ and AE. Although VCK is part of the barotropic term, it is considered a baroclinic process since it involves the vertical wind shear.

C. EFFECT OF WAVE-ZONAL FLOW INTERACTION

Although Gall (1976a) showed that the most unstable growth rate occurred at wavenumbers 12-15, the dominant scale of motion was eventually found to be wavenumbers 5-7. Subsequestly, Gall (1976b) included wave-zonal flow inter- action and surface friction effects. It was found that the growth rate in the lower troposphere exhibited the most rapid reduction due to increasing static stability and reduced vertical shear. Coupled with the effects of surface friction in the lower troposphere, short waves (wavenumbers 12-15) stopped growing earlier than longer waves which extended throughout the troposphere. Gall (1976b) concluded that wave interaction with the zonal flow plus surface friction modified the waves and the zonal flow so that wavenumbers 5-7 dominated the flow.

It was observed in the experiments with the genesis jet in the previous section, that after G40 had developed, other disturbances somewhat larger than wavenumber 40 developed. It was suspected that a maximum in the growth rate spectrum existed between wavenumber 8 and 40 for a slightly modified genesis jet. Therefore, in this section, the effects of

wave-zonal flow interaction are studied for the mean winter and genesis jets. These experiments (set B) differ from the previous experiments (set A) in the following way. First, the model is integrated in time until the linear growth rate of the waves ceases. This occurs at 120 h for the mean winter jet and at 84 h for the genesis jet. Second, the zonal means are computed for u, v, T and π from these forecast fields and are used as the initial fields. The growth of the waves in the modified mean winter and genesis jets is then calculated exactly as in the set A experiments.

The growth rates for the set B experiments are compared in Fig. 3-15 with those from set A. For the mean winter jet modified by the wave-zonal flow interaction the growth rates are reduced by 10-30% for wavenumbers greater than 9. There is a tendency for the growth rates of the highest wavenumbers to have the greatest reduction. Very significant changes occurred with the modified genesis jet. Here again, growth rates are reduced for all wavenumbers greater than 9 with the most significant reduction at the shortest wavelengths. In fact, the growth rate for wavenumber 40 decreased from 1.82 day^{-1} to 0.82 day^{-1}. In the previous section it was shown that this wave involves both baroclinic instability and Kelvin-Helmholtz instability. Stone (1966) and Orlanski (1968) demonstrated that R_i must be < 1 for the latter to exist and this condition was satisfied (cf, Fig. 3-2) for the set A experiments. However, the modified

63

Fig. 3-15. Linear growth rates for (a) mean winter and (b) genesis jets for set B experiments (heavy line) and for set A experiments (light line).

64

genesis jet for the set B experiment does not meet this condition. R_i values in the vicinty of the modified genesis jet in the lowest levels are in the range of 2-5 (Fig. 3-16), which is a small but significant increase relative to the set A experiment. This R_i increase is due to an increase of the static stability in the lowest levels. The decreased growth rates for the shortest waves are consistent with the increased R_i values (Stone, 1966; Orlanski, 1968; Staley and Gall, 1977). R_i values poleward of the jet in the lowest levels are unchanged from the set A experiments and remain less than 2.

The growth rate for wavenumber 20 for the genesis jet was not reduced as much as the other waves. In fact, the growth rate spectrum for the modified genesis jet exhibits a maximum at wavenumber 8 (1.17 day^{-1}) and also at wavenumber 20 (1.2 day^{-1}). It is suggested that the peak at wavenumber 20 did not appear in the A experiment due to the magnitude of the growth rate for the "mixed" baroclinic mode.

To study wavenumber 20 (G20), the model was initialized with just this wave in the domain. Here, a horizontal resolution of 50 km with 28 intervals in the x-direction and 128 intervals in the y-direction is used. The initial fields were generated as in the B experiments described earlier.
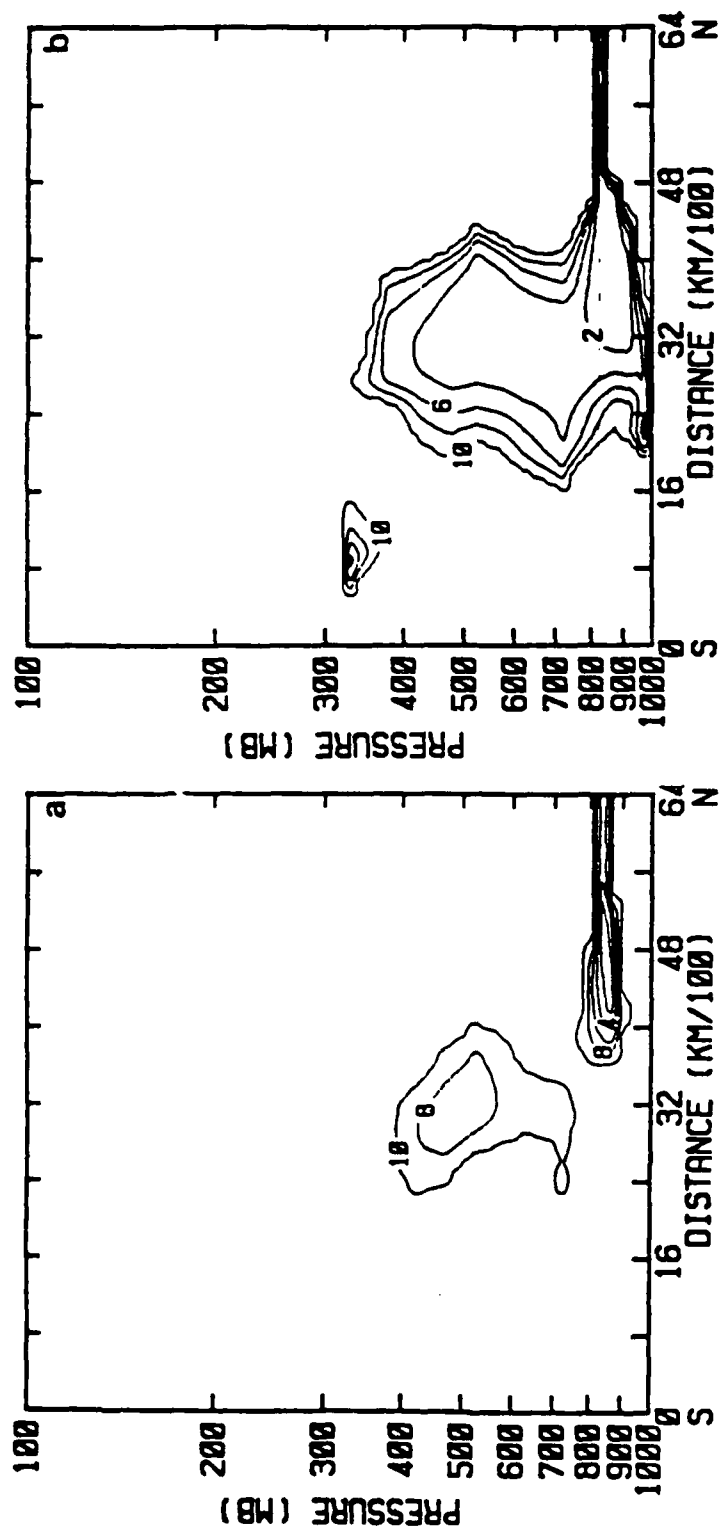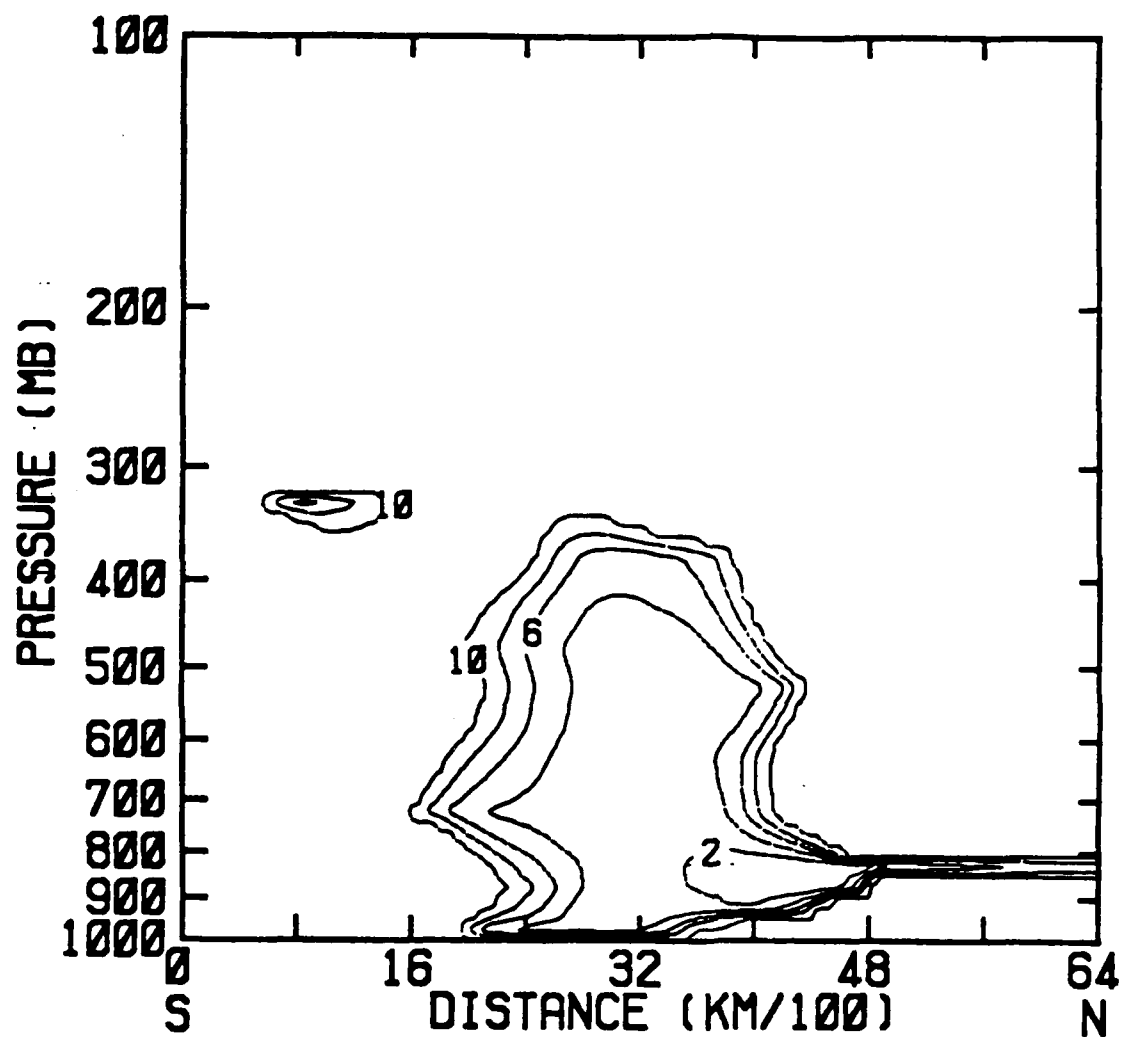
Fig. 3-16. Initial zonally-averaged Richardson number for modified genesis jet. Contour interval is 2. Values above 10 are not contoured.

The time evolution of CE, HCK and VCK for G20 is shown in Fig. 3-17. Term CE is dominant, which indicates that this wave receives energy through conventional baroclinic processes. Term VCK is also positive but is only one-fourth of CE. Term HCK is negative and about one-half the magnitude of VCK.

An east-west cross-section of vertical motion, temperature and trough position for G20 is given in Fig. 3-18. The trough tilts westward with height with the largest slope between 850 and 700 mb. The warmest air extends from the surface trough position to 750 mb with little or no tilt. Above 750 mb, the warmest air tilts to the west. With the strongest vertical motion occurring just east of the surface trough position, generation of KE is a maximum in the lowest 250 mb. This pattern is similar to that observed in G40 in the previous section and is consistent with the shallow nature of G20 and G40 compared to W12 and G8.

The surface pressure pattern for G20 is shown in Fig. 3-19. A well-defined surface low develops about 1000 km north of the jet stream. Although the horizontal scale of G20 is smaller than that of extratropical, synoptic-scale waves, surface pressure patterns in both waves are similar. In addition, the energetics for both waves are similar with large positive CE and smaller, negative HCK.

air-sea temperature difference fields are shown with the individual experiments. Surface vapor pressures are the saturation values corresponding to the sea-surface temperatures. Sea-surface temperature and moisture values remain constant over each forecast.

The diabatic runs use the complete model while the adiabatic runs neglect precipitation physics and sensible and latent heating within the PBL. Also, the adiabatic runs utilize the surface momentum fluxes to incorporate surface friction and the surface heat flux to predict the PBL depth even though the sensible heating due to the surface heat flux is not added to the temperature field.

A. WAVE GROWTH AND STRUCTURE

A graph of the minimum central pressure versus time of G20 for both the adiabatic (G20A) and diabatic (G20D) simulations is given in Fig. 4-1. The inclusion of diabatic effects results in G20D attaining a central pressure of 984 mb, which is 19 mb lower than G20A. Clearly, diabatic effects serve to intensify the disturbance. This is expected based on the studies of Bullock and Johnson (1971), Tracton (1973), Gall (1976c) and Sanders and Gyakum (1980).

Mullen (1983) computed deepening rates for several Pacific polar lows according to the method proposed by Sanders and Gyakum (1980), who defined 1 Bergeron (B) as a central pressure fall of 1 mb h^{-1} for 24 h at 60° latitude.

presented in Appendix C. The results of the experiments in Appendix C are used for comparison of the polar low to an extratropical synoptic-scale system.

The following procedure is used to incorporate the initial perturbation into the fields for the model simulations. First, the perturbation for a single wave is imposed in the initialized fields in the manner described in Chapter II (i.e., constant amplitude in the vertical). Second, the model is integrated for 36 h with the initial zonal mean values of u, v, T, q and π restored every time step under inviscid, adiabatic conditions. This allows the wave to reach the point at which exponential growth starts as in the Chapter III experiments. This insures the proper vertical structure of the wave at the initial time. These 36 h forecast fields serve as the initial fields for all simulations presented here.

The sea-surface temperature for these experiments is computed as follows. The mean air-sea temperature difference given by Mullen (1979) for the genesis conditions is interpolated to the forecast grid in the same manner as for the u-component described in Chapter II. Mullen (1979) found the maximum air-sea temperature difference of 6.8°C to be approximately 750 km north of the jet axis and decreased to about 4.5°C to the north and to about 2°C south of the jet axis. This difference is added to the lowest level initial temperature field. The sea-surface temperature and

80

IV. NONLINEAR MODEL SIMULATIONS

It was shown in Chapter III that the linear growth rates for both the mean winter and genesis jets are largest for relatively large (wavenumber 8-9) baroclinic waves when frictional effects and wave-zonal flow interaction are considered. In addition, the genesis jet exhibits large growth rates for two smaller-scale systems. The first, wavenumber 40, was found to be very shallow and forms through baroclinic and Kelvin-Helmholtz instabilities. After this wave modifies the zonal flow in the vicinity of the jet, a peak in the growth rate spectrum occurs at wavenumber 20 (1400 km). This particular wave, G20, forms through conventional baroclinic instability and resembles the Pacific polar low described by Reed (1979) and Mullen (1979). However, the vertical scale of G20 is smaller than observed for the Pacific polar low.

The development and structure of G20 will now be studied in detail. This will be accomplished through the examination of model output and energy budgets of the storm at various stages of development for both adiabatic and diabatic simulations. The model configuration to study these waves is the same as that used in studying the energy transfer in these waves in Chapter III (Table 3-1). A similar study of wavenumber 8 for the genesis jet is

The second major point is that the linear growth rate
spectrum is strongly affected by processes which act to
continuously modify the initial zonal flow. The processes
tested here include wave-zonal flow interation and surface
friction. It was found that surface friction damps all
wavelengths, but is especially effective in damping the
shortest waves. In addition, surface friction shifted the
most unstable wavenumber for the mean winter jet from wave-
number 12 to 9. It was also found that wave-zonal flow
interaction modified the shortest waves the most and led to
a significant change in the growth rate spectrum for the
genesis jet. The baroclinic/Kelvin-Helmholtz wave was
damped considerably, as the growth rate was reduced from
1.82 day-1 to 0.82 day-1. This was due to an increase in
the low-level R_i values from less than 1 to values of 2-5.
The modified genesis jet exhibited maximum growth rates at
wavenumbers 8 and 20. It was found that wavenumber 20 was a
baroclinic wave with maximum amplitude in the lowest level
and resembles the Pacific polar low described by Reed (1979)
and Mullen (1979). In addition, this wave is not as deep as
the longer baroclinic waves, with the maximum upward motion
occurring at 800 mb as opposed to 750 mb for the longer
waves. Friction is found to damp wavenumber 20 strongly,
which suggests that polar lows cannot attain observed
intensities through baroclinic instability alone.

the growth rate spectrum of the original genesis jet such that the synoptic-scale wave dominates. Clearly, the development of a polar low must involve processes other than baroclinic instability to attain observed intensities. The effect of diabatic processes on the polar low will be studied in Chapter IV.

E.   CHAPTER SUMMARY

The experiments described in this chapter lead to two important points. First, significant differences exist in the growth rate spectrum for the two jet profiles. It was found that the mean winter jet yields a maximum growth rate for wavenumber 12 (0.59 day^{-1}). This result supports the findings of Gall (1976a), who computed linear growth rates for a mean zonal flow similar to the mean winter jet. He found wavenumbers 12-15 to be most unstable with a growth rate of 0.6 day^{-1}. In addition, the shape of the curve in Fig. 3-1 for the mean winter jet is quite similar to that given by Gall (1976a), who included only wavenumbers < 15. The genesis jet case yields a maximum growth rate for wavenumber 8 (1.22 day^{-1}) and 40 (1.82 day^{-1}). It was shown that wavenumber 12 for the mean winter case and wavenumber 8 for the genesis case are baroclinic waves which extend throughout the troposphere. However, wavenumber 40 was found to be a baroclinic/Kelvin-Helmholtz wave which is confined to the surface-750 mb layer and is characterized by a helical type circulation about a horizontal axis.

77
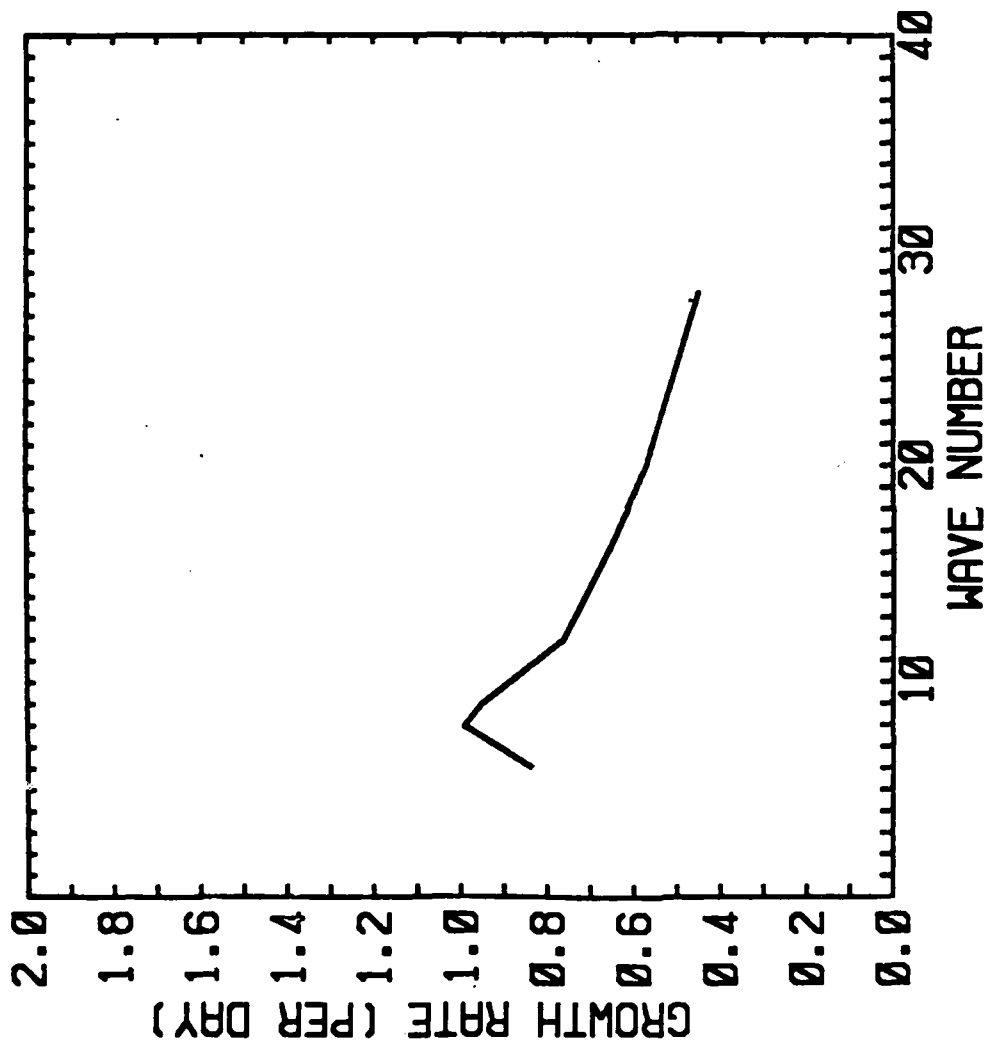
Fig. 3-21. Linear growth rates for modified genesis jet with friction included.

have their largest amplitude in the lowest level. Growth
rates for wavenumbers 6 and 9 for the mean winter jet and
wavenumber 6 for the genesis jet are reduced by less than
10%. All other growth rates are reduced over 15%. Growth
rates for wavenumbers greater than 18 for the mean winter
jet could not be calculated because these perturbations were
strongly damped.

The most unstable waves for the mean winter jet in the
C experiments is wavenumber 9 with a growth rate of 0.48
day^{-1}. Therefore, the effect of friction on the mean winter
jet is to shift the most unstable wave to a longer wave-
length (wavenumber 12 in set A versus wavenumber 9 in set C
experiment). For the genesis jet, a maximum occurs at wave
number 8 (1.04 day-1) as in the set A experiments and at
wavenumber 36 (1.38 day-1). The growth rate spectrum for
the genesis jet is very flat for wavenumbers greater than
24, which suggests that the helical rolls formed in the
"mixed" baroclinic wave tend to be larger when frictional
effects are included.

The growth rates for the modified genesis jet with
linearized friction (experiment D) are shown in Fig. 3-21.
Again, the shortest wavelengths are most highly damped with
the growth rates for wavenumbers greater than 28 too small
to calculate. The peak in the growth rate spectrum is 0.99
day-1 at wavenumber 8. This indicates that the combination
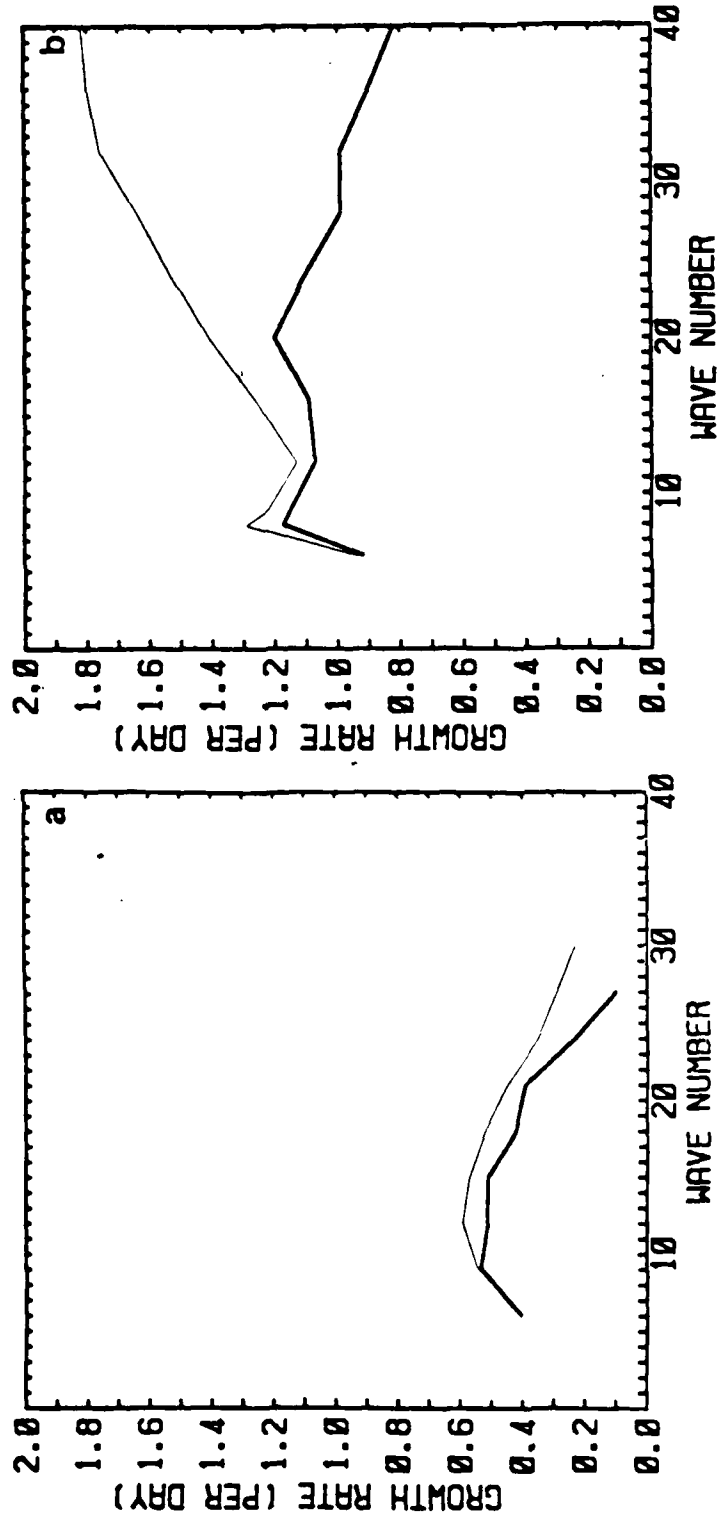of wave-zonal flow interaction and surface friction alter

75
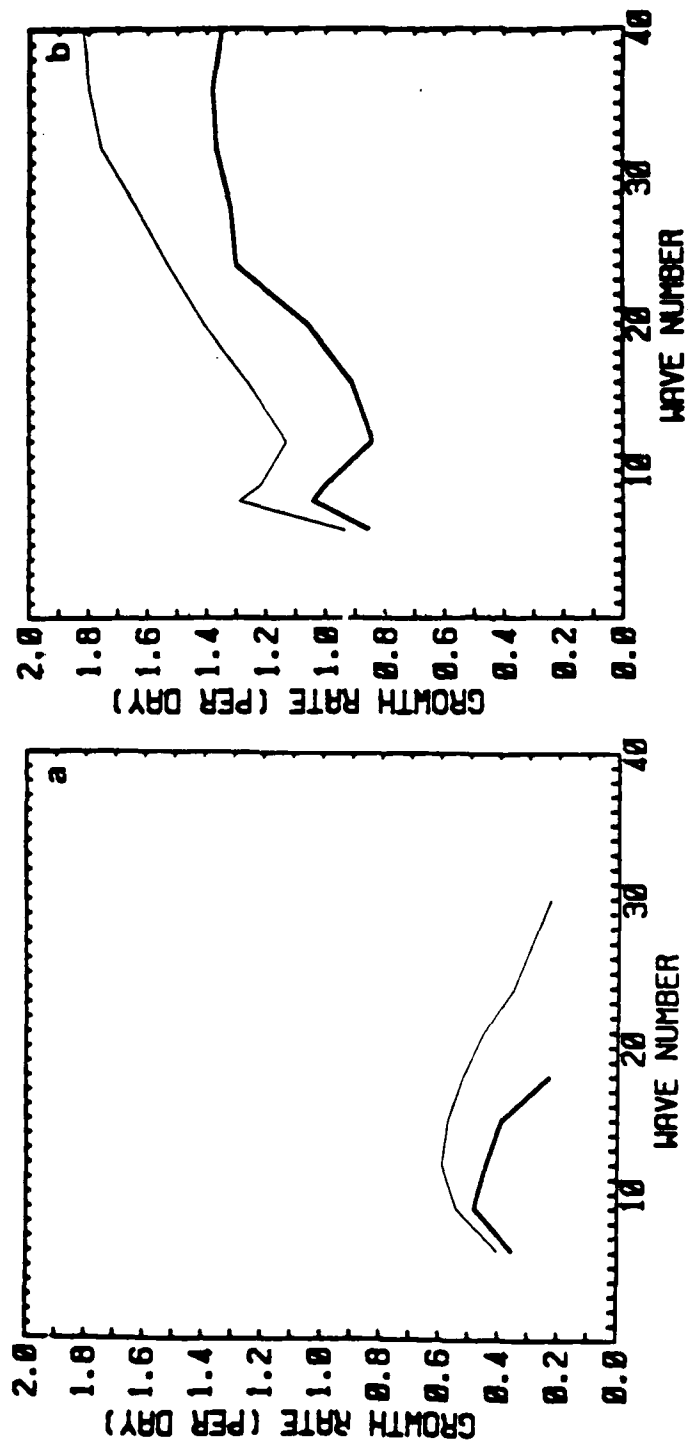
Fig. 3-20. Linear growth rates for (a) mean winter and (b) genesis jets for set C experiments (heavy line) and for set A experiments (light line).

74

D. EFFECT OF FRICTION

An experiment (set C) similar to those described in the previous two sections is performed to study the effect of friction on the linear growth rates. These C experiments differ from the set A experiments in that the surface friction is included. The zonal mean quantities of u, v, T and π are again restored each time step.

The incorporation of friction in the C experiments differs from the form described in Appendix A. Here, the surface stress is

$$\tau = \rho C_D \; |V|V \qquad\qquad\qquad (3.3)$$

where $C_D = 1.0 \times 10^{-3}$. It is assumed that the surface stress decreases to zero linearly with pressure through the lowest two model layers (approximately 120 mb). This formulation of the surface friction is used to provide linear friction over the entire grid. Although this form is proportional to the velocity squared, interactions with the zonal flow are zero since the zonal flow is held constant in time. The interactions between waves is small since the perturbation is small.

The major effect of the friction is to decrease the growth rate of all the waves (Fig. 3-20). Also, the shortest waves are most highly damped, which is consistent with Gall (1976b) and Gall et al. (1979). This is expected since the short waves have been shown to be shallow and to

73

instability creates a structure different from the observed structure of polar lows. Wave G20 is barotropically damped since HCK < 0.

The results for the genesis jet disagree with the findings of Sardie and Warner (1983). Using a 3-layer quasi-geostrophic model, they found the most unstable wavelength to be 2700 km (about wavenumber 10) with a growth rate of 1.29 day-1. They did not find large growth rates for the "mixed" baroclinic wave (G40) because quasi-geostrophic models neglect the non-geostrophic effects necessary for Kelvin-Helmholtz instability. Sardie and Warner (1983) showed that inclusion of moist processes shifted the most unstable wave to shorter wavelengths (600-2300 km depending on the heating distribution) and concluded that moist baroclinic processes are the primary cause of Pacific polar lows.

The growth rates computed in this study for the modified genesis jet indicate that moist processes may not be necessary for polar lows to form. Mullen (1982) documented a case of deep continental polar low development with a scale of 1800 km in a domain with negligible water content. The formation of a polar low with this horizontal scale and without moist processes is consistent with the findings of this study. Some other process(es) (possibly terrain induced) must be responsible for the deep structure of the continental systems observed by Mullen (1979).

Striking similarities exist between wavenumber 20 for the modified genesis jet (G20) and the observations of Pacific polar lows by Reed (1979) and Mullen (1979). Reed (1979) observed that the polar low has typical wavelengths from 1000-1500 km. Wave G20 has a wavelength of 1400 km. Mullen (1979) presented composited data which exhibited R_i values of 1-2 at the position of the polar low from the surface to 850 mb. This has also been found to be the case for G20 (cf, Fig. 3-16). Mullen (1979) also showed that the polar low formed 500-700 km north of the jet while G20 formed about 1000 km north of the jet. Differences exist between the vertical structure of observed polar lows and G20. Reed (1979) documented a Pacific polar low which exhibited geopotential perturbations at 300 mb as large as those observed at the surface. G20 has been found to exhibit maximum amplitude at the surface with little evidence of the wave above 500 mb. It has been shown by Gall (1976c) that latent heat release can serve to deepen systems. This process will be examined in Chapter IV.

It has been demonstrated that G20 is formed by conventional baroclinic instability which supports the hypotheses of Reed (1979) and Mullen (1979) that Pacific polar lows are baroclinically unstable disturbances. Energy conversion processes suggest Kelvin-Helmholtz instability is a contributing factor, but it is about four times smaller in magnitude than CE. In addition, the Kelvin-Helmholtz
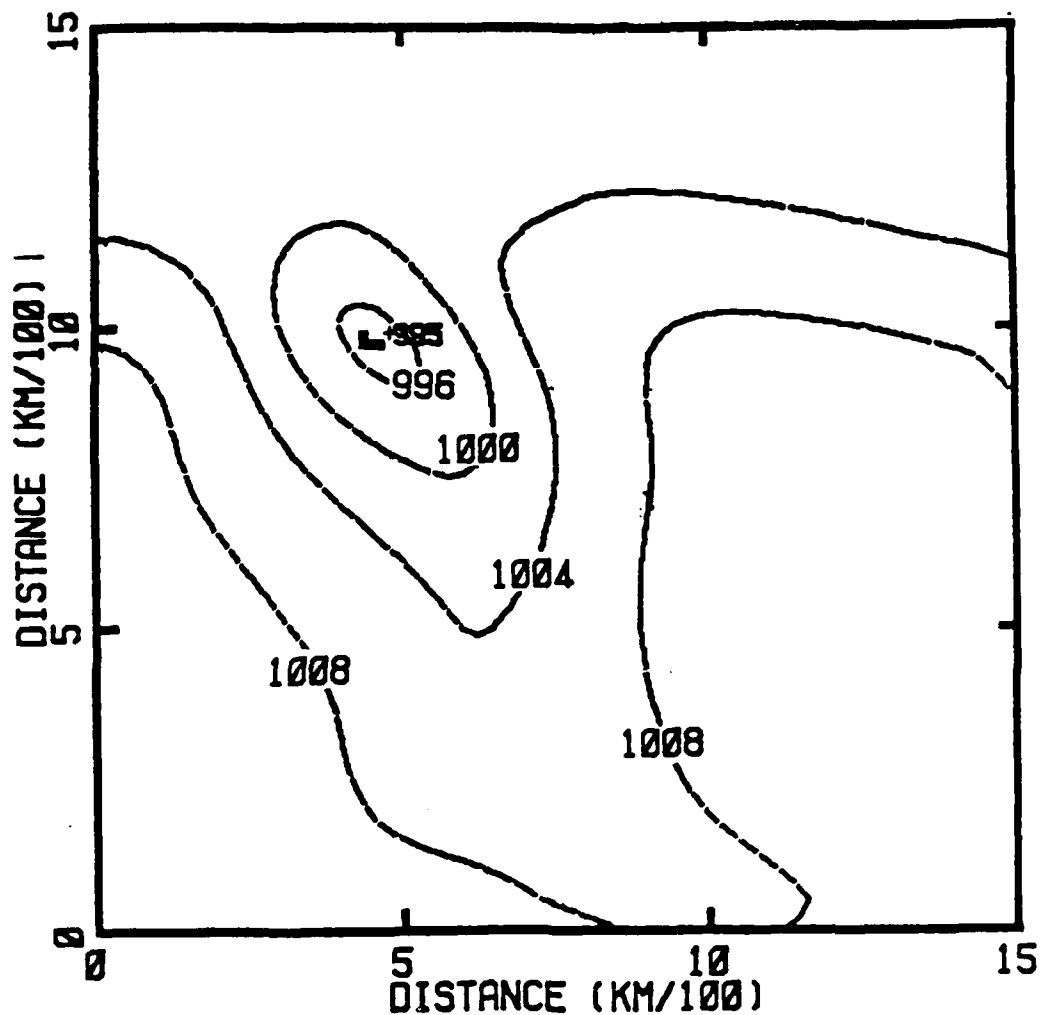
Fig. 3-19. Surface pressure at 84h for wavenumber 20
in modified genesis jet. Contour interval is
4 mb. Figure represents a subsection of the
forecast domain. Southern boundary of figure
is at the center of the forecast domain.
100 km of right side of domain is the same
as leftmost 100 km due to periodicity.
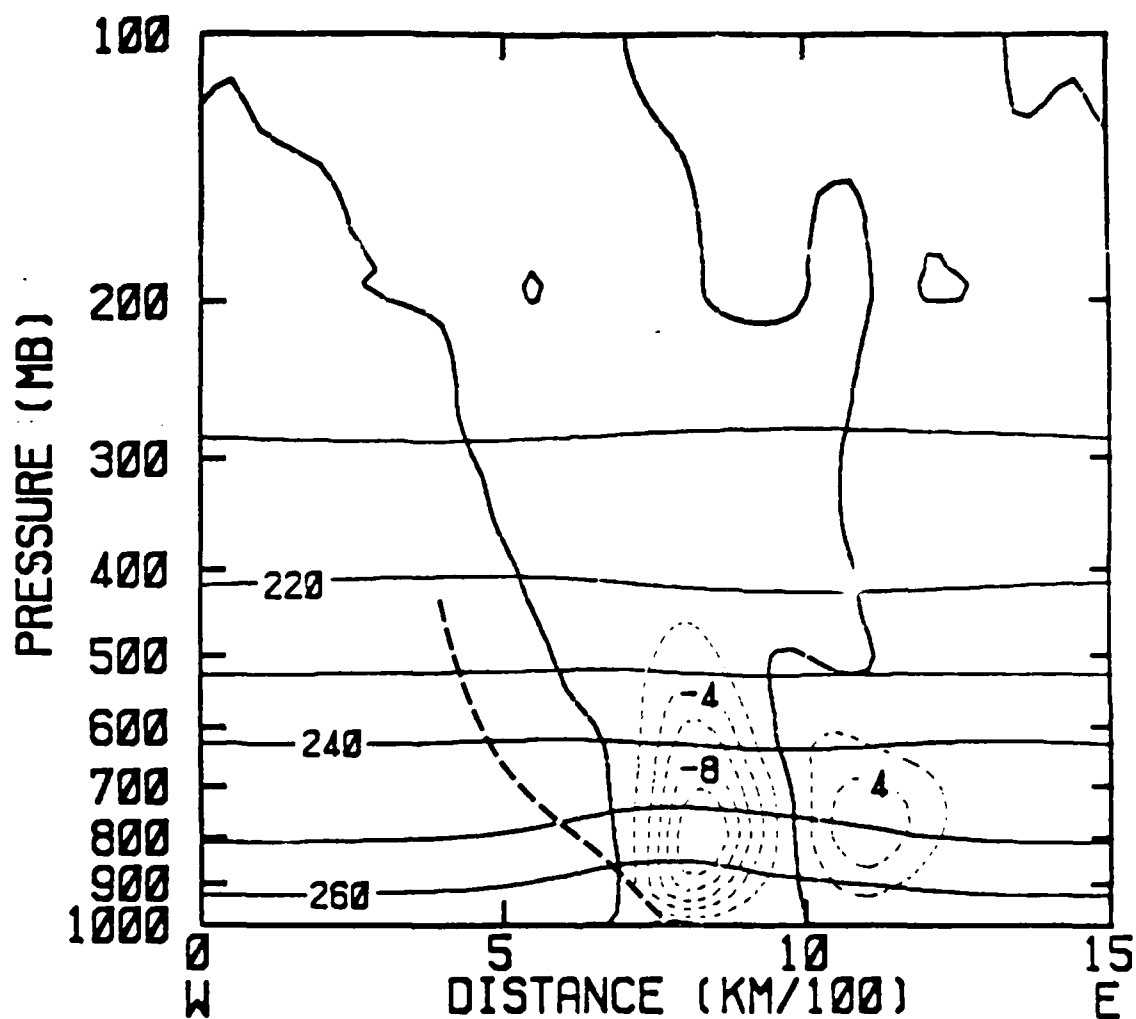
Fig. 3-18. Similar to Fig. 3-10 except for wavenumber 20
in modified genesis jet. Contour interval is
2 μbar/s for ω and 10 K for T. 100 km of right
side of domain is the same as the leftmost
100 km due to periodicity.

69
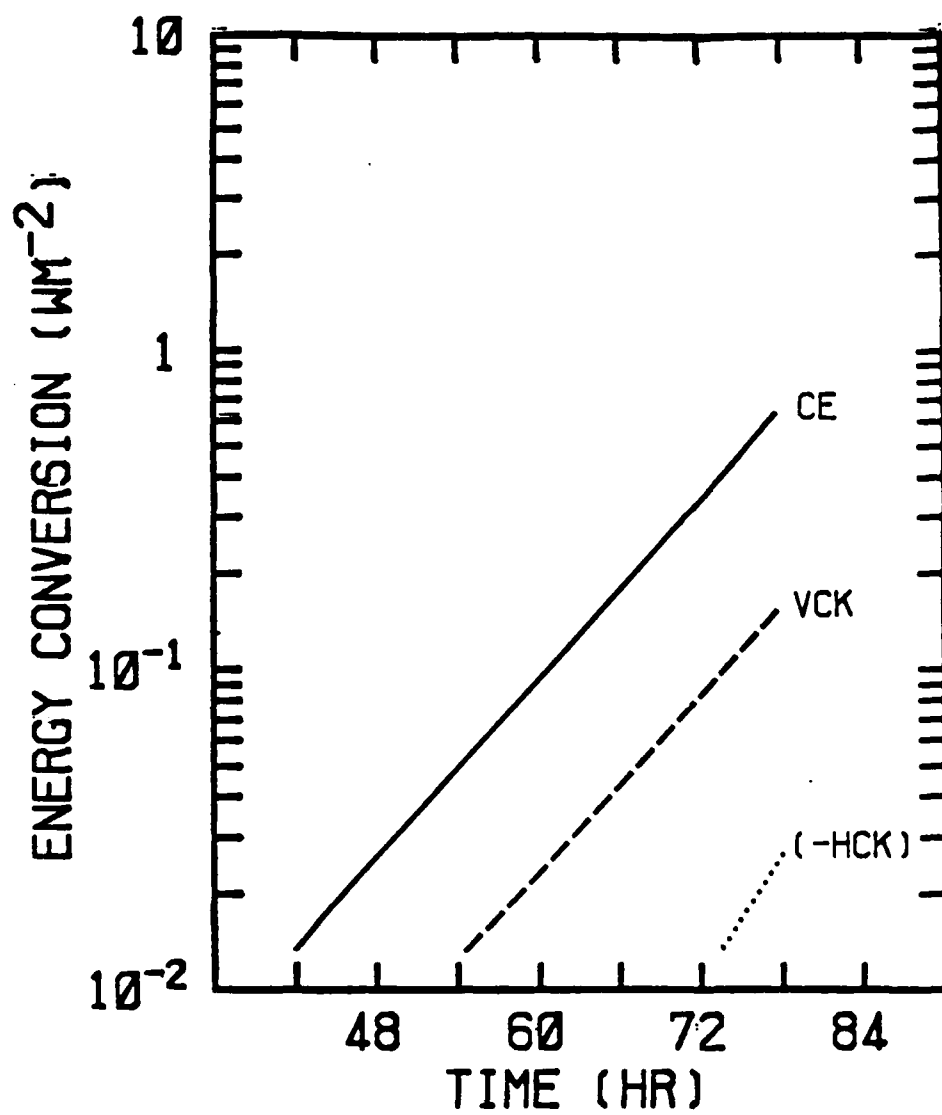
Fig. 3-17. Similar to Fig. 3-7 except for wavenumber 20 in modified genesis jet.
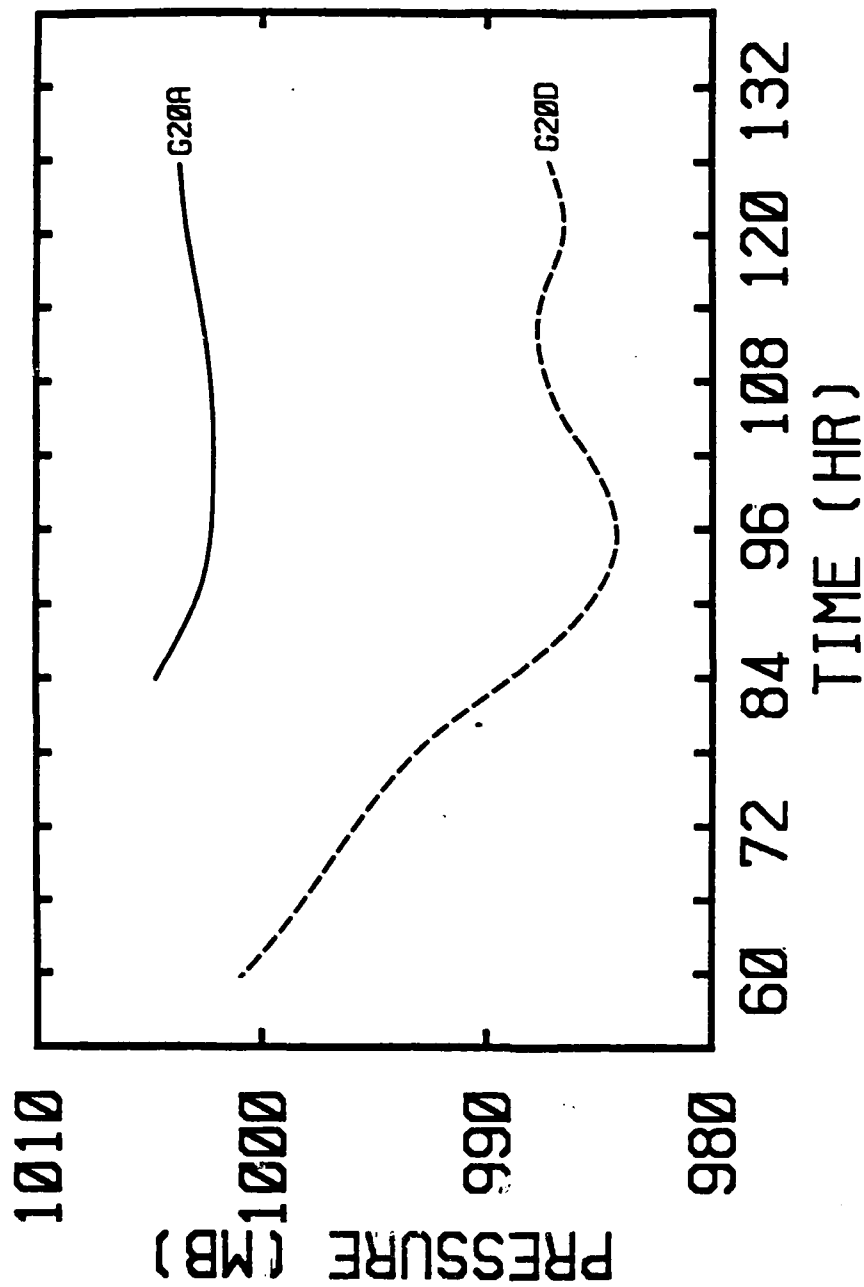
Fig. 4-1. Minimum central pressure for G20A (solid) and G20D (dashed).

The deepening rate at any latitude ϕ, is adjusted by multi-
plying by sin 60°/sin ϕ. Here G20D exhibits a 13 mb fall
in 24 h near 52N, which corresponds to a deepening rate of
0.6 B. The maximum deepening rate for G20A is 0.22 B.
Mullen (1983) showed that Pacific polar lows can achieve
deepening rates of about 1.9 B, although this seems to occur
only when the polar low interacts with the main frontal band
equatorward of the deepening low. For a polar low which
did not interact with the main polar front, Mullen found a
deepening rate of 0.85 B. This corresponds well with the
deepening rate computed here for G20D. Observed deepening
rates, such as those computed by Mullen, should be expected
to be larger than those computed in this study. Pacific
polar lows generally deepen as they move into a large area
of low pressure often centered in the Gulf of Alaska.
Therefore, some of the pressure fall must be attributed
to the new environment of the storm, rather than actual
intensification of the individual cyclone. This "change of
environment" did not exist in G20D and therefore, deepening
rates computed using real data could very well be larger
than those computed here.

The sea-level pressure fields at 60, 72, 84 and 96 h for
G20A and G20D are shown in Figs. 4-2 and 4-3, respectively.
During intensification, the low center in G20D (hereafter
G20D) moves due east while G20A moves toward the east-
northeast. At 96 h, the center in G20A is about 200 km

83
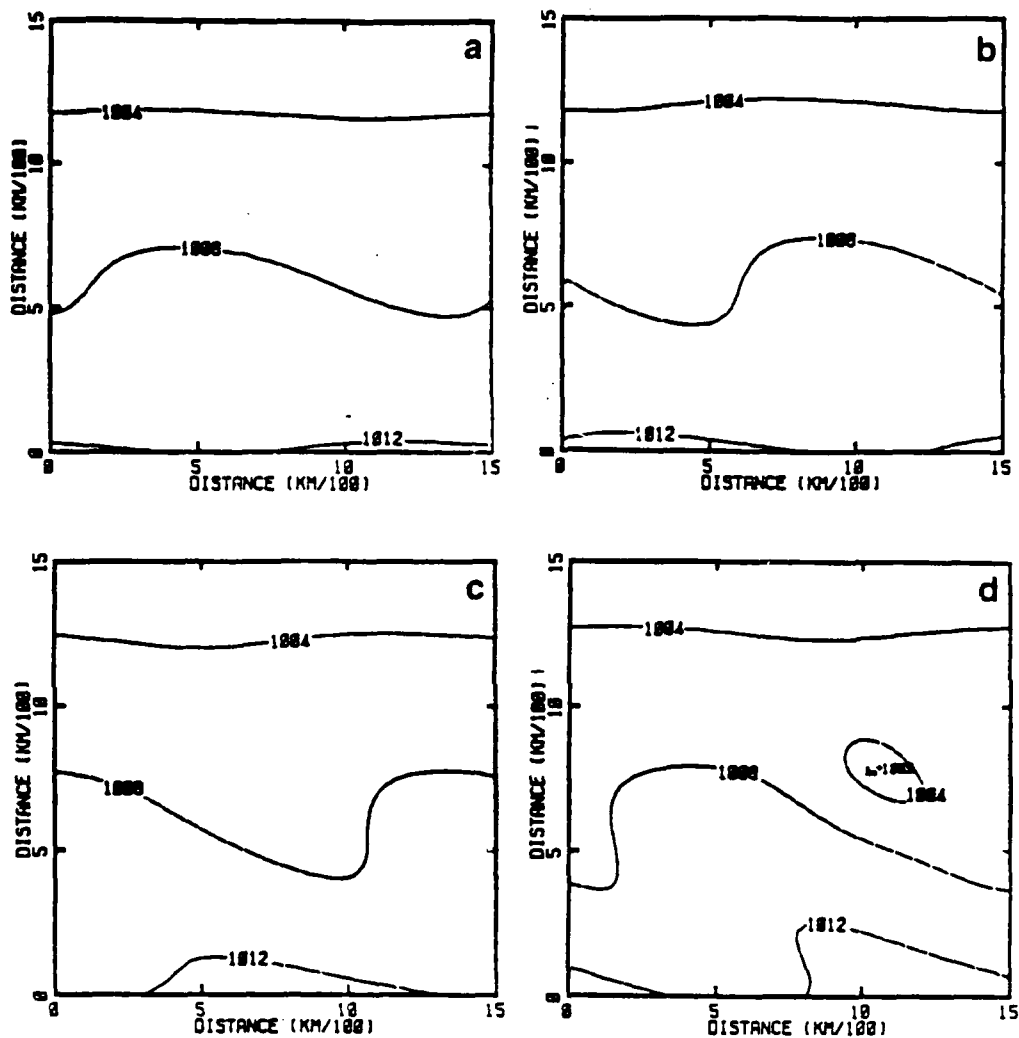
Fig. 4-2.   Sea-level pressure fields for G20A at (a)
             60 h (b) 72 h, (c) 84 h and (d) 96 h. Figures
             represent a subsection of forecast domain.
             Southern boundary of figure is located 200 km
             north of center of forecast domain. 100 km of
             right side of domain is the same as the leftmost
             100 km due to periodicity.

84
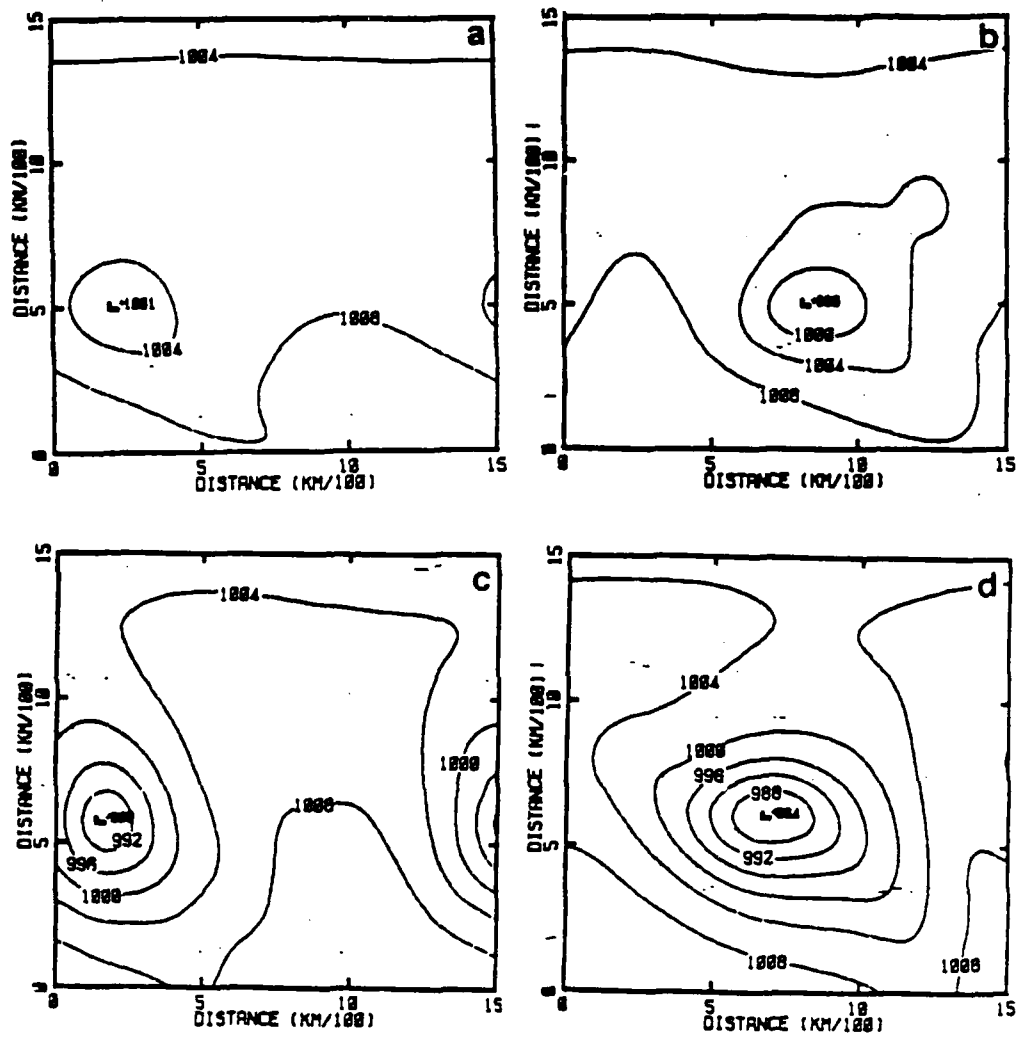
Fig. 4-3.   Similar to Fig. 4-2 except for G20D.

north of the corresponding position of G20D. Since diabatic processes are included in G20D, it is suspected that the sea-surface temperature (Fig. 4-4) plays a role in determining the position of the low. Sanders and Gyakum (1980) demonstrated that strong oceanic development tends to occur near the maximum gradient of the sea-surface temperature. Here, it is clear that during the developing stages, the center in G20D remains in the region of maximum gradient of sea-surface temperature (near the 6°C isotherm), while the center in G20A moves away from it.

The low in G20A is observed to form about 900-1000 km north of the jet axis while the low in G20D forms about 750 km north of the jet axis. This is consistent with the composite results of Mullen (1979), which indicated that the polar low forms 500-700 km north of the jet. Therefore, realistic deepening rates and more realistic storm positions are produced when diabatic effects are included.

Both G20A and G20D exhibit a band of positively correlated u' and ω' similar to that in G40 (cf, Fig. 3-13) parallel to the trough extending from the low center. In this region, the $R_i < 1$, which suggests that Kelvin-Helmholtz instability may be significant near the trough.

East-west cross-sections of height perturbations at 84 h are given in Fig. 4-5 for G20A and G20D. These figures are representative of the developing stages of the disturbance.

86
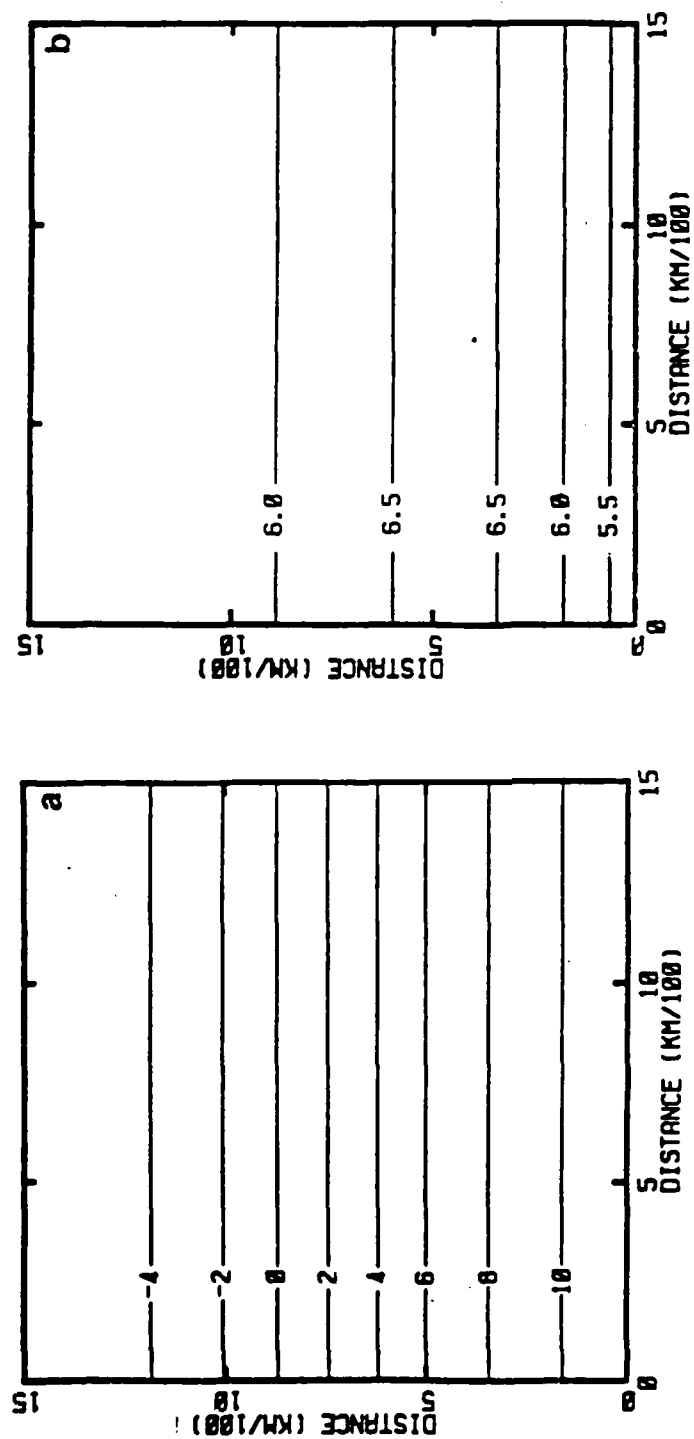
Fig. 4-4.   Fields of (a) sea-surface temperature and (b) air-sea
temperature difference for G20A and G20D. Contour
interval is 2°C in (a) and 0.5°C in (b). Grid placement
as in Fig. 4-2.

87
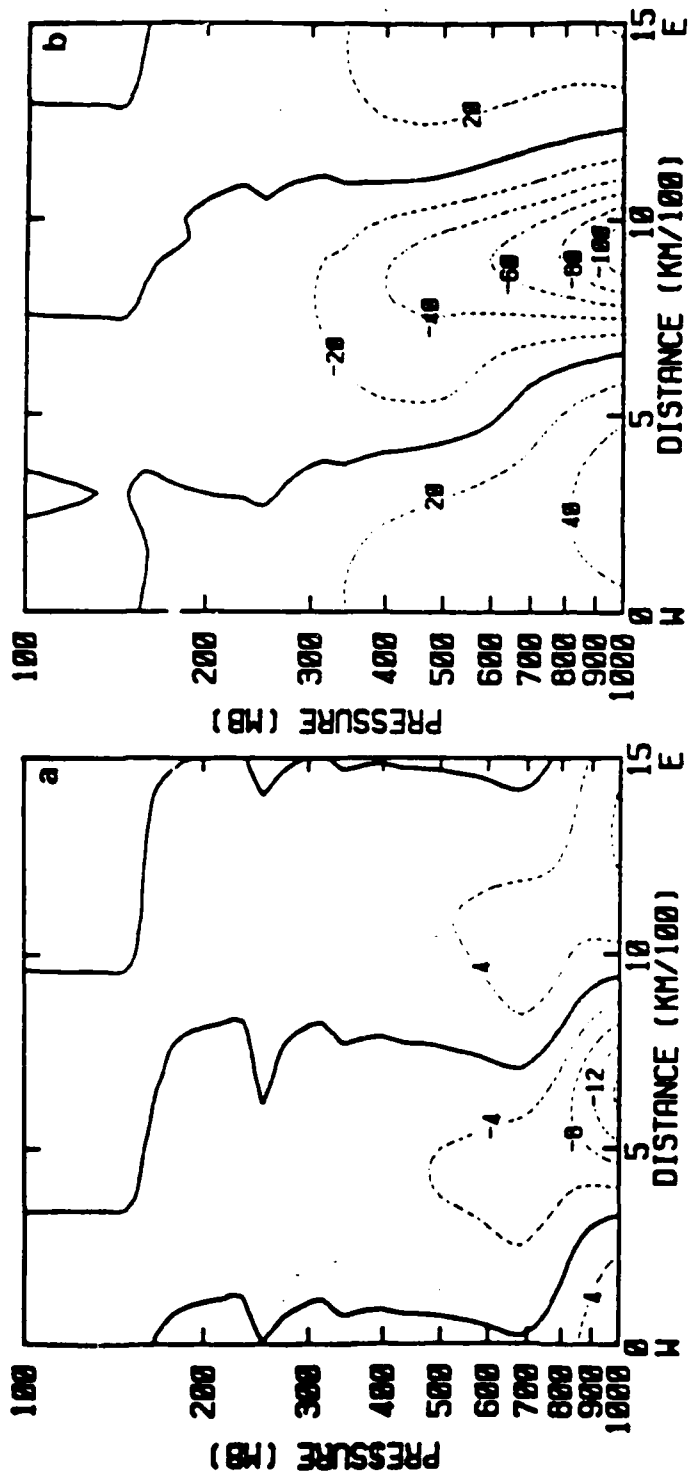
Fig. 4-5. East-west cross-sections of height perturbations for (a) G20A and (b) G20D at 84 h. Contour interval is 2 m in (a) and 10 m in (b). Heavy dark line is zero contour. 100 km of right side of domain is the same as the leftmost 100 km due to periodicity.

G20A exhibits a maximum deviation at the surface of about 16 m. The wave is damped strongly in the vertical so that the amplitude at 800 mb is only 50% of the surface value. G20D is noticeably stronger with a surface maximum amplitude of 110 m. The amplitude does not decrease as rapidly in the vertical as in G20A. The amplitude at 500 mb is about one-half the surface amplitude.

Since G20D extends through a greater depth than G20A, it should be expected to have a phase speed greater than that of G20A. Phase speeds computed from the surface pressure centers in Figs. 4-2 and 4-3 are 12.4 m s^{-1} for G20D and 8.2 m s^{-1} for G20A. Some of the increase in phase speed of G20D must also be due to it being imbedded in stronger flow along the more southern track.

East-west cross-sections of vertical motion and temperature at 84 h are shown in Fig. 4-6. The reason for the increased vertical scale in G20D becomes obvious upon inspection of the ω and T fields. For G20A, the warmest air extends upward from the surface to about 750 mb with little or no tilt. The maximum vertical motion occurs just east of the warmest air, which favors generation of KE. Above 750 mb, the warmest air tilts to the west with height away from the maximum vertical velocity similar to the pattern exhibited by wavenumber 20 in the linear experiments in Chapter III. In addition, the temperature perturbation decreases above 750 mb. These factors are consistent with a
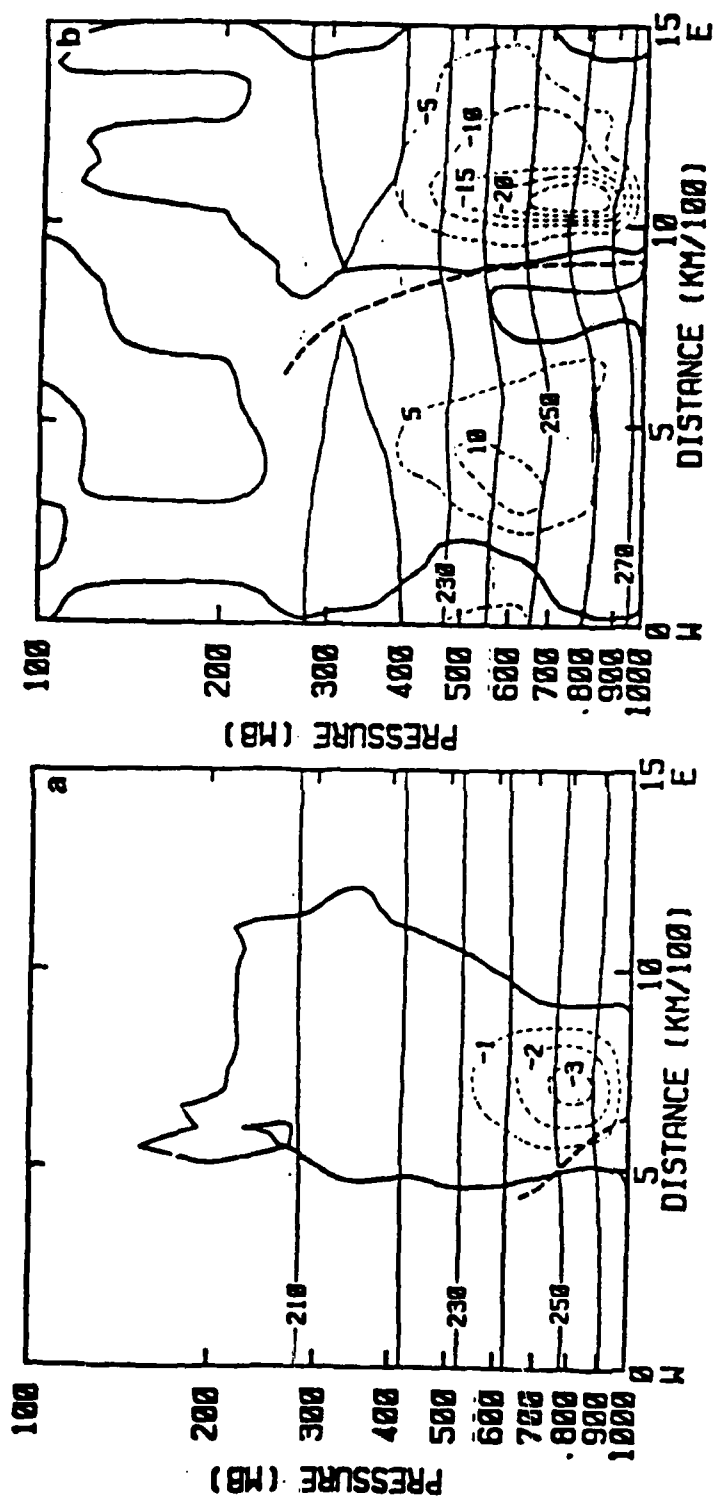
Fig. 4-6. East-west cross-sections of ω (dashed line; heavy solid line is zero contour), T (light solid line) and trough position (heavy dashed line) for (a) G20A and (b) G20D at 84 h. Contour interval for ω is 1 µbar/s in (a) and 4 µbar/s in (b). Contour interval for T is 10 K.

reduced generation or even a destruction of KE above 750 mb.
This will be discussed further in the next section. The
structure of G20A strongly resembles that of G20 in the
linear experiments in Chapter III. This is not surprising
since no other waves are included in these studies, and
since the disturbance is relatively weak, wave-zonal flow
interaction is small. In contrast to the vertical structure
of G20A, the low in G20D exhibits a strong positive tempera-
ture maximum which extends from the surface to 450 mb with
little or no tilt. This results in a generation of KE over
a much deeper layer than in G20A.

One reason for the increased depth of the temperature
perturbation in G20D can be seen by examining Fig. 4-7,
which shows the amount of total , convective and stable
precipitation that accumulated during the 12 h period ending
at 84 h. A maximum of precipitation (about 22 mm) is found
at and just ahead of the path of the low center with a
secondary maximum (about 15 mm) south of the low along the
front. About 70% of the precipitation occurring near the
low center and about 85% in the southern maximum is convec-
tive. Based on cross-sections of θ_e and relative humidity
(not shown), conditional instability extended up to about
500 mb while stratiform clouds (relative humidity $\geq$ 100%)
extended up to about 350 mb in the warm sector ahead of the
low. The release of latent heat over this depth is consist-
ent with the warming observed in G20D ahead of the low. The
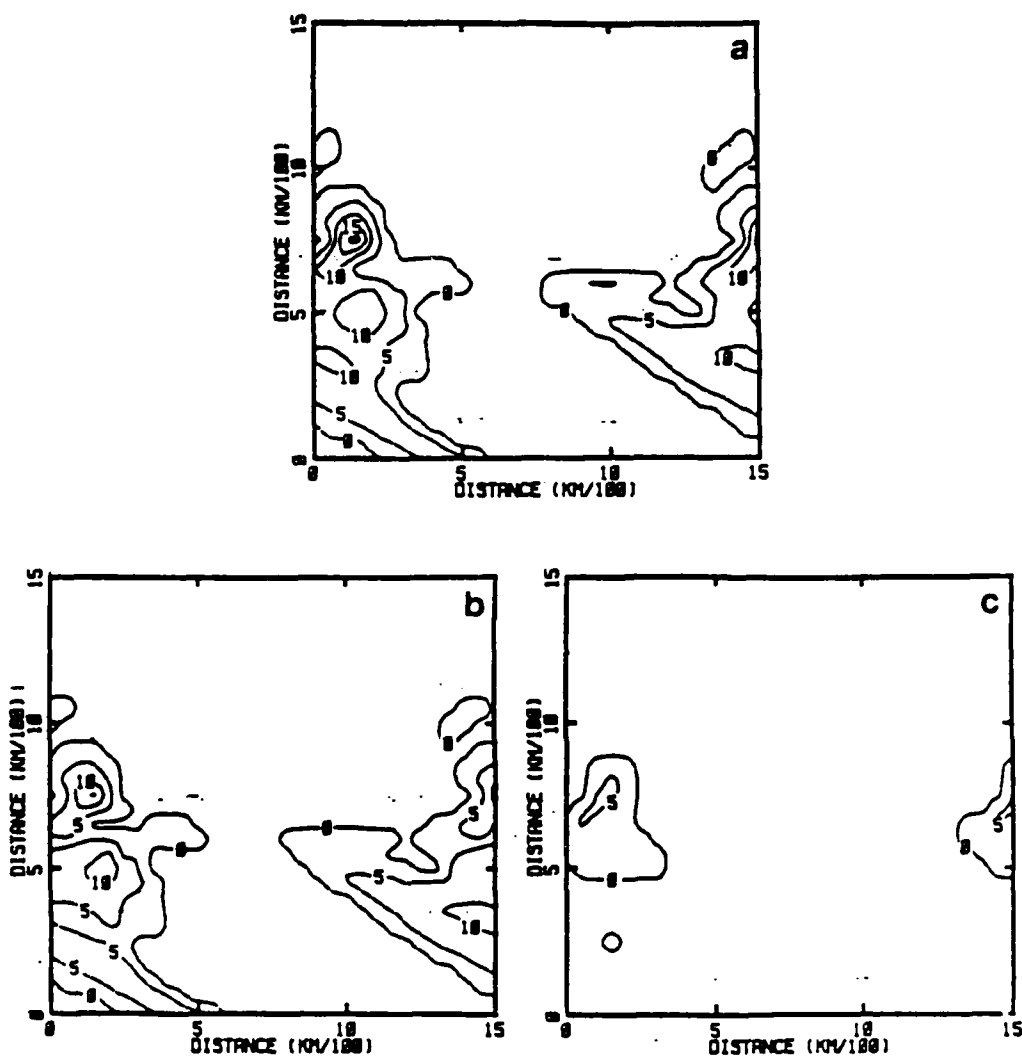
Fig. 4-7.   12h accumulation of (a) total, (b) convective
and (c) stable precipitation in a fixed-frame
reference ending at 84 h for G20D. Contour
interval is 5 mm. Grid placement as in
Fig. 4-2 .

diabatic heating effectively reduces the amount of adiabatic cooling in the region of ascent.

To separate the effects of latent heat release by precipitation from the PBL diabatic processes, a simulation (G20E) was made which was similar to G20D except that latent heat release by precipitation was not allowed. G20E attains a minimum central pressure of 993 mb (Fig. 4-8), which is 10 mb lower than the adiabatic simulation, but 9 mb higher than the fully diabatic simulation. Obviously, latent heat release by precipitation is not acting alone in the intensification of G20D. Significant contributions to the intensification of the polar low are made by three other processes. First, the sensible heating due to the large air-sea temperature difference insures a strong meridional low-level temperature gradient (i. e., baroclinity) over a longer time period than found in the adiabatic simulation. Second, the sensible heating within the PBL can be realized in the mid-levels almost immediately through dry convective adjustment. This is because the lapse rate is nearly dry adiabatic in the genesis jet from the surface to near 750 mb in the vicinity of the polar low. Third, the large, initial air-sea temperature difference acts to maintain a nearly dry adiabatic lapse rate in the lowest troposphere (i.e., low R_i) which should increase the growth rates of the shorter waves (Staley and Gall, 1977). To show the influence of the surface heat flux, G20E was rerun without a perturbation in
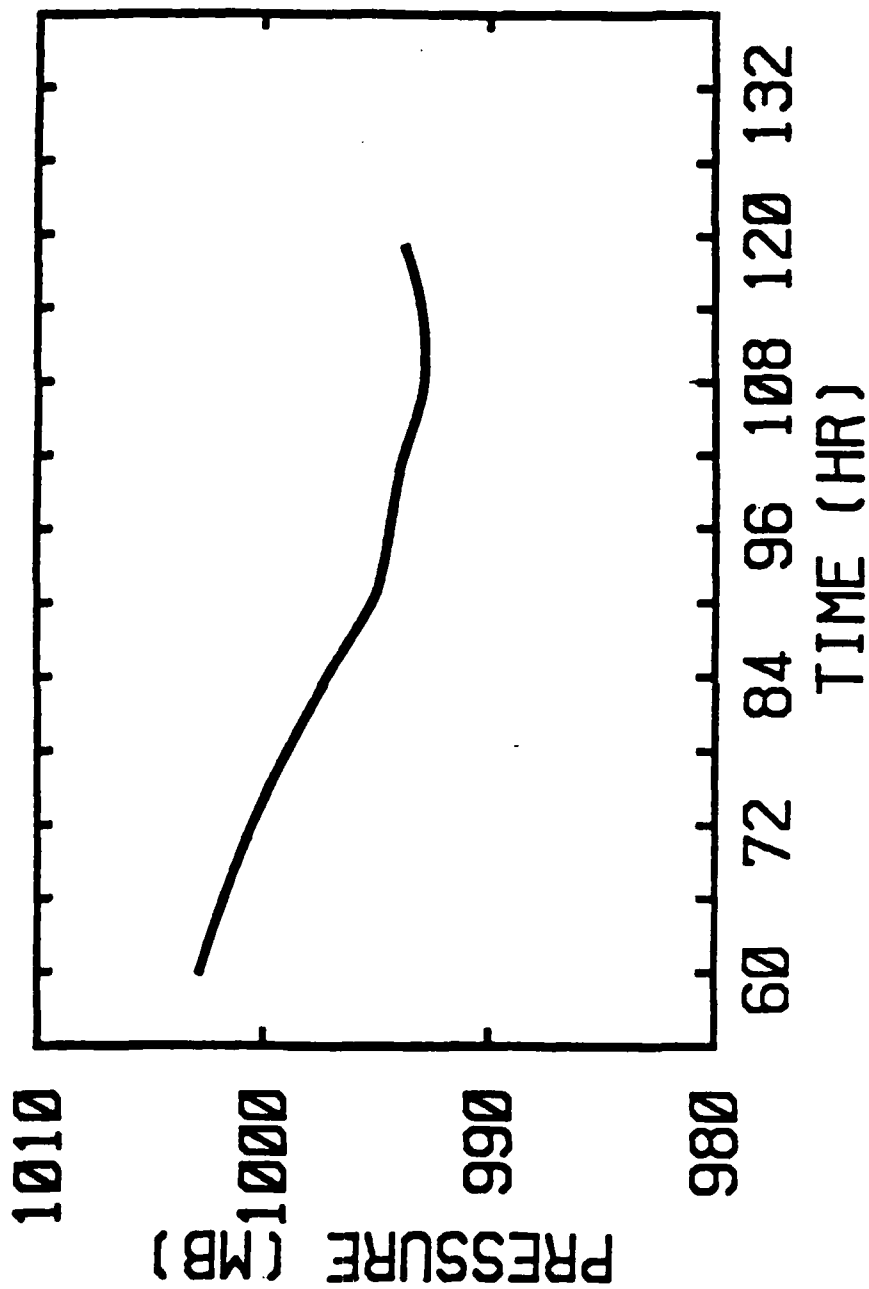
Fig. 4-8.   Minimum central pressure for G20E.

e initial fields. The top of the low level dry adiabatic

yer near the latitude of the polar low rose from near

0 mb initially to near 650 mb by 96 h. The effect of

ese two processes on the energetics of G20D will be

scussed further in the following section.

The effect of the diabatic processes on G20 can be seen

Figs. 4-9 and 4-10, which show the height and temperature

elds at 84 h for 850, 700 and 500 mb for G20A and G20D,

spectively. The amplitude of G20D is stronger at all

vels. In addition, the warmest (coldest) air in G20A

mains just to the east of the trough (ridge) position at

l levels. The amplitude of the thermal ridge is larger

d farther to the east of the trough axis in G20D, espe-

ally at 700 and 500 mb.

The surface sensible and latent heat fluxes for G20D at

h are shown in Fig. 4-11. The maximum for both is about

0 W m^{-2} and is found to the southwest of the low center

hind the cold front. This occurs because this quadrant

hibits relatively low temperatures and the strongest low-

vel winds. Although downward fluxes are typically

served in the warm sector ahead of a low, G20D exhibits a

condary maximum of upward surface fluxes roughly one-half

e maximum values in the cold air. There are two reasons

r the upward fluxes in the warm air. First, the initial

r-sea temperature difference in G20D was at least 5°C in

e vicinity of the developing low, a condition that results

95

END

FILMED

DTIC
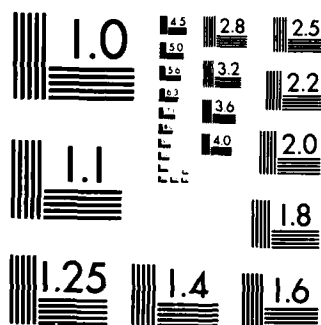
MICROCOPY RESOLUTION TEST CHART
NATIONAL BUREAU OF STANDARDS-1963-A
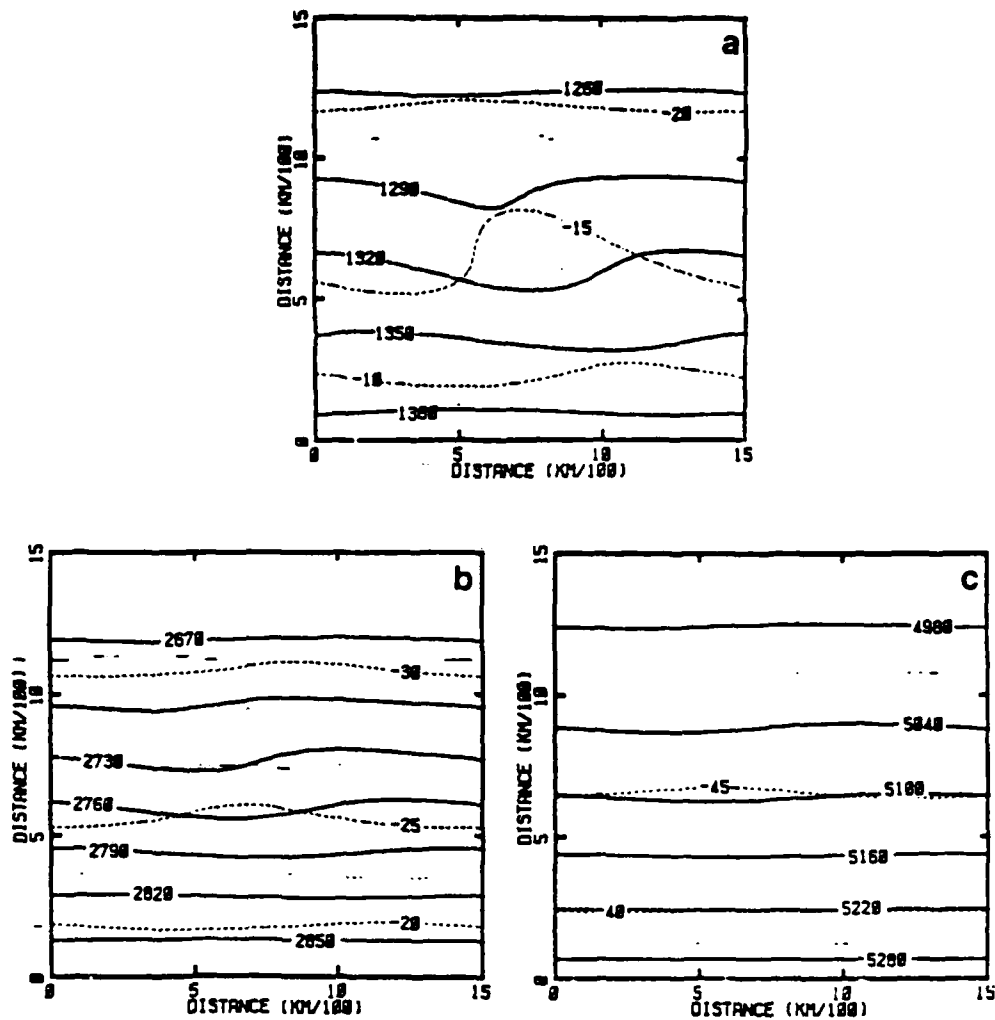
Fig. 4-9.   Fields of height and temperature at (a) 850 mb,
             (b) 700 mb and (c) 500 mb at 84 h for G20A.
             Contour interval for height is 30 m in (a)
             and (b) and 60 m in (c). Contour interval
             for temperature is 5°C. Grid placement as in
             Fig. 4-2.

96
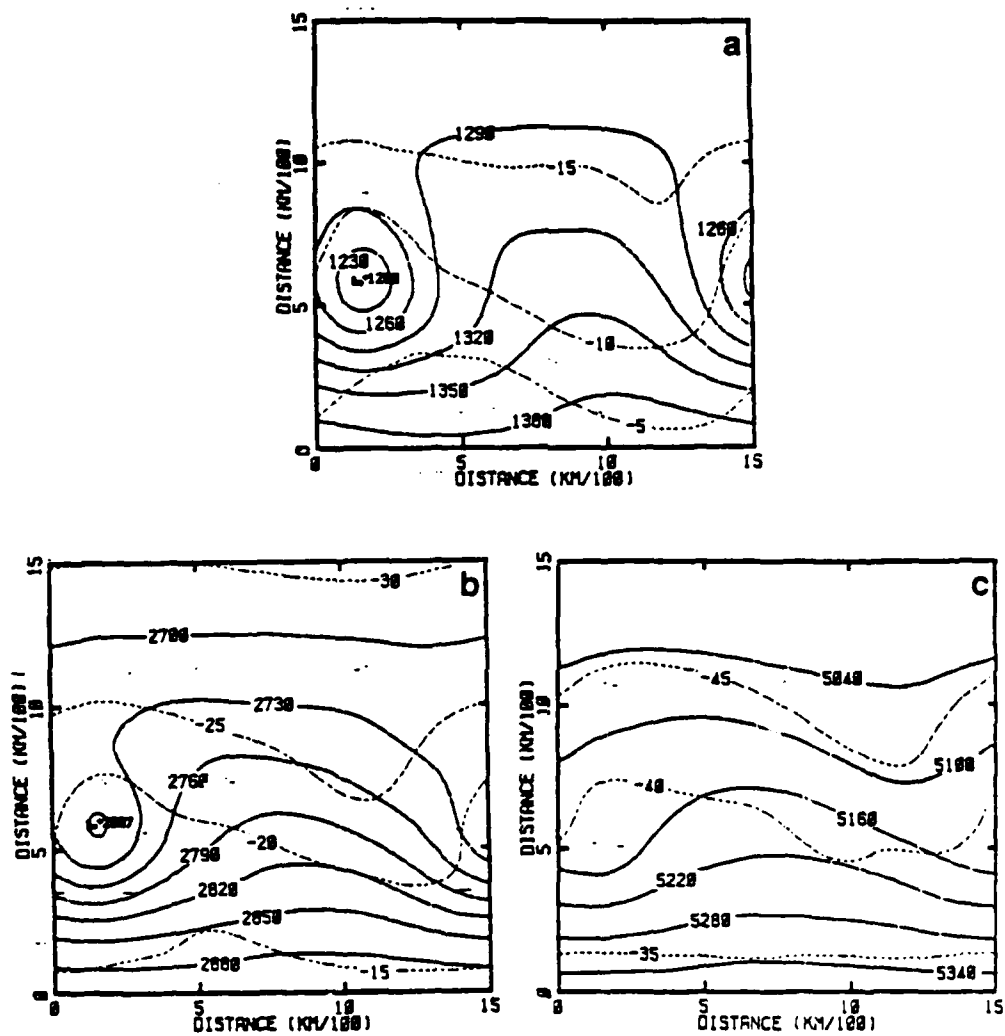
Fig. 4-10. Similar to Fig. 4-9 except for G20D.
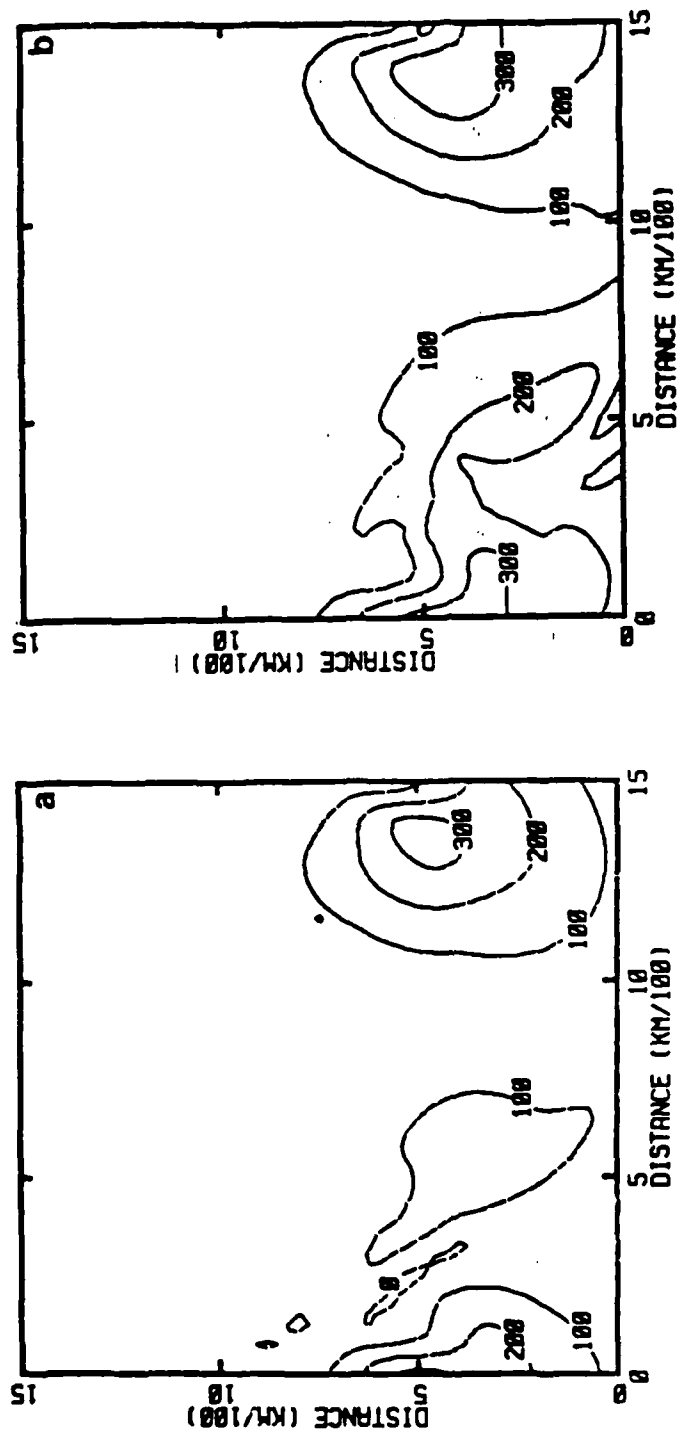
Fig. 4-11. Fields of (a) sensible heat flux and (b) latent heat flux at 84 h for G20D. Contour interval is 100 W m^{-2}. Grid placement as in Fig. 4-2.

in an upward surface heat flux in all quadrants around the low. Second, the low-level horizontal temperature perturbation associated with G20D (Fig. 4-10a) did not become strong enough (at least through 84 h) to reverse the sign of the initial air-sea temperature difference.

B. ENERGETICS

The equations of the energy budgets used in this section are given in Appendix B. However, the terms involving changes in the surface pressure (i.e., PAE, PAZ, PKE, PKZ) are small relative to the other terms, and therefore are not included in this discussion. The budgets are not perfectly balanced due to truncation, interpolation, round-off errors, etc. For the adiabatic runs, the residual is generally an order of magnitude less than the leading term(s), and the residual for the diabatic runs is about 5 times less than the leading term(s).

KE budgets, integrated over the forecast domain, are presented in 6 h intervals in Tables 4-1 and 4-2 for G20A and G20D, respectively. Steady increases of KE are noted in both runs from the beginning of the forecast. The maximum KE attained in G20A (7×10^3 J m^{-2}) is an order of magnitude less than the maximum reached in G20D (8×10^4 J m^{-2}). In addition, the maximum value occurred from 114-132 h for G20A and at 90 h for G20D, which shows the importance of the diabatic processes in increasing both the deepening rate as well as the intensity of the system.

Table 4-1. KE budgets for G20A. KE in units of 10^2 Jm^{-2}. All other budget terms in units of 10^{-1} Wm^{-2}.

Time (hr)	KE	$\partial KE/\partial t$	CE	HCK	VCK	DE
48	2.4	.05	.04	.00	.03	- .03
54	3.5	.07	.07	-.01	.04	- .04
60	5.3	.10	.10	-.01	.06	- .06
66	8.0	.15	.16	-.02	.08	- .10
72	11.7	.21	.23	-.04	.12	- .14
78	17.1	.29	.34	-.07	.18	- .21
84	24.0	.36	.46	-.11	.25	- .31
90	32.8	.44	.65	-.18	.34	- .46
96	42.8	.46	.82	-.27	.44	- .65
102	52.5	.42	.98	-.38	.53	- .87
108	61.0	.33	1.09	-.48	.62	-1.08
114	66.9	.21	1.12	-.55	.69	-1.25
120	69.9	.08	1.06	-.57	.77	-1.34
126	70.3	.00	.93	-.50	.82	-1.36
132	70.1	.08	.86	-.34	.87	-1.34
138	73.9	.29	1.01	-.24	.90	-1.36

Table 4-2. Similar to Table 4-1 except for G20D.

Time (hr)	KE	$\partial KE/\partial t$	CE	HCK	VCK	DE
48	63.7	1.55	1.0	.1	1.5	.3
54	94.1	1.48	1.2	-.5	1.8	-.5
60	127.6	2.13	1.6	-.7	2.7	-1.0
66	186.2	3.34	3.7	-1.6	4.5	-1.5
72	272.0	5.22	4.6	-1.3	5.1	-1.9
78	411.8	8.46	10.8	-1.6	3.8	-3.8
84	637.6	9.15	16.6	-4.4	6.3	-7.2
90	807.2	1.78	15.6	-13.5	12.4	-9.3
96	714.6	-6.45	4.3	-13.0	10.5	-7.8
102	528.4	-7.20	1.5	-6.1	4.9	-5.4
108	394.8	-3.58	1.0	-2.5	4.1	-3.6
114	373.6	-1.25	3.6	-3.6	3.1	-3.9
120	341.0	-.84	5.0	-4.2	2.3	-3.0
126	337.5	1.27	3.7	-1.4	2.2	-2.3
132	396.0	2.55	3.4	-1.4	4.0	-2.9
138	447.8	.26	2.2	-3.5	5.3	-4.1

Time-height cross-sections of KE for G20A and G20D are given in Fig. 4-12. For G20A, the maximum KE occurs at 950 mb and decreases rapidly with height. For G20D, the maximum KE is found at 90 h, also near 950 mb, but a secondary maximum of about 2/3 of the 950 mb value exists near 450 mb. This is a reflection of the increased depth of this system, as noted in the previous section.

During the growth of G20A and G20D, CE is the largest term, which indicates that baroclinic conversion is the principal mechanism in forming the 1400 km wave. The values of CE are more than an order of magnitude larger for G20D than for G20A. Time-height cross-sections of CE are shown in Fig. 4-13. For G20A, CE has a maximum at 120 h near 875 mb with negative values above 700 mb as the storm is developing. This is consistent with the structure of G20A found in the previous section. It was noted that a thermally direct circulation was evident below about 750 mb, which is consistent with the shallow nature of CE in Fig. 4-13. For G20D, CE exhibits a maximum at 84 h near 700 mb that is nearly an order of magnitude larger than the G20A maximum. In addition, positive values of CE extend to nearly 400 mb. It was noted in the previous section that the effect of diabatic heating was to shift the warmest air above 750 mb to the region of the strongest upward motion, thereby enabling the generation of KE, through the term CE, to strengthen the circulation in the middle to upper levels.
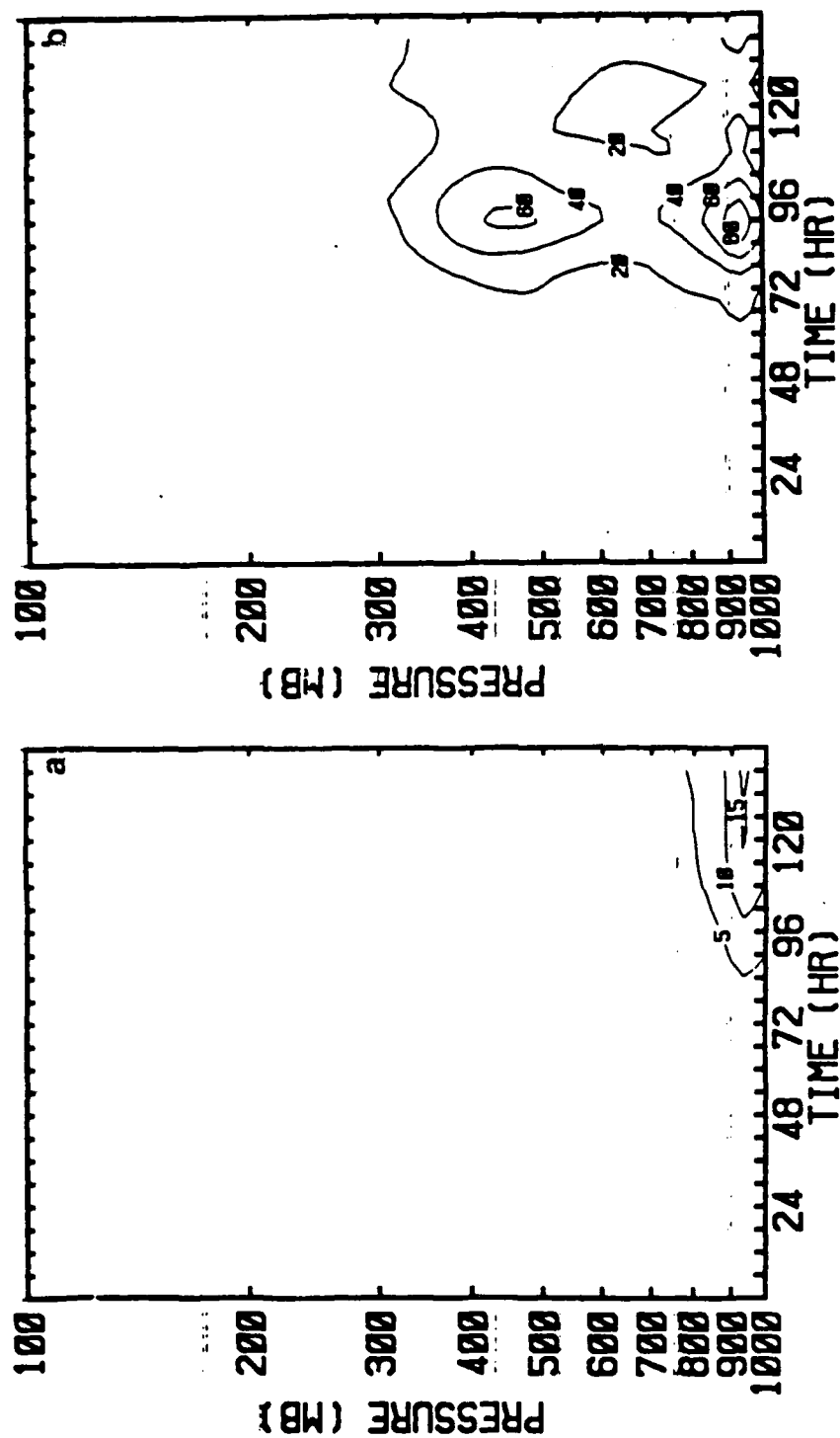
Fig. 4-12. Time-height cross-sections of KE for (a) G20A and (b) G20D. Contour interval is 5 x 102 J m^{-2} in (a) and 20 x 102 J m^{-2} in (b).

Fig. 4-13. Time-height cross-sections of CE for (a) G20A and (b) G20D. Contour interval is 5 x 10-3 W m-2 in (a) and 30 x 10-3 W m-2 in (b). Heavy solid line is zero contour, light solid line is positive contour and dashed line is negative contour.

The horizontal shear, or the barotropic term, HCK, is about one order of magnitude less than CE for both G20A and G20D during the early stages of development. As the wave grows, HCK is negative and increases in magnitude. In G20A, HCK reaches a value of about one-half that of CE at 120 h while in G20D, HCK becomes the largest term at 96 h. Therefore, barotropic effects are important in halting the growth of the polar low, especially when diabatic effects are included. Time-height cross-sections of HCK are given in Fig. 4-14. As with CE, G20A exhibits a maximum of HCK near 900 mb while G20D exhibits a maximum at 850 mb and near 500 mb.

The Kelvin-Helmholtz term, VCK, is positive at all times for both forecasts. It was shown in Chapter III that VCK involves the correlation between u' and ω' multiplied by the vertical wind shear. During the development of the polar low in these experiments, strong positive correlations were observed between u' and ω'. Generally, this implies easterly, upward motion ahead of the trough and westerly, downward motion behind the trough. Coupled with the large vertical wind shear, large, positive values of VCK result. It was shown in the previous section that the sensible heat flux in G20D reduces the stability in the lowest levels, which results in a decrease of R_i, which is consistent with the large values of VCK. However, VCK is ruled out as the term which is responsible for the rapid deepening of the

105
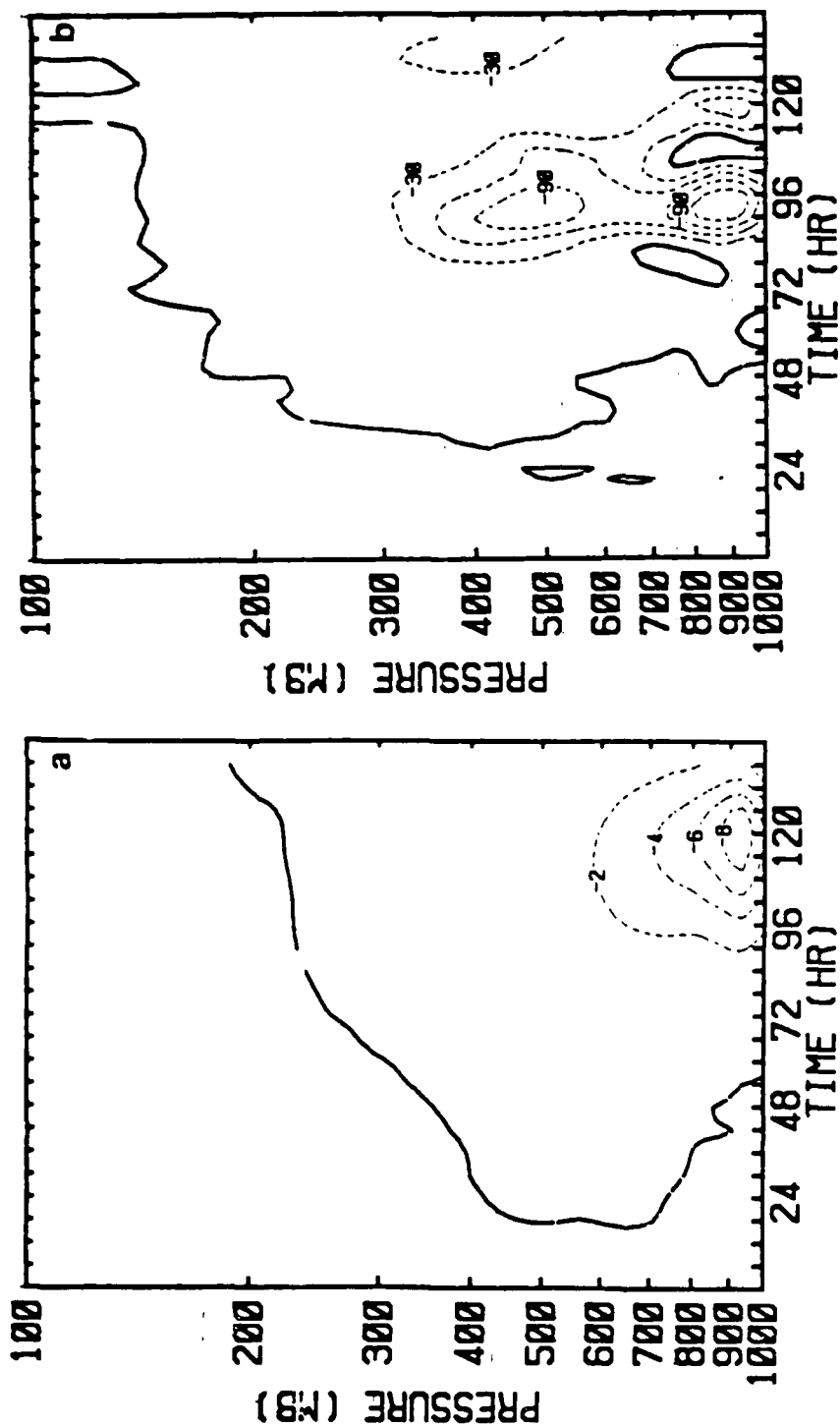
Fig. 4-14. Time-height cross-sections of HCK for (a) G20A and (b) G20D. Contour interval is 2×10^{-3} W m-2 in (a) and 30×10^{-3} W m-2 in (b). Format of contours as in Fig. 4-13.

polar low. In fact, VCK may inhibit polar low formation.

As described in Chapter III, positive values of VCK lead to

helical circulations in the vertical plane which are quite

different from the observed structure of polar lows. The

presence of this helical circulation will tend to decrease

the vertical wind shear (i.e., baroclinity) and result in

a reduced growth rate of the polar low through CE. Also,

during the rapid growth of G20D from 78-90 h, CE is the

dominant term. For example, VCK is three times less than

CE at 78 h. When weaker development was occurring prior

to 78 h, VCK was larger than CE in G20D. In G20A, VCK was

generally a factor of two smaller than CE at all times.

Time-height cross-sections of VCK are shown in Fig. 4-15.

Again, the increased depth of the disturbance is reflected

by a double maximum in VCK at 850 mb and 500 mb in G20D and

only a low-level maximum of VCK near 850 mb for G20A.

The dissipation of KE by friction, DE, is negative at

all times, which indicates a sink of KE. For G20A, DE

slow   ses in magnitude during the forecast so that

at 24 h, DE is one half that of CE. At 114 h, DE is larger

than CE, which shows the strong influence of friction in

damping this disturbance at all times. In fact, DE is the

largest term in the G20A budget from 114-138 h. This is

expected due to the shallow nature of this disturbance.

For G20D, DE plays a reduced, but still significant role.

The results of experiments G20B, G20C and G20D illustrate the type of environment that is favorable for significant polar low development. As the polar low develops, relatively cold air is advected to the west of the storm in the lower levels, while warmer air is advected ahead of the storm. This temperature advection drives the PBL toward more unstable conditions behind the storm and toward more stable conditions ahead of the storm. For an initially neutral PBL (as in G20B), this implies an unstable PBL in the cold air and a stable PBL in the warm air during the growth stage. Therefore, surface fluxes in the warm sector tend to be relatively small. This implies that relatively little or no additional moisture will be added to the system which may be used to sustain additional growth. In addition, surface friction would also be relatively small in the warm sector which implies smaller vertical motion and smaller moisture convergence, and therefore a reduced amount of precipitation. In the unstable PBL behind the surface low, relatively large surface fluxes exist. However, heating in this area will destroy AE. More favorable conditions for development exist for an initially unstable PBL in all quadrants around the developing disturbance (G20D). In this case, large amounts of heat and moisture are added to the near-surface layers, which is a favorable condition for convection. In addition, surface friction is increased,

121
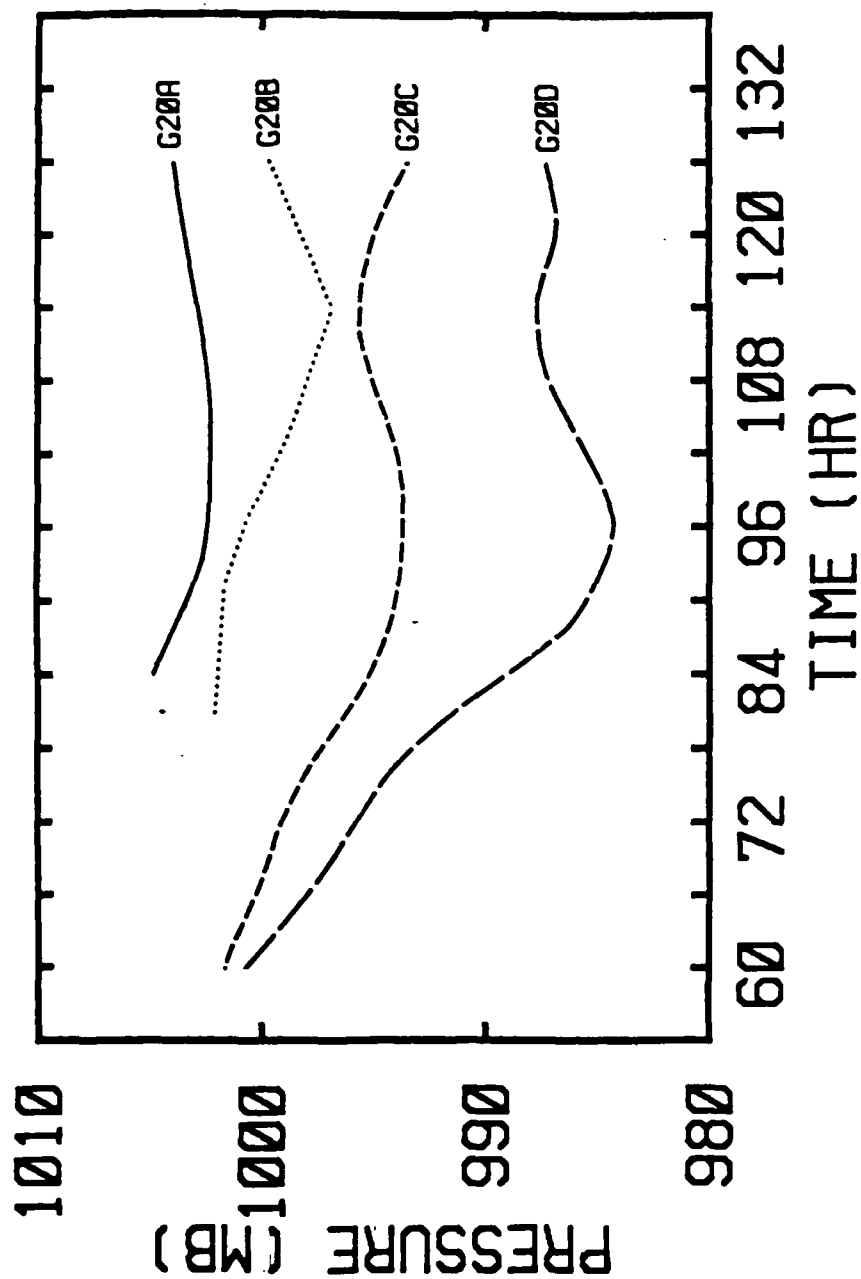
Fig. 4-20. Minimum central pressure for G20A (solid), G20B (dotted), G20C (short dash) and G20D (long dash).

The minimum central pressures versus time for all four G20 simulations are given in Fig. 4-20. The least intense storm was produced by the adiabatic simulation, G20A, which attained a minimum pressure of 1003 mb. Although this forecast did not include diabatic effects explicitly, the initial air-sea temperature difference did play a role in the evolution of the storm since the surface friction is a function of the stability of the PBL (Eqs. A-10 through A-20). Initially, the PBL was unstable due to the large air-sea temperature difference imposed and remained unstable throughout the forecast. This is somewhat unrealistic because the surface heat flux would act to drive the PBL toward a neutral stability. Therefore, G20A was rerun using an initial air-sea temperature difference of zero to determine the effect of PBL stabilization on G20A. Although no difference in storm structure or speed was noted, the minimum central pressure did decrease 2 mb more than in G20A.

The simulation of G20D produces the most intense storm and the storm with the greatest vertical depth. The rapid deepening of the system is crucially tied to the latent heat release. From 72-84 h, when G20C and G20D exhibit the most significant deepening, there is 15-22 mm of precipitation near and ahead of the storm center in G20D. During the same time, G20C has 5-7 mm and G20B has less than 3 mm of precipitation.

119

tends to be too shallow. Inclusion of diabatic processes leads to a significant increase in intensity (i.e., 19 mb lower central pressure) and a deeper, more realistic vertical structure.

C. EFFECT OF AIR-SEA TEMPERATURE DIFFERENCE

In the previous two sections, large differences were observed between the adiabatic and diabatic experiments. The air-sea temperature differences given by Mullen (1979) for the genesis case (cf, Fig. 4-4) were used in the initial fields. The results of two additional simulations of G20 are presented here to illustrate the effect of the air-sea temperature difference. Details of all four G20 simulations are given in Table 4-5. A zero initial air-sea temperature difference is specified in G20B, while in G20C the air-sea temperature difference is one-half of that used in G20D. All diabatic processes used in G20D are also used in G20B and G20C.

Table 4-5. Physical processes and initial air-sea temperature differences for polar low simulations.

Experiment	Friction	Diabatic Processes	Initial Air-Sea Temperature Difference (K)
G20A	Yes	No	Mullen (1979) Genesis Case
G20B	Yes	Yes	0.0
G20C	Yes	Yes	One-half value used in G20A
G20D	Yes	Yes	Same as in G20A

118

The most significant differences between the forecasts is the large increase in VCA near 600 mb in G20D, which again reflects the increased circulation in the middle layers.

The results of these energy budgets illustrate how the diabatic effects lead to an increase in storm intensity. During the rapid intensification of G20D from 73-90 h, the sum of HCA and VCA is 6-10 times larger than GE. This suggests that much more AE is formed by eddy heat transport processes than generated directly by diabatic effects. This is supported by the fact that experiment G20E, which neglected latent heat release by precipitation resulted in a 10 mb decrease in minimum central pressure from the adiabatic simulation. Therefore, it is concluded that diabatic processes in the Pacific polar low primarily serve to alter the overall temperature structure of the disturbance such that eddy heat transport, and therefore, AE values are increased. The rapid storm growth is due to baroclinic conversion of this AE to KE.

The results presented here agree with the speculation of Sardie and Warner (1983) that moist baroclinity is the cause of Pacific polar lows. The linear studies in Chapter III demonstrated that wavenumber 20 exhibits growth rates as large as wavenumber 8 after a period of modification to the genesis jet. Although wavenumber 20 forms in the nonlinear, adiabatic model with friction, the intensity of the polar low is much weaker than observed. Furthermore, the wave

117
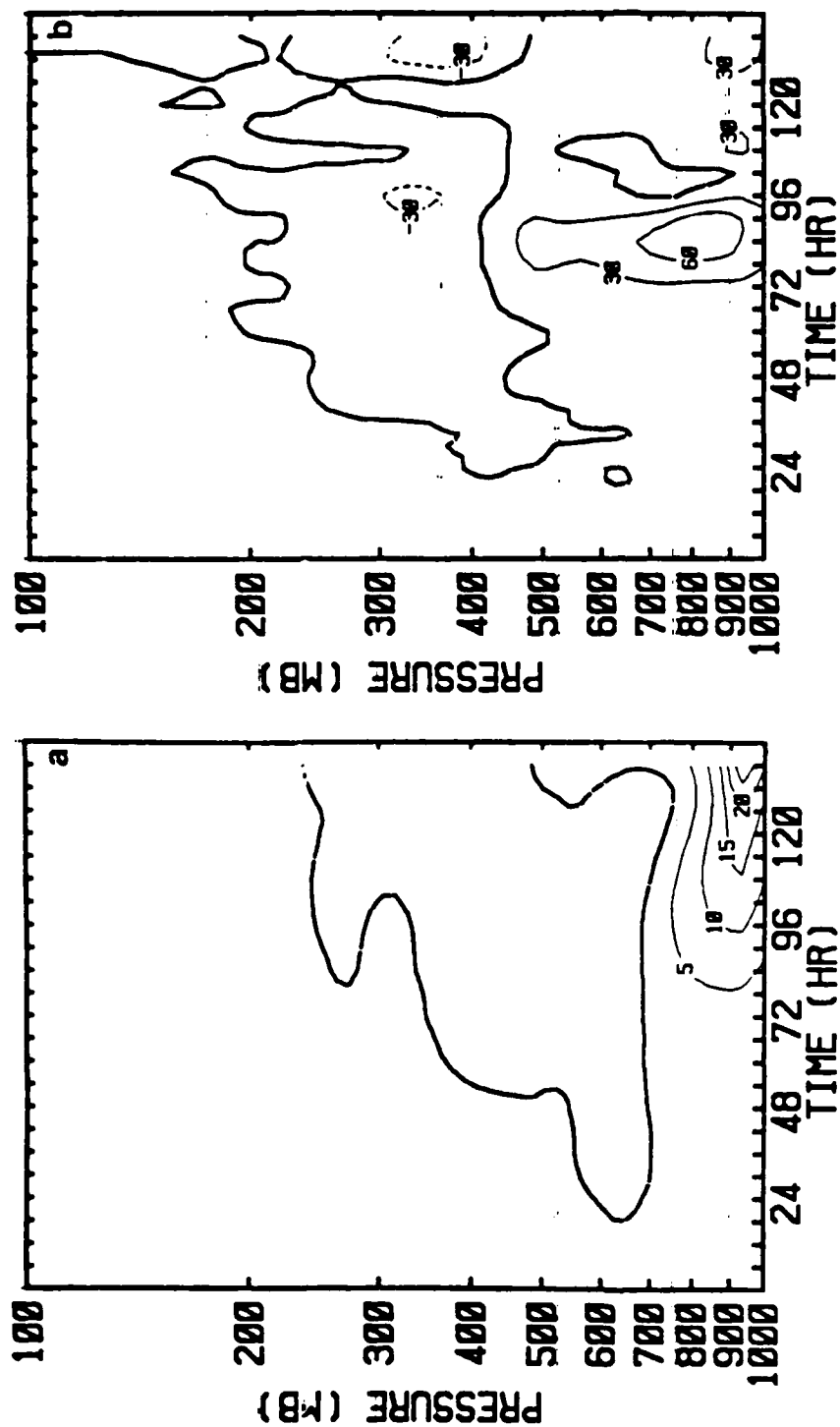
Fig. 4-19. Time-height cross-sections of VCA for (a) G20A and (b) G20D. Contour interval is 5 x 10-3 W m-2 in (a) and 30 x 10-3 W m-2 in (b) Format of contours as in Fig. 4-13.

116
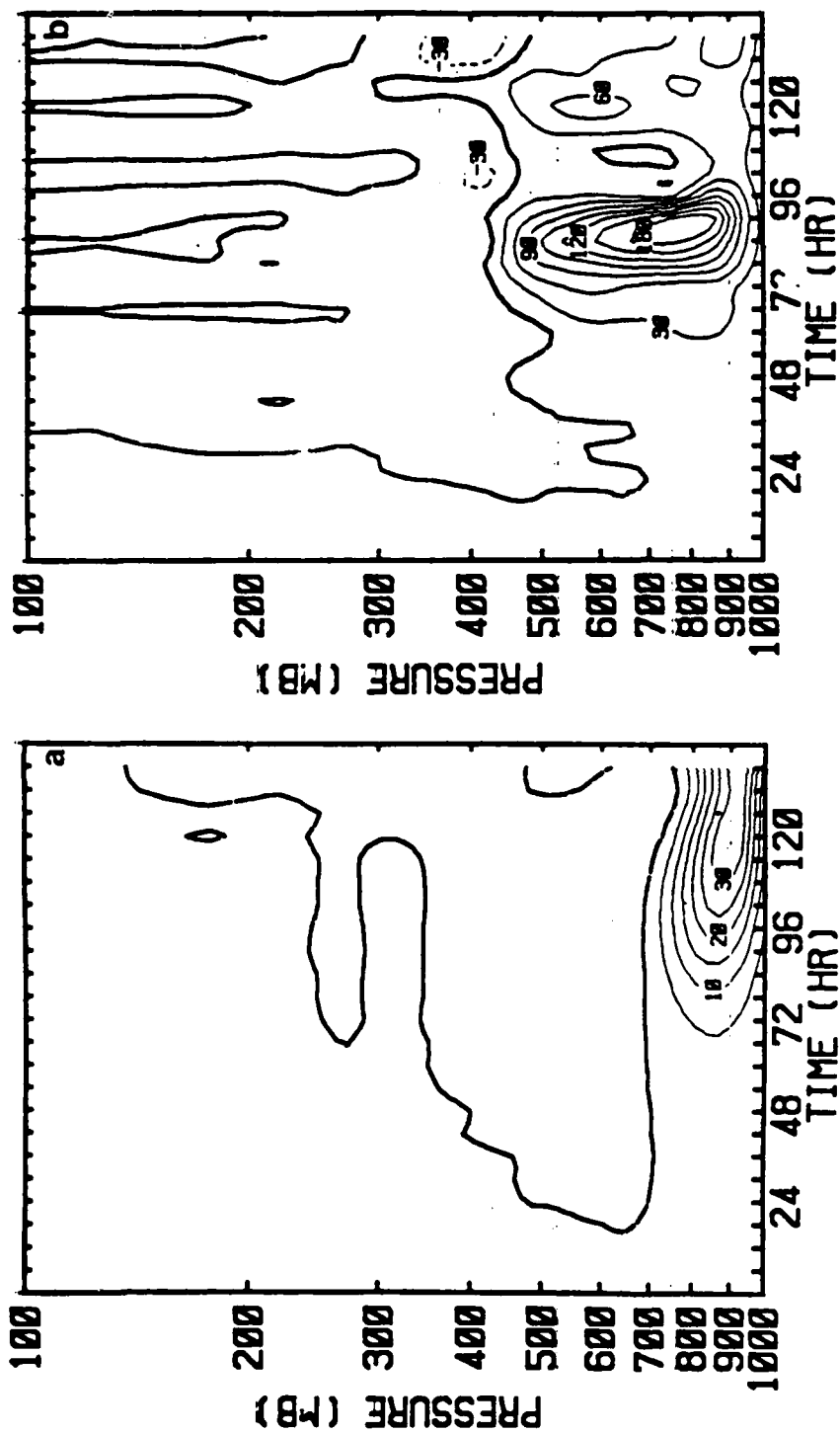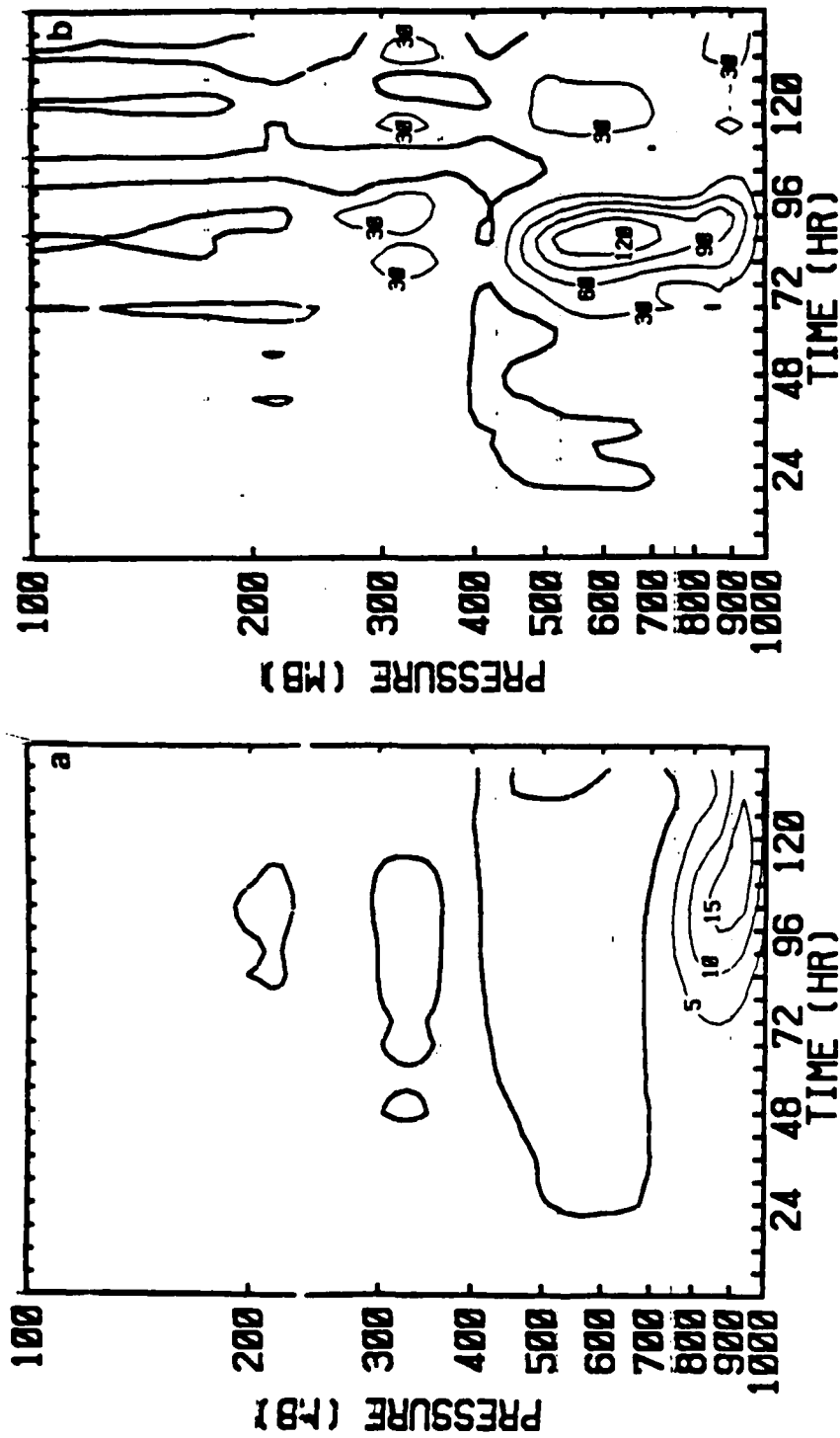
Fig. 4-18. Time-height cross-sections of HCA for (a) G20A and (b) G20D. Contour interval is 5 x 10-3 W m-2 in (a) and 30 x 10-3 W m-2 in (b). Format of contours as in Fig. 4-13.
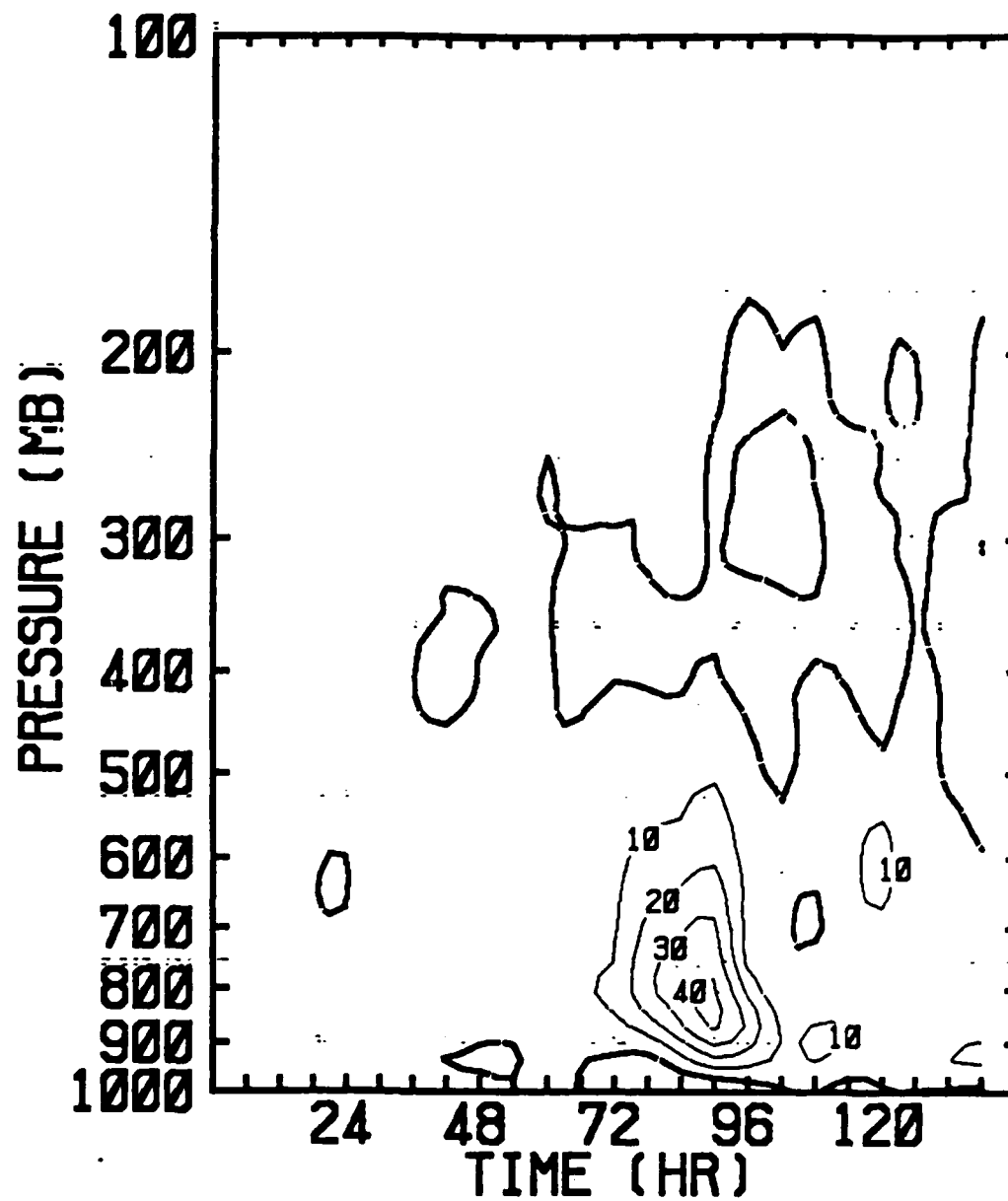
Fig. 4-17. Time-height cross-section of GE for G20D.
Contour interval is 10 x 10-3 W m-2. Format
of contours as in Fig. 4-13.

114

GE for G20D is shown in Fig. 4-17. Maximum values of GE are found near 800 mb with positive values extending from near 950 mb to 400 mb. Small negative values are observed near the surface due to the largest surface fluxes occurring in the cold air behind the low (Fig. 4-11).

The horizontal eddy heat transport term, HCA, is positive during the development of G20A and G20D, which indicates a generation of AE. Maximum values of HCA for G20A are found near 950 mb with smaller, negative values above 700 mb (Fig. 4-18). For the diabatic run, HCA is larger in magnitude and the positive values extend up to 450 mb. This illustrates that the diabatic processes have resulted in an increased circulation above 750 mb such that *horizontal eddy heat transport can generate significant AE at these levels.* This is expected due to the height and temperature patterns exhibited by G20A and G20D (Figs. 4-9 and 4-10).

The vertical component of CA, VCA, is also positive during the development of the polar low in both experiments. Again, G20D exhibits values over one order of magnitude larger than G20A. Although the term containing $\overline{E'\omega'}\bar{\alpha}$ favors destruction of AE, the terms containing $\overline{\omega'E'}\,\partial\bar{T}/\partial p$ and $\overline{\omega'T'}\,\partial\bar{E}/\partial p$ are positive and larger in magnitude, and result in an overall gain in AE through VCA. Time-height cross-sections of VCA for G20A and G20D are given in Fig. 4-19.
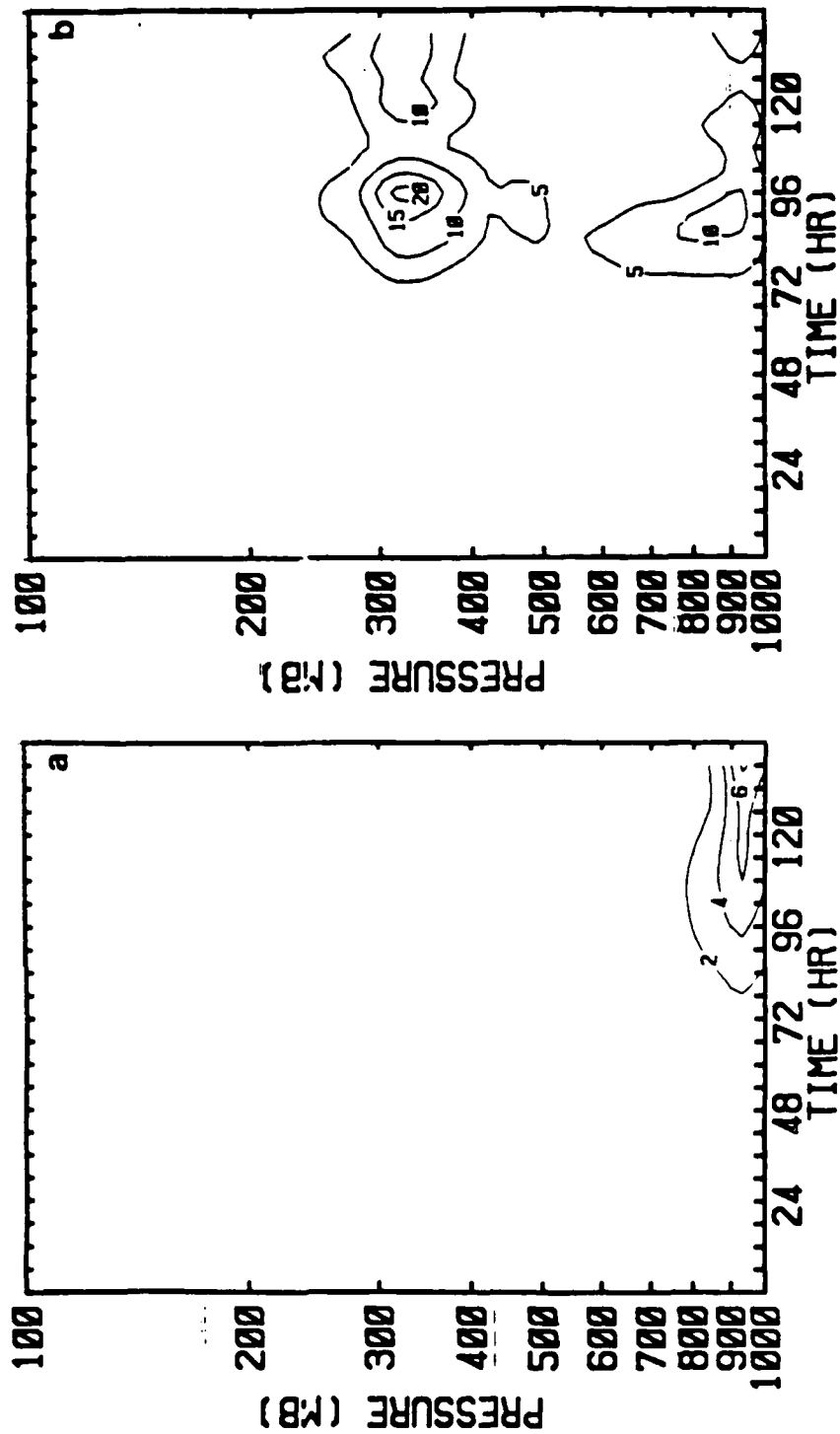
Fig. 4-16. Time-height cross-sections of AE for (a) G20A and (b) G20D. Contour interval is 2 x 10² J m-2 in (a) and 5 x 10² J m-2 in (b).

112

Table 4.4. Similar to Table 4-3 except for G20D.

Time (hr)	AE	$\partial AE/\partial t$	CE	GE	HCA	VCA
48	9.9	.21	1.00	.14	.37	1.05
54	14.5	.25	1.07	.14	.36	1.03
60	20.6	.33	1.60	.21	.67	1.55
66	28.9	.72	3.71	.52	1.20	3.21
72	51.6	1.42	4.56	.66	2.34	4.36
78	90.3	1.75	10.80	1.38	4.67	9.15
84	127.2	.96	16.60	1.88	6.59	11.79
90	132.0	-.17	15.60	2.44	5.20	10.38
96	120.0	-1.19	4.25	.93	.41	3.33
102	80.3	-1.24	1.51	.24	-.24	.50
108	66.3	-.03	.95	.49	1.07	1.11
114	78.8	.26	3.64	.58	.98	4.35
120	77.7	-.48	5.03	.51	1.43	3.44
126	58.2	-.19	3.70	.42	1.57	2.56
132	61.4	.49	3.40	.29	1.15	3.67
138	79.2	.25	2.23	.18	1.04	2.57

Table 4-3. AE budgets for G20A. AE in units of 10^2 Jm^{-2}. All other budget terms in units of 10^{-1} Wm^{-2}.

Time (hr)	AE	$\partial AE/\partial t$	CE	HCA	VCA
48	1.3	.03	.04	.03	.04
54	1.9	.04	.07	.05	.06
60	2.9	.05	.10	.08	.09
66	4.2	.08	.15	.11	.13
72	6.1	.10	.23	.16	.19
78	8.7	.14	.34	.23	.27
84	12.0	.17	.46	.31	.36
90	15.9	.19	.65	.41	.49
96	20.0	.18	.82	.50	.58
102	23.7	.14	.98	.57	.65
108	26.1	.06	1.09	.61	.67
114	26.5	-.02	1.12	.61	.60
120	25.2	-.05	1.06	.60	.52
126	24.2	.01	.93	.63	.43
132	25.8	.14	.86	.75	.40
138	30.3	.26	1.01	.95	.47

Although DE attains a maximum at 90 h in G20D when KE is a maximum, DE is still 30% smaller than H⁢. Therefore, when diabatic processes are included, barotropic damping is dominant in halting wave growth. This is due to the increased depth of G20D. Frictional effects are relatively small in G20D since they are felt only in the lowest levels of the model. However, it was shown earlier (Fig. 4-14) that HCK exhibits large values near 850 mb and near 500 mb and is, therefore, more efficient in reducing overall wave growth.

AE budgets, integrated over the forecast domain, are presented in 6 h intervals in Tables 4-3 and 4-4 for G20A and G20D, respectively. G20D exhibits more AE than G20A at all times. The maximum AE for G20A (2.6×10^3 J m^{-2}) is found at 114 h, and the maximum AE for G20D (1.3×10^4 J m^{-2}) is found at 90 h. Therefore, as evidenced with KE, AE develops faster and reaches larger values with the inclusion of diabatic processes. Time-height cross-sections of AE are given in Fig. 4-16. The major difference between the forecasts is that G20D exhibits a strong maximum of AE near 300 mb. This feature is absent in the G20A forecast.

The generation of AE by diabatic processes, GE, is positive at all times in G20D as a result of the precipitation found in advance of the storm center (cf, Fig. 4-8). The largest values of GE occur from 78-90 h during the rapid intensification of G20D. The time-height cross-section of

109
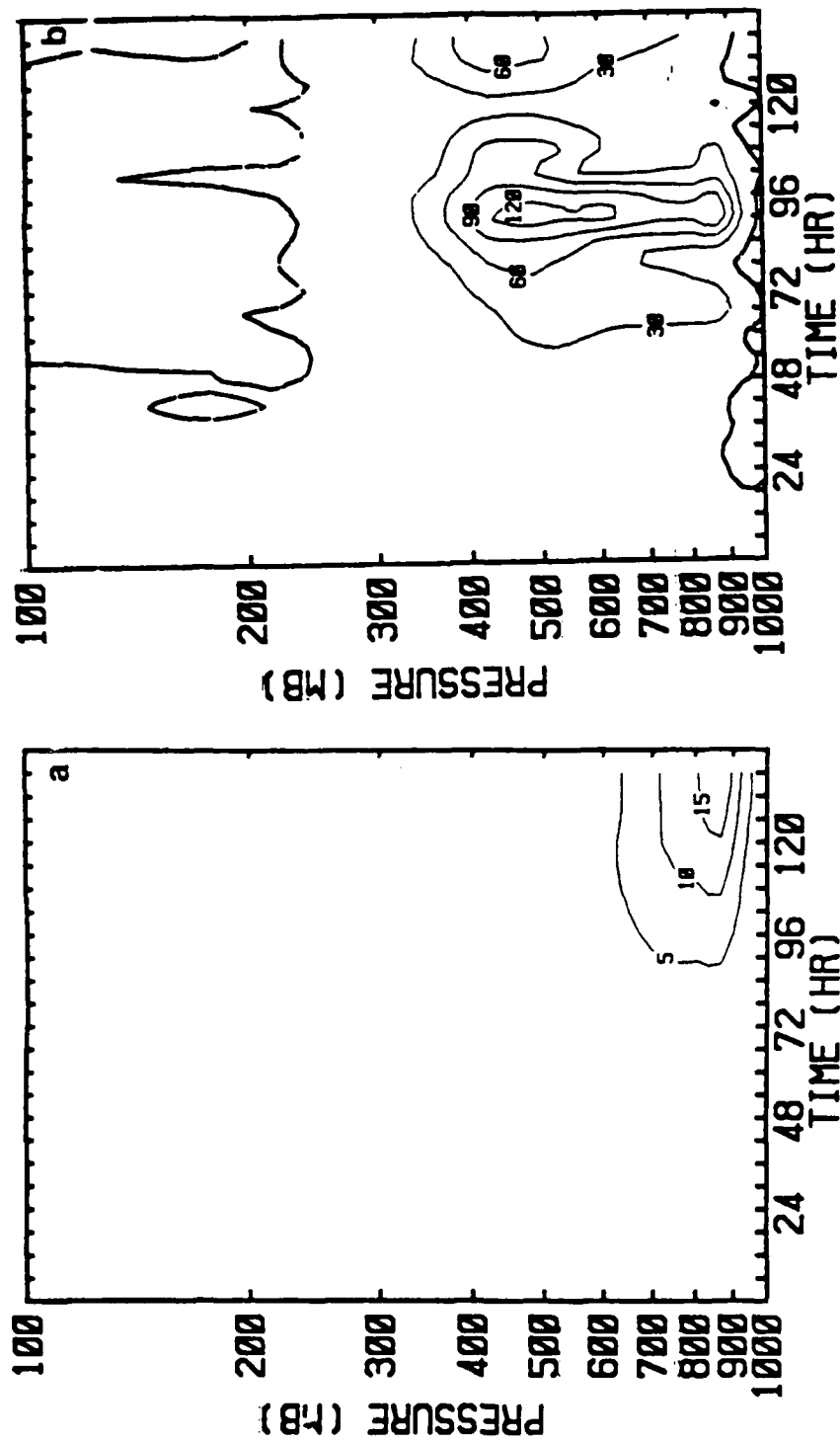
Fig. 4-15. Time-height cross-sections of VCK for (a) G20A and (b) G20D. Contour interval is 5 x 10-3 W m-2 in (a) and 30 x 10-3 W m-2 in (b). Format of contours as in Fig. 4-13.

which suggests stronger vertical motion and therefore, an increase in precipitation. Although AE is still destroyed in the cold air behind the low, this is small in comparison to the generation of AE in the warm sector.

V. CONCLUSIONS

The purpose of this study is to determine the reasons for the growth and maintenance of Pacific polar lows. In particular, the major hypothesis to be tested is that the Pacific polar low forms through baroclinic instability. To accomplish this, a 3-dimensional, primitive equation model, including convective and planetary boundary layer parameterizations is used with two sets of initial data. The first set is a jet profile typical of mean winter conditions and the second is a jet profile typical of conditions present during the genesis period of Pacific polar lows (Mullen, 1979). A linearized version of the model is used for adiabatic and diabatic simulations of the Pacific polar low.

The linear studies indicate that medium-scale (wavenumber 12) waves are most unstable for mean winter conditions. However, wave-zonal flow interaction and surface friction are found to preferentially damp the shortest waves and thereby shift the most unstable mode to wavenumber 9. Energy budgets verify that this wave forms through baroclinic instability. These results are similar to those found by Gall (1976a), who computed the growth rate spectrum for wavenumbers less than 15 for mean winter conditions. Although this study includes wavenumbers 15-30, growth rates of these waves were found to be much less than for the longer waves.

The genesis jet exhibits a peak in the growth rate spectrum at wavenumber 3, which also grows primarily through baroclinic instability. However, the largest growth rate is found at wavenumber 40. This disturbance is confined to the lowest 300 mb of the troposphere and exhibits a helical circulation. An energy budget verifies that this wave grows through baroclinic instability and Kelvin-Helmholtz (vertical shear) instability. Stone (1966) and Orlanski (1968) showed that Kelvin-Helmholtz instability can be significant for Richardson numbers less than 1, a condition initially satisfied near the surface in the genesis jet case.

Wavenumber 40 is found to be sensitive to the initial conditions and physical processes. This wave exhibits a relatively short period of linear growth, approximately one day, as opposed to several days for longer waves. It is suggested that this is due to the stabilization of the flow, relative to wavenumber 40, by either wavenumber 40 or a combination of waves. For this reason, a modified genesis jet is created by allowing perturbations to interact with the zonal flow for 84 h, and then computing the new zonal flow by averaging all 84 h forecast fields over latitudinal circles. In this modified genesis jet, the Richardson number in the low-levels near the jet axis ranges from 2-5 and the growth rate of wavenumber 40 is 0.82 day^{-1}. This is in contrast to the original genesis jet which exhibits

Richardson numbers less than 1 in the low-levels underneath
the jet axis and a growth rate for wavenumber 40 of 1.82
day^{-1}. In addition, surface friction is found to result in
a further reduction in the growth rate of wavenumber 40.
However, nonlinear simulations of a longer wave (wavenumber
20) indicates the presence of Kelvin-Helmholtz instability
by the formation of bands similar to that found in wave-
number 40 in the linear experiments. These bands are
located along the front and are correlated with Richardson
numbers less than 1 in the low levels. These low Richardson
numbers are a result of a large surface sensible heat flux
forcing near-dry adiabatic lapse rates in the near-surface
layers. This suggests that although wave-zonal flow inter-
action and surface friction act to damp severely the growth
of the baroclinic/Kelvin-Helmholtz wave, physical processes
can create favorable conditions for its existence.

Growth rates for the modified genesis jet are signifi-
cantly different from the original genesis jet with one
growth rate maximum at wavenumber 8 and another of equal
size at wavenumber 20. The latter disturbance resembles the
Pacific polar low described by Reed (1979) and Mullen (1979)
in that it forms about 1000 km north of the jet axis with a
wavelength of 1400 km. However, wavenumber 20 has maximum
amplitude at the surface and extends only through about the
lowest 300 mb of the troposphere. This is inconsistent with
observed mature Pacific polar lows which can exhibit height

perturbations at 300 mb as large as at the surface (Reed, 1979). Energy budgets verify that wavenumber 20 forms through baroclinic instability. The magnitude of the growth rates found in this study for wavenumbers 20 and 40 demonstrate that systems with horizontal scales of the Pacific polar low (and smaller) are unstable without the inclusion of diabatic processes.

The results of these linear studies using the genesis jet differ from those of Sardie and Warner (1983) (hereafter SW), who showed that the maximum growth rate for the genesis jet is 1.29 day^{-1} at wavenumber 10. SW found no evidence of the larger growth rates for shorter wavelengths as found in this study. Two reasons are cited for this. First, SW used a quasi-geostrophic model which neglects the non-geostrophic term ($\overline{u' \omega'}\, \partial \bar{u}/\partial p$) that was found to be significant in the development of wavenumber 40. Second, the model used by SW contained only three layers, with the lowest layer being 200 mb thick, whereas the model used here contains three layers within the lowest 200 mb. In this study, for linear, adiabatic, inviscid conditions, wavenumbers 20 and 40 are confined to the lowest 250 mb, which suggests that the vertical resolution used by SW is insufficient to define these features.

Adiabatic and diabatic nonlinear simulations are performed for wavenumber 20 of the modified genesis jet. Although the adiabatic system intensifies, it remains a

126

shallow disturbance as in the linear experiments and the deepening rate is much smaller than typically observed for Pacific polar lows. The inclusion of diabatic effects dramatically increases both the disturbance depth and deepening rate. This is accomplished by enhancing the temperature perturbation within the disturbance such that large amounts of AE are generated by eddy heat transport. The temperature perturbation is increased in two ways. The first is through latent heat release, primarily by convection, in the warm sector of the storm. Second, large initial air-sea temperature differences result in a strong surface heat flux which acts to maintain the low-level horizontal temperature gradient. In addition, the sensible heat added within the PBL is rapidly mixed to mid-levels through dry convective adjustment. Rapid intensification results from the baroclinic conversion of this AE to KE. The amount of AE directly generated by latent heat release in the warm sector, where eddy efficiency factors are positive, is about an order of magnitude less than that produced by eddy heat transport. Overall, the inclusion of diabatic effects increased the kinetic energy of the polar low by over an order of magnitude.

Significant KE is generated in the diabatic simulation of the polar low by Kelvin-Helmholtz instability. Maximum values of this instability are found in the trough associated with the polar low. While this instability does not

127

appear to be significant to the overall development of the polar low, it may be significant in the formation of meso-scale features near the front as suggested by Bennetts and Hoskins (1979) and observed by Locatelli et al. (1982).

The simulated polar low, with diabatic effects included, is found to resemble a simulated synoptic-scale extra-tropical cyclone (wavenumber 8), as observed by Locatelli et al. (1982). Similarities exist in patterns of wind, tempera-ture, precipitation and surface pressure. The effects of diabatic processes on wavenumber 8 is found to be similar to that for the polar low.

The results of this study confirm the major hypothesis that the Pacific polar low is a baroclinic disturbance. However, diabatic effects, specifically latent heat release in the warm sector, and the presence of an initial air-sea temperature difference of at least 5 K, are necessary for the polar low to achieve observed deepening rates. This is consistent with the speculation of Sardie and Warner (1983) that moist baroclinity is responsible for the growth of the Pacific polar low.

Research should be continued to further our under-standing and prediction capabilities of the polar low. Specifically, our understanding of convective and planetary boundary layer physics must continue to improve since they are so crucial to the development of the polar low. This can be accomplished through observational studies. More

studies are needed to determine the precise role of Kelvin-Helmholtz instability near the cold front and its possible role in the formation of rainbands. Also, this study does not address either the Atlantic polar low or the continental polar low. Studies similar to this one, using the appropriate initial conditions, are necessary to obtain a better understanding of these systems.

APPENDIX A: THE FORECAST MODEL

A. DYNAMICS

The forecast model uses the primitive equations in the σ coordinate system after Phillips (1957),

$$\sigma = \frac{p}{\pi} \tag{A-1}$$

where $0 \leq \sigma \leq 1$. The equations are:

$$\frac{\partial(\pi u)}{\partial t} = -\frac{\partial(\pi u u)}{\partial x} - \frac{(\pi u v)}{\partial y} - \frac{\partial(\pi u \dot{\sigma})}{\partial \sigma} + f\pi v - RT\frac{\partial \pi}{\partial x}$$

$$- \pi\frac{\partial \phi}{\partial x} + \pi F_u + \pi K_H \nabla^2_\sigma (\nabla^2_\sigma u) \tag{A-2}$$

$$\frac{\partial(\pi v)}{\partial t} = -\frac{\partial(\pi u v)}{\partial x} - \frac{\partial(\pi v v)}{\partial y} - \frac{\partial(\pi v \dot{\sigma})}{\partial \sigma} - f\pi u - RT\frac{\partial \pi}{\partial y}$$

$$- \pi\frac{\partial \phi}{\partial y} + \pi F_v + \pi K_H \nabla^2_\sigma (\nabla^2_\sigma v) \tag{A-3}$$

$$\frac{\partial(\pi T)}{\partial t} = -\frac{\partial(\pi u T)}{\partial x} - \frac{\partial(\pi v T)}{\partial y} - \frac{\partial(\pi \dot{\sigma} T)}{\partial \sigma} - \frac{RT\pi\dot{\sigma}}{\sigma C_p} - \frac{RT}{C_p}(\mathbb{V}\cdot\nabla\pi)$$

$$+ \frac{RT}{C_p}\int_0^1 \nabla\cdot\pi\mathbb{V}d\sigma + \pi K_H \nabla^2_\sigma[\nabla^2_\sigma(T-T_{std})] + \frac{\pi Q}{C_p} \tag{A-4}$$

$$\frac{\partial(\pi q)}{\partial t} = -\frac{\partial(\pi u q)}{\partial x} - \frac{\partial(\pi v q)}{\partial y} - \frac{\partial(\pi \dot{\sigma} q)}{\partial \sigma} + \pi Q_m$$

$$+ \pi K_H \nabla^2[\nabla^2(q - q^*_{std})] \tag{A-5}$$

$$\frac{\partial \pi}{\partial t} = - \int_0^1 \nabla_\sigma \cdot (\pi \mathbf{V}) d\sigma \qquad \text{(A-6)}$$

$$\frac{\partial \phi}{\partial \ln \sigma} = - RT \qquad \text{(A-7)}$$

$$\frac{\partial (\pi \dot{\sigma})}{\partial \sigma} = \int_0^1 \nabla_\sigma \cdot (\pi \mathbf{V}) d\sigma - \nabla \sigma \cdot (\pi \mathbf{V}) \qquad \text{(A-8)}$$

The vertical structure of the grid is shown in Fig. A-1. All variables are defined at the middle of each layer, except $\pi \dot{\sigma}$, which is carried at the interface between the layers. The sigma levels are defined in Table A-1.

Table A-1. Model levels.

Level Number	σ
1	.05
2	.15
3	.24
4	.32
5	.40
6	.48
7	.57
8	.67
9	.76
10	.84
11	.92
12	.98

The horizontal structure of the grid is shown in Fig. A-2. This is defined as scheme C by Arakawa and Lamb (1977). Here, the u-component is defined one-half grid interval in the x-direction from the mass points and

$\sigma=0$ ——————— $\pi\dot{\sigma}=0$

— — — — — — u, v, T, q, ϕ

——————— $\pi\dot{\sigma}$

— — — — — — u, v, T, q, ϕ

——————— $\pi\dot{\sigma}$

⋮

——————— $\pi\dot{\sigma}$

— — — — — — u, v, T, q, ϕ

——————— $\pi\dot{\sigma}$

— — — — — — u, v, T, q, ϕ

$\sigma=1$ ///////////// $\pi\dot{\sigma}=0$
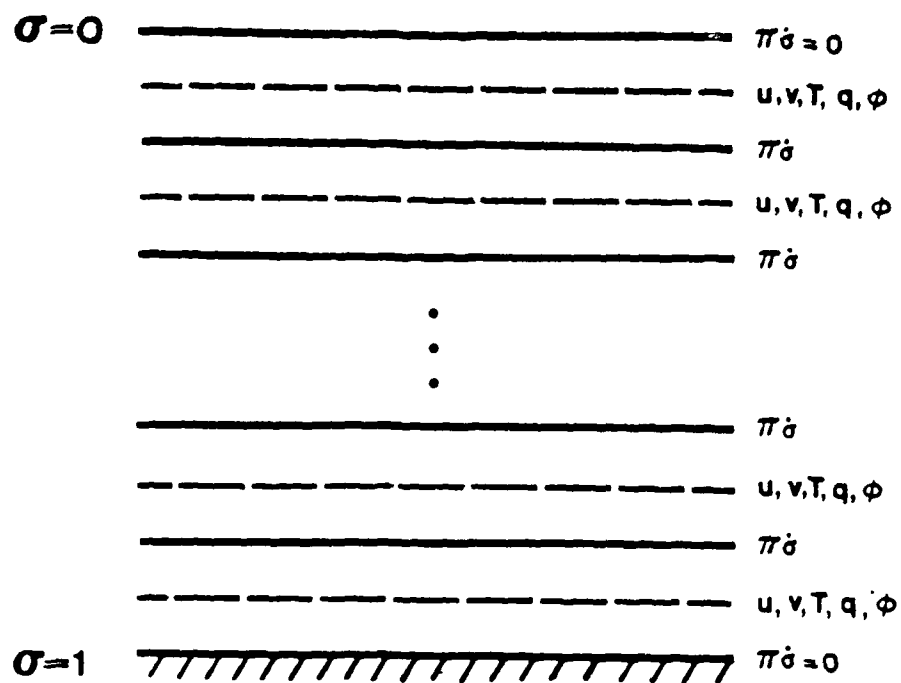
Fig. A-1.   Vertical structure of model grid with distribution of forecast variables.

$$\pi \quad u \quad \pi \quad u \quad \pi$$

$$v \qquad\;\; v \qquad\;\; v$$

$$\pi \quad u \quad \pi \quad u \quad \pi$$

$$v \qquad\;\; v \qquad\;\; v$$

$$\pi \quad u \quad \pi \quad u \quad \pi$$

Fig. A-2.   Horizontal distribution of mass and momentum
points on the forecast grid.

133

the v-component is defined one-half grid interval in the y-direction from the mass points. The grid is periodic in x and has free-slip walls on the y boundaries.

The model uses the split-explicit time integration scheme developed by Madala (1981). First, the equations are integrated over a time step governed by the meteorological and slowest gravity modes. The solution is then adjusted for the linear terms which govern the fastest gravity modes. The momentum and thermodynamic equations are solved with centered time and space differencing, while the moisture equation differencing is forward in time and upstream in space. Fourth order advection is used for the momentum and temperature. Second order advection is used for the moisture.

Fourth order diffusion is used in all the prognostic equations except for π. Second order diffusion is used on the first interior row. This diffusion is done on the sigma levels, which can lead to spurious sources and sinks of energy when applied to the mass and moisture fields. To overcome this problem, the diffusion is applied to deviations from the standard atmosphere for the temperature and moisture. The diffusion coefficient is computed as:

$$K_H = \begin{cases} 5\Delta x/3 & \text{on 1st interior row} \\ 1.6\ \Delta x & \text{on 2nd-4th interior rows} \\ 1.25\Delta x & \text{on all other interior points} \end{cases} \quad \text{(A-9)}$$

134

where Δx is the grid spacing in meters. High frequency time oscillations are controlled by applying the Robert (1966) time filter with the smoothing coefficient set to 0.15.

B. PHYSICS

  1. Planetary Boundary Layer

The surface fluxes are calculated in the manner described by Deardorff (1972). First, the stability of the PBL is calculated using the bulk Richadson number,

$$Ri_B = gh\frac{(\theta v_m - \theta v_s)}{u_m^2} \qquad\qquad (A-10)$$

where θ_v is the vertical potential temperature, subscript s denotes surface values and subscript m denotes mean PBL values. For stable or neutral conditions ($Ri_B \geq 0$), the friction coefficient is

$$C_u = C_{un} \quad (1 - \frac{Ri_B}{Ri_C}), \qquad\qquad (A-11)$$

and the heat transfer coefficient is

$$C_\theta = C_{\theta n} (1 - \frac{Ri_B}{Ri_C}) \qquad\qquad (A-12)$$

where the neutral values are

$$C_{un} = [\frac{1}{k} \ln (\frac{0.025h}{Z_o}) + 8.4]^{-1} \qquad\qquad (A-13)$$

135

APPENDIX C: NONLINEAR SIMULATIONS OF WAVENUMBER 8

The purpose of this appendix is to show the results of
nonlinear, adiabatic and diabatic simulations of wavenumber
8 for the genesis jet to be compared to the results for
similar simulations of wavenumber 20 presented in Chapter
IV.   The minimum central pressures for the adiabatic (G8A)
and diabatic (G8D) experiments are given in Fig. C-1.   The
central pressure in G8A falls from 1003 mb at 72 h to 968 mb
at 120 h with rising pressure afterwards.   In G8D, the
central pressure falls from 999 mb at 72 h to 944 mb at
138 h.   The deepening rate is similar for both systems from
72-108 h.   However, after this time, G8D exhibits a rapid
decrease in central pressure while the central pressure in
G8A starts to rise slowly.   The reasons for this pressure
tendency will now be examined.

The sea-level pressure fields for 60, 84, 108 and 132 h
for G8A and G8D are shown in Figs. C-2 and C-3, respective-
ly. At 60 h, both forecasts exhibit an open trough pattern
with the pressure 2-3 mb lower in G8D.   In addition, the
trough extends further to the southeast in G8D with the
formation of a second center in this trough.   The extension
of this trough is due to convection in the warm sector of
the disturbance.   By 84 h, G8A has attained a closed circu-
lation with a central pressure of 996 mb, whereas G8D has

149

of mass; DE (DZ) is the dissipation of KE (KZ) by surface
friction; GE (GZ) is the generation of AE (AZ) by diabatic
processes; PAE (PAZ) is the change in AE (AZ) due to changes
in the surface pressure and PKE (PKZ) is the change in KE
due to changes in the surface pressure.

$$DZ = -\frac{1}{g} \int_0^\pi [\vec{V} \cdot \vec{F}] dp \tag{B-20}$$

$$GE = \frac{C_p}{g} \int_0^\pi [\overline{E'Q'}] dp \tag{B-21}$$

$$GZ = \frac{C_p}{g} \int_0^\pi [\overline{E}\,\overline{Q}] dp \tag{B-22}$$

$$PAE = \frac{C_p}{g} [\overline{E'_s T'_s \frac{\partial \pi}{\partial t}}] \tag{B-23}$$

$$PAZ = \frac{C_p}{g} [\overline{E}_s \overline{T}_s \overline{\frac{\partial \pi}{\partial t}}] \tag{B-24}$$

$$PKE = \frac{1}{g} [\overline{\frac{V'_s \cdot V'_s}{2} \frac{\partial \pi}{\partial t}}] \tag{B-25}$$

$$PKZ = \frac{1}{g} [\overline{\frac{V_s \cdot V_s}{2}} \overline{\frac{\partial \pi}{\partial t}}] \tag{B-26}$$

The following is a description of these terms: CA is the conversion of energy between AZ and AE; CE is the conversion of energy between AE and KE by vertical redistribution of mass, which is often referred to as baroclinic development; CK is the conversion of energy between KZ and KE, which is often referred to as the barotropic term; CZ is the conversion of energy between KZ and AZ by vertical redistribution

147

The budget equations are:

$$\frac{\partial KZ}{\partial t} = CZ + DZ - CK + PKZ \tag{B-11}$$

$$\frac{\partial KE}{\partial t} = CE + DE + CK + PKE \tag{B-12}$$

$$\frac{\partial AZ}{\partial t} = -CZ - CA + GA + PAZ \tag{B-13}$$

$$\frac{\partial AE}{\partial t} = -CE + CA + GE + PAE \tag{B-14}$$

where,

$$CA = -\frac{C_p}{g} \int_0^{\pi} [\overline{T'V'} \cdot \nabla\bar{E} + \overline{E'V'} \cdot \nabla\bar{T} - \frac{\bar{E}}{C_p}\overline{\omega'\alpha'} - \frac{\bar{\alpha}}{C_p}\overline{\omega'E'}$$
$$+ \overline{T'\omega'}\frac{\partial\bar{E}}{\partial p} + \overline{E'\omega'}\frac{\partial\bar{T}}{\partial p}]dp \tag{B-15}$$

$$CE = -\frac{1}{g}\int_0^{\pi}[\overline{\omega'\alpha'}]dp \tag{B-16}$$

$$CK = -\frac{1}{g}\int_0^{\pi}[\overline{V'\cdot(V'\cdot\nabla)\,\bar{V}}]dp - \frac{1}{g}\int_0^{\pi}[\overline{V'\cdot\omega'\frac{\partial\bar{V}}{\partial p}}] \tag{B-17}$$

$$CZ = -\frac{1}{g}\int_0^{\pi}[\bar{\omega}\bar{\alpha}]dp \tag{B-18}$$

$$DE = -\frac{1}{g}\int_0^{\pi}[\overline{V'\cdot F'}]dp \tag{B-19}$$

where E is the efficiency factor, defined as,

$$E = \frac{p^k - p_r{}^k}{p^k} \qquad (B-6)$$

The reference pressure, P_r, is the areal mean pressure on an isentropic surface. The zonal and eddy components of the kinetic energy are

$$KZ = \frac{1}{g} \int_0^\pi [\overline{\frac{\bar{V} \cdot \bar{V}}{2}}] dp \qquad (B-7)$$

and

$$KE = \frac{1}{g} \int_0^\pi [\overline{\frac{V' \cdot V'}{2}}] dp \qquad (B-8)$$

respectively. The zonal and eddy components of the available potential energy are,

$$AZ = \frac{C_p}{g} \int_0^\pi [\overline{ET}] dp \qquad (B-9)$$

and

$$AE = \frac{C_p}{g} \int_0^\pi [\overline{E'T'}] dp \qquad (B-10)$$

respectively.

APPENDIX B: ENERGY BUDGET EQUATIONS

The energy equations presented here were developed by Robertson and Smith (1983). Several boundary terms do not appear in this study because of the closed domain. The equations use the following definitions,

$$\overline{(\quad)} = \frac{1}{X} \int_0^X (\quad)\,dx \qquad\qquad (B-1)$$

is the zonal average,

$$(\quad)' = \overline{(\quad)} - (\quad) \qquad\qquad (B-2)$$

is the deviation from the zonal mean or the eddy component, and

$$[(\quad)] = \frac{1}{Y} \int_0^Y (\quad)\,dy \qquad\qquad (B-3)$$

is the average in the y-direction. The mass-integrated kinetic energy is

$$K = \frac{1}{g} \int_0^\pi \left(\frac{\mathbf{V}\cdot\mathbf{V}}{2}\right) dp \qquad\qquad (B-4)$$

and the mass-integrated available potential energy is

$$A = \frac{Cp}{g} \int_0^\pi [ET]\,dp \qquad\qquad (B-5)$$

144

as are the dynamics. Therefore, the physical parameterizations only need to be calculated at some multiple of the dynamics time step. In this study, the non-convective heating and the cumulus parameterization are applied with a 2400s time step. The heating and moistening rates are distributed uniformly over all time steps until these routines are called again. The PBL processes and the dry convective adjustment are called every dynamic step.

Moisture is condensed until saturation is reached. All condensed moisture falls into the next layer which is then checked for supersaturation. Precipitation occurs only when the air is saturated from the cloud to the ground.

3. Dry Convective Adjustment

Dry convective adjustment is applied whenever the lapse rate exceeds the dry adiabatic lapse rate. Temperatures in the unstable layer are modified such that the total potential energy is conserved. All unstable layers are adjusted subject to the conditions

$$\left| \frac{\partial \theta}{\partial \sigma} \right| \leq 10^{-3} \tag{A-36}$$

and

$$\frac{C_p}{g} \int_{\sigma_T}^{\sigma_B} (\Delta T) \, d\sigma = 0 \, , \tag{A-37}$$

where ΔT is the temperature change required to reduce the lapse rate to neutral. These equations are solved as a system of linear equations.

4. Incorporation of Physical Processes

Physical processes tend to evolve relatively slowly and are not restricted as severely by time step limitations

$$W_{sc} = \pi(\sigma_{LCL} - \sigma_{PBL})/2\Delta t \qquad\qquad (A\text{-}33)$$

where Δt is the time step for the physics routine. This acts to drive the PBL halfway down to the LCL in the absence of other effects.

Cloud temperature (T_c) and mixing ratios (q_c) are assumed to be those of the moist adiabat which passes through the LCL. The partitioning of the heating and moistening follows Kuo (1965). A value b is defined so that a fraction bM_t is used to moisten the environment and $(1-b)M_t$ condenses and falls instantaneously as rain. The value of b is defined as

$$b = \frac{1}{(\sigma_B - \sigma_T)} \int_{\sigma_B}^{\sigma_T} (1-IRH)d\sigma \qquad\qquad (A\text{-}34)$$

where IRH is the integrated relative humidity $(0 \leq IRH \leq 1)$ over the depth of the cloud,

$$IRH = \frac{1}{(\sigma_B - \sigma_T)} \int_{\sigma_B}^{\sigma_T} \left(\frac{q}{q_c}\right)d\sigma \qquad\qquad (A\text{-}35)$$

Non-convective precipitation is assumed to occur when supersaturation conditions occur at a grid point.

141

specified as 10° at all times. The time scale, S, in (A-27) is given by

$$S = -\frac{0.75(\theta_h - \theta_o)}{d\theta_o/dt}$$ (A-30)

when $(\theta_h - \theta_o) > 1°K$, and by Khakimov's (1976) equation

$$S = \frac{0.67}{f}$$ (A-31)

when $(\theta_h - \theta_o) \leq 1°K$.

2. Precipitation

A modified version of the Kuo (1965) cumulus parameterization is used. This modified version links the convection to the PBL. First, the moisture convergence, M_t, is calculated as

$$M_t = \frac{1}{g} \nabla \cdot (q_m \pi \mathbf{V}_m)(1 - \sigma_{PBL}) + \rho_s (\overline{w'q'})_s$$ (A-32)

Here, M_t is the moisture convergence occurring solely in the PBL. Convection can occur when $M_t > 4.0 \times 10^{-6}$ gm $m^{-2}s^{-1}$ and when the equivalent potential temperature decreases with height from the PBL to the first model layer above the PBL. The final constraint is that convection cannot occur if the LCL is above the PBL. In addition, if convection is occurring, the cloud-induced subsidence term (term C) in Eq. (A-23) is computed as

140

The entrainment velocity is found by iterating (A-24) and (A-26). The first term on the right-hand side of (A-24) describes the buoyant production of turbulent kinetic energy, while the second term describes the mechanical production of energy. Stull's equation for W_e also contained a term for energy loss due to internal gravity waves. This term is neglected here. Term C in (A-23) accounts for cloud-induced subsidence. The computation of this term is described later in this Appendix.

The prognostic equation for the PBL depth in stable conditions follows the development of Niewstadt and Tennekes (1981).

$$\frac{\partial(\Delta P)}{\partial t} = g\rho\left(\frac{h_e - h}{S}\right) . \tag{A-27}$$

The equilibrium height is given by

$$h_e = \frac{0.15\theta_{vm} \, f\sin\alpha \, \cos\alpha \, |V_h|^2}{g|d\theta_o/dt|} \tag{A-28}$$

over land when $|d\theta_o/dt| > 0.1°K \, hr^{-1}$ and

$$h_e = \frac{1.6u_*^2}{f|V_n|\sin\alpha} \tag{A-29}$$

over land or water when $|d\theta_o/dt| \leq 0.1°K \, hr^{-1}$ after Brost and Wyngaard (1978). The cross-isobar angle is arbitrarily

139

where α can be u, v, θ or q. By making these assumptions, the values found in the lowest layer of the model are always the mean quantities in the PBL.

The height of the PBL in unstable conditions is modeled after Stull (1976). The prognostic equation for the PBL depth (ΔP) is

$$\frac{\partial}{\partial t}(\Delta P) = -\nabla \cdot (\mathbb{V}\Delta p) + W_e + W_{sc} \qquad (A\text{-}23)$$
$$\qquad\qquad\quad (a) \qquad (b) \quad (c)$$

Term (a) defines the effect of large-scale motion on the PBL. Term (b) is the entrainment velocity given by

$$W_e = g\rho\left[\frac{0.1(\overline{w'\theta_v'})}{\Delta\theta_{vm}}\right.$$

$$\left. + \frac{\theta_{vm}}{gd_1\Delta\theta_{vm}}[0.05u_*^2|\mathbb{V}_m| + 0.001(\Delta u)^3]\right] \qquad (A\text{-}24)$$

where

$$\Delta u = \frac{u_*^2}{fh} \qquad (A\text{-}25)$$

$\Delta\theta_{vm}$ is the inversion strength at the PBL, and d_1 is the depth of the layer of negative heat flux at the top of the PBL,

$$d_1 = \frac{W_e\Delta\theta_{vm}h}{(\overline{w'\theta'_v}) + W_e\Delta\theta_{vm}}, \qquad (A\text{-}26)$$

138

respectively. Once C_u and C_θ are known, the surface stress is calculated from

$$\rho u_*^2 = \rho u_m^2 C_u^2 \qquad\qquad (A-20)$$

and the virtual temperature flux is

$$(-\overline{w' \theta_v'}) = C_\theta u_* (\theta_{vm} - \theta_{vs}). \qquad (A-21)$$

Deardorff (1972) proposed extrapolation equations to determine the mean PBL quantities. This can lead to serious problems if the PBL does not extend at least through the bottom model layer. To avoid extrapolations when the PBL is shallow, the PBL is constrained to always be at least as deep as the lowest model layer (about 40 mb). As long as the lowest layer is reasonably shallow, any errors introduced should be relatively small since such a shallow PBL will be presumably stable and the surface fluxes should be relatively small.

The PBL is assumed to always be well-mixed. Each time the model physics routines are called (this can be any integer multiple of the dynamic time step), u, v, θ and q at all model levels within the PBL are replaced by average values throughout the PBL. That is,

$$\alpha = \frac{\int_1^{\sigma_{PBL}} \alpha\, d\sigma}{(1 - \sigma_{PBL})} \qquad\qquad (A-22)$$

$$C_{\theta n} = \left[\frac{R}{k} \ln \left(\frac{0.025h}{Z_0} \right) + 7.3 \right]^{-1} \qquad (A-14)$$

and

$$Ri_C = 3.05 \qquad (A-15)$$

Ri_B was constrained to be no larger than 90% of Ri_C. The surface roughness, Z_0 is a specified constant over land and

$$Z_0 = 0.01 \, u_*^2 \qquad (A-16)$$

over water. The value of Z_0 over water is constrained to be no less than 2.435×10^{-4} m (suggested by Dr. S. Burk, NEPRF).

For unstable conditions ($Ri_B < 0$), the friction coefficient is

$$C_u = [C_{un}^{-1} - 25 \exp (0.26\xi - 0.03\xi^2)]^{-1}, \qquad (A-17)$$

and the heat transfer coefficient is

$$C_\theta = (C_{\theta n}^{-1} + C_u^{-1} + C_{un}^{-1})^{-1} , \qquad (A-18)$$

where

$$\xi = \log_{10} (-Ri_B) - 3.5 \qquad (A-19)$$

and C_{un} and $C_{\theta n}$ are given by (A-13) and (A-14),
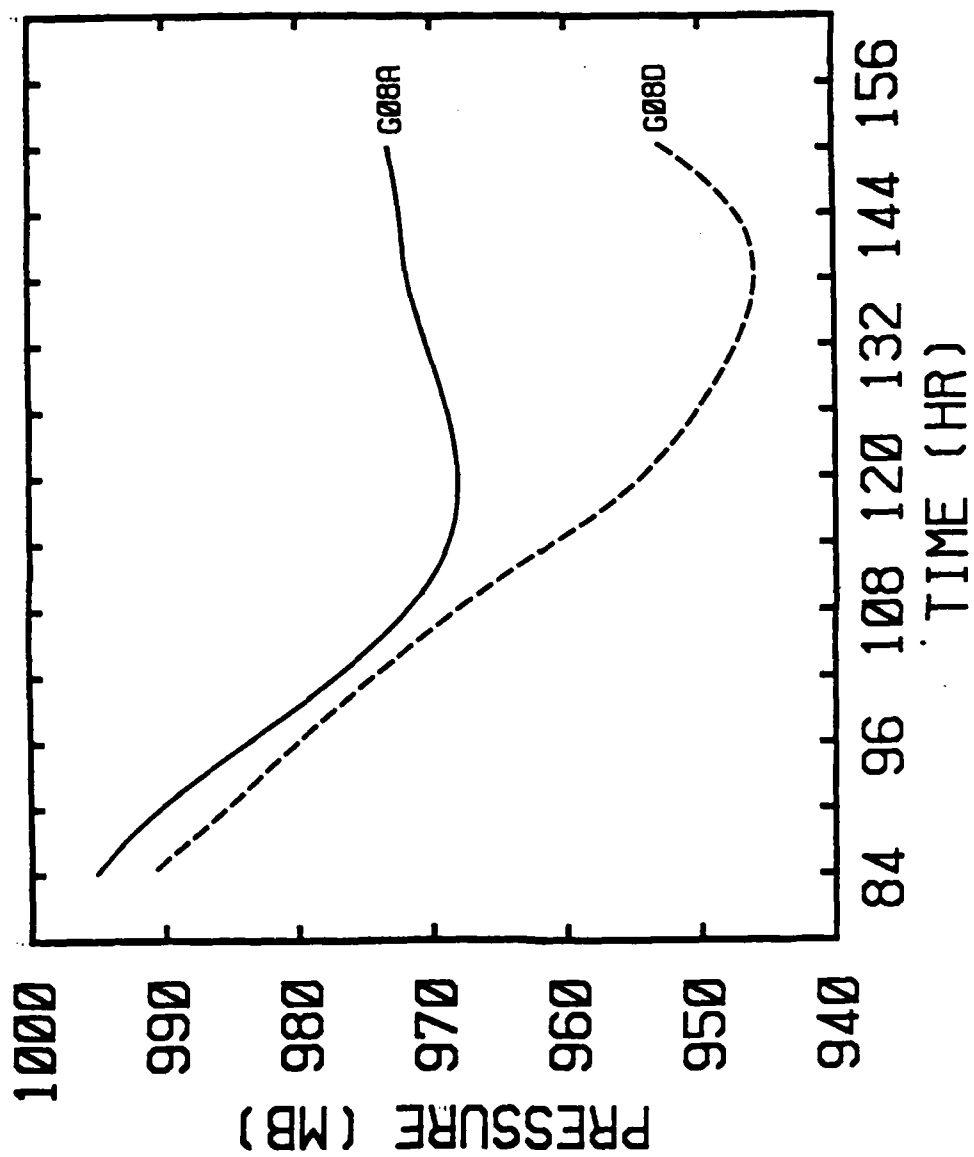
Fig. C-1. Minimum central pressure for G8A (solid) and G8D (dashed).
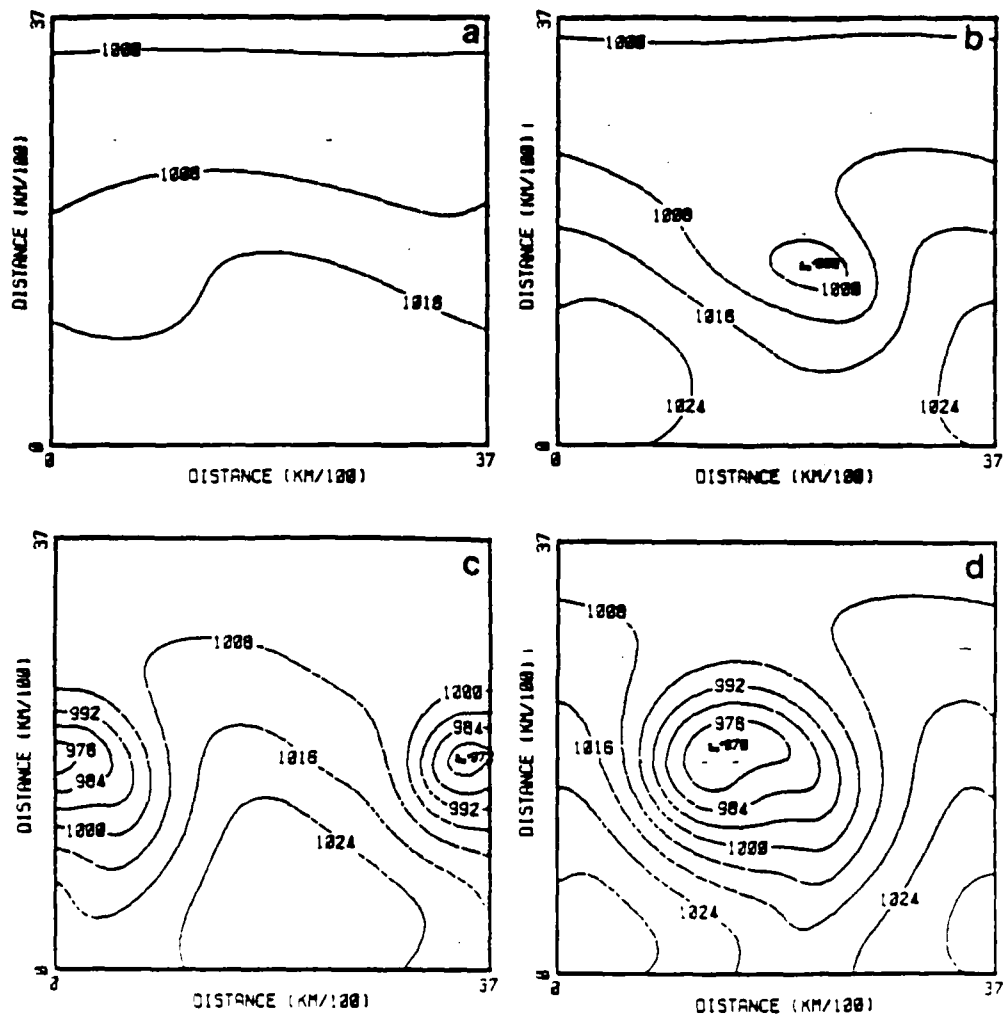
Fig. C-2.   Sea-level pressure (mb) fields for G8A at (a)
             60 h, (b) 84 h, (c) 108 h and (d) 132 h.
             Figures represent a sub-section of forecast
             domain.   Southern boundary of figure is located
             at center of forecast domain. 200 km of right
             side of domain is the same as the leftmost
             200 km due to periodicity.
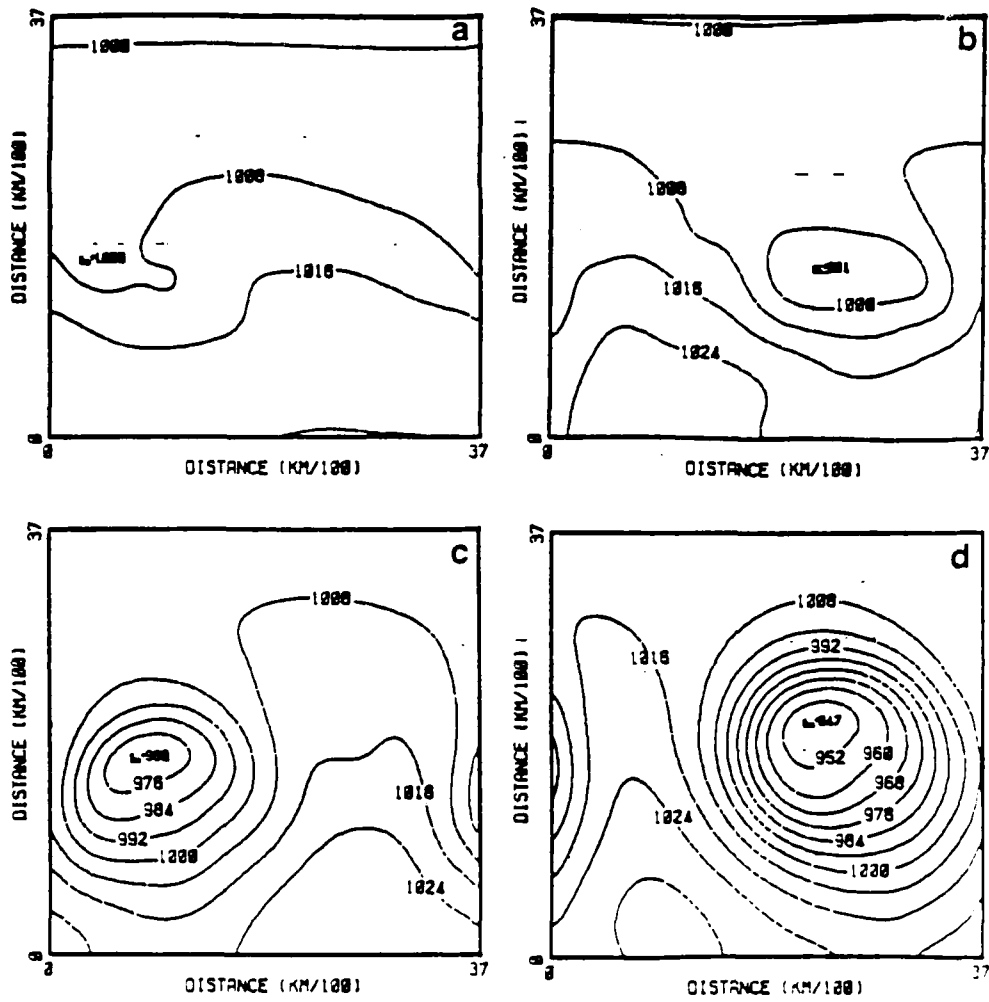
Fig. C-3.   Similar to Fig. C-2 except for G8D.

deepened to 991 mb. By 108 h, both systems have intensified further with G8A near the mature stage. At 132 h, G8A remains at nearly the same central pressure while G8D has continued to deepen and has reached the mature stage with a central pressure of 947 mb.

Cross-sections of height perturbations through G8A and G8D at 84 h are given in Fig. C-4. Both systems exhibit maximum perturbations at the surface and in the upper levels with a westward tilt with height. The upper level height perturbation is stronger in G8D than in G8A, which shows that diabatic effects tend to strengthen the upper level circulation. This is also found to be the case for the polar low (cf, Fig. 4-5). Unlike G20A, which is strongly damped in the vertical, the upper level perturbation in G8A is more than half the magnitude of the surface perturbation. This again illustrates that shorter waves tend to be shallow disturbances as found in Chapter III.

Cross-sections of vertical motion, temperature and the trough axis for G8A and G8D at 84 h are shown in Fig. C-5. The adiabatic case exhibits a warm perturbation extending from the surface to 400 mb. The center of the warmest air tilts eastward with height from the surface to 500 mb, and westward above 500 mb. A center of upward vertical motion occurs just east of the surface low in the warmest air, which implies an increase of KE over a deep layer due to this thermally direct circulation. This is in contrast to
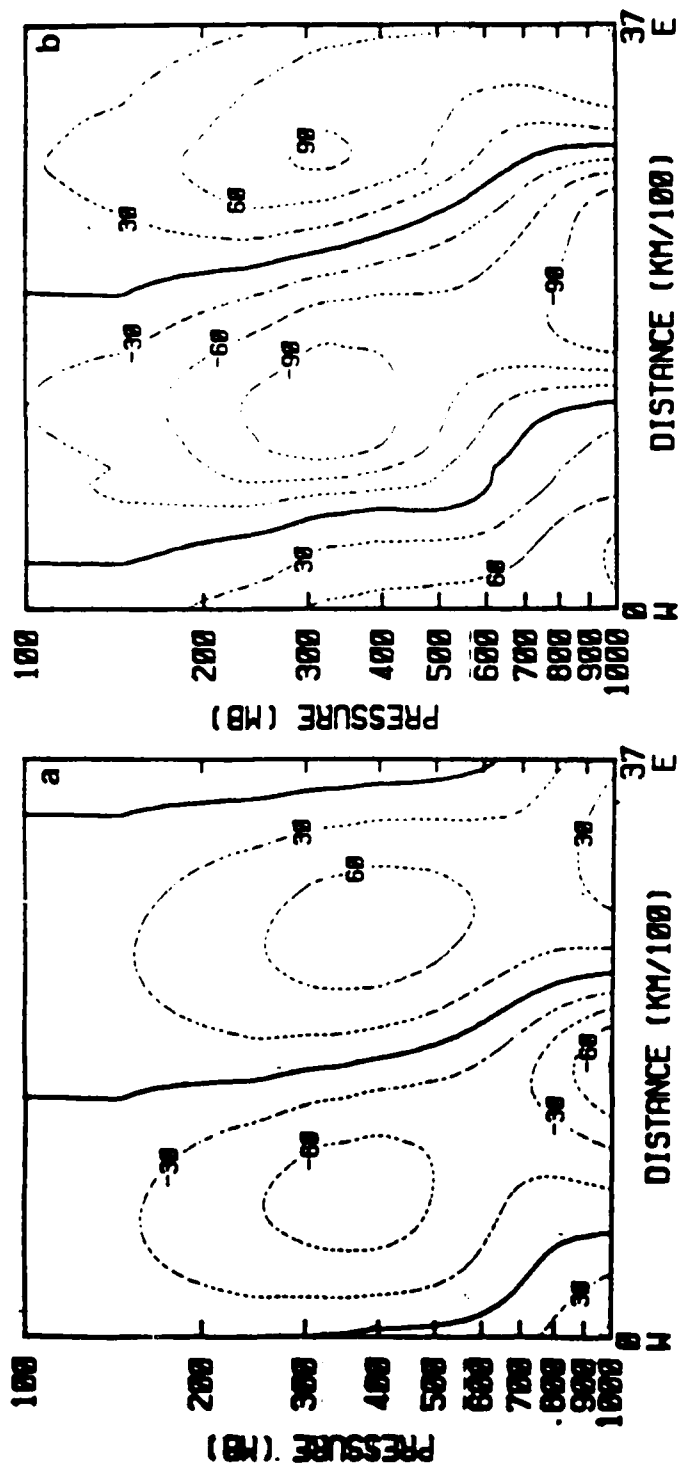
Fig. C-4. East-west cross-sections of height perturbations through
surface pressure center for (a) G8A and (b) G8D at 84h.
Contour interval is 30 m. Heavy dark line is zero
contour. 200 km of right side of domain is the same
as the leftmost 200 km due to periodicity.

Fig. C-5. East-west cross-sections of ω (dashed line; heavy solid line is zero contour), T (light solid line) and trough position (heavy dashed line) for (a) G8A and (b) G8D at 84 h. Contour interval for ω is 2 μbar/s in (a) and 5 μbar/s in (b). Contour interval for T is 10 K. 200 km of right side of domain is the same as leftmost 200 km due to periodicity.

155

the polar low, G20A (Fig. 4-2), which exhibits very little tilt to the warm air perturbation from the surface to 750 mb with a strong westward tilt above 750 mb.

Significant differences exist between the cross-sections of G8A and G8D. First, the center of upward vertical motion and the warmest air in G8D are found about 750 km east of their respective positions in G8A. This is a result of the convection taking place ahead of the surface low as noted above. Second, in G8D, a narrow band of upward motion within a weak warm air perturbation is found in the cold air about 1000 km behind the position of the surface low. The surface reflection of this feature is the weak pressure trough in the northwest flow in G8D at 84 h (Fig. C-3b). This pressure trough is a weak polar low and its formation is related to an interaction between convection and the PBL. Forecast PBL depths in the cold air behind the trough are relatively large because the maximum air-sea temperature differences are in this area. Some convection (about 5 mm/ 12 h) is forecast behind the surface low in the cold air. This results in a decrease in the PBL height at the convec- tive points due to cloud-induced subsidence (Eq. A-33). At the points where the PBL is deep, relatively strong PBL winds exist due to the mixing of the winds throughout the PBL. At the convective points, where the PBL is shallow, relatively light winds exist since the stronger winds aloft are not being mixed into the PBL. This sets up a zone of

convergence in the PBL on the western edge of convective areas which further enhances convective forcing of this system. While this process is capable of producing small-scale, cold air disturbances in this model, it is felt that this is more of a numerically induced feature as opposed to a physically realistic situation. Certainly, not all convection drives the PBL halfway down to the LCL every half hour as is assumed here. However, large variations in PBL depth over a small area in the presence of strong vertical wind shear should be considered as a possible mechanism to trigger polar low development.

The total, convective and stable precipitation accumulated in G8D during the 12 h period ending at 108 h are shown in Fig. C-6. About 26 mm of precipitation is forecast to the north of the disturbance with a maximum of 38 mm to the southeast of the low along the cold front. Only about 40% of the northern maximum and 2/3 of the southern maximum in precipitation is convective. Therefore, the percentage of convective precipitation is smaller in G8D than in the polar low, G20D.

The effect of the diabatic processes can be seen in Figs. C-7 and C-8 in which the 850, 700 and 500 mb height and temperature fields are given for G8A and G8D, respectively. As with the polar low in Chapter IV, a noticeable

157
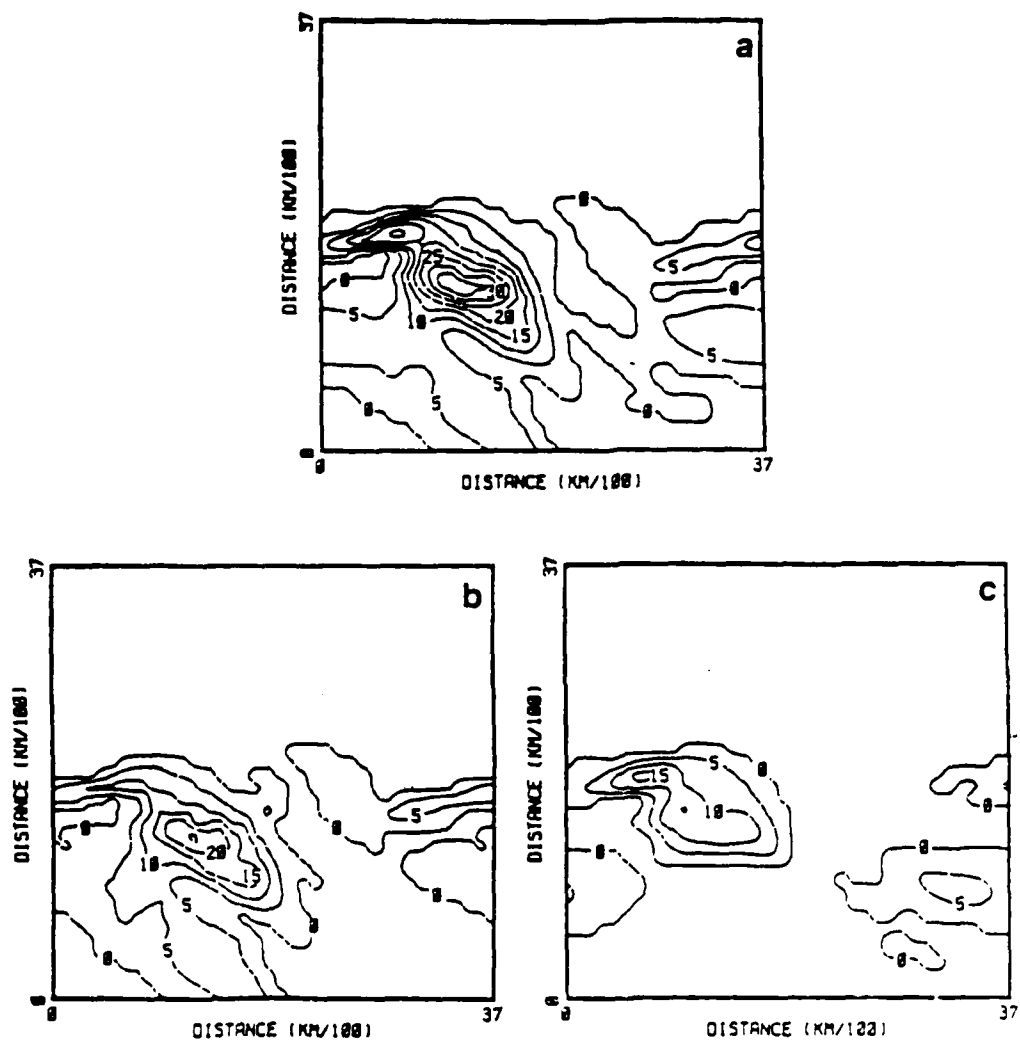
Fig. C-6.   12 h accumulation of (a) total, (b) convective
            and (c) stable precipitation in a fixed-frame
            reference ending at 108 h for G8D. Contour
            interval is 5 mm. Grid placement as in Fig. C-2.

158
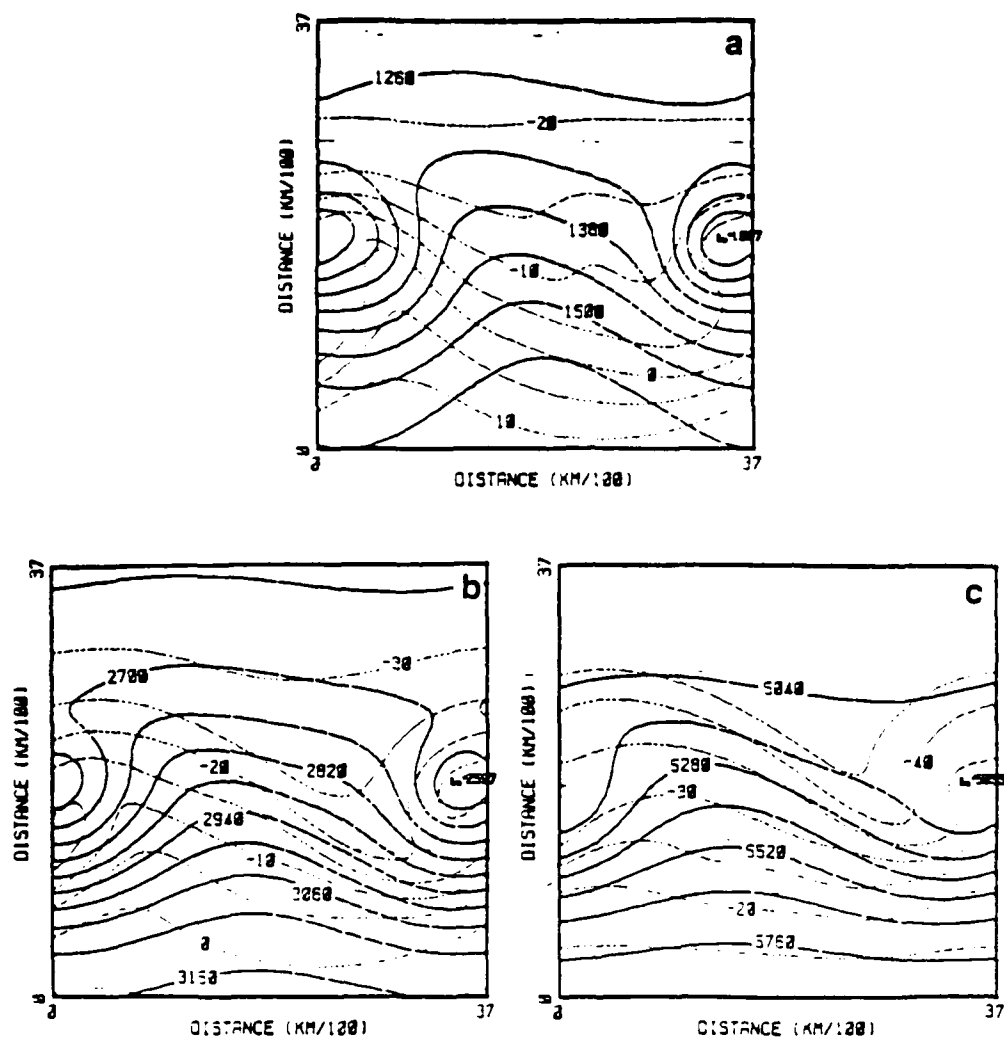
Fig. C-7. Fields of height and temperature at (a) 850 mb,
          (b) 700 mb and (c) 500 mb at 108 h for G8A.
          Contour interval for height is 60 m in (a) and
          (b) and 120 m in (c). Grid placement as in
          Fig. C-2.
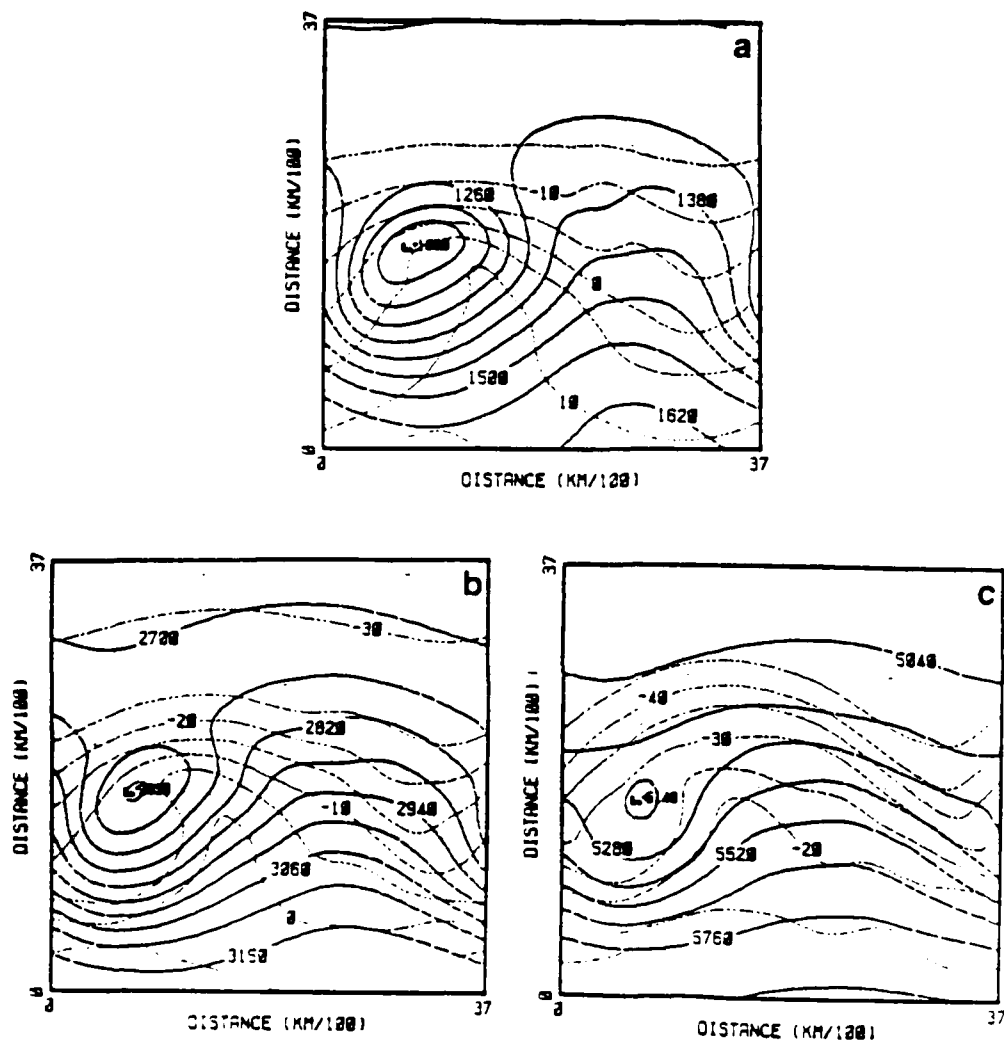
Fig. C-8.   Similar to Fig. C-7 except for G8D.

160

warming occurs ahead of the developing wave due to the
release of latent heat in this area, which reduces the
effect of adiabatic cooling through ascent.

The surface sensible and latent heat fluxes associated
with G8D at 108 h are shown in Fig. C-9. Maximum values of
the fluxes are found behind the developing wave in the
colder air, as noted with the polar low (cf, Fig. 4-11).
However, unlike the polar low, downward (negative) fluxes
occur ahead of G8D in the warm sector. This results from a
large low-level temperature perturbation (Fig. C-8a) in G8D
which reverses the sign of the air-sea temperature differ-
ence in the warm sector.

KE budgets for G8A and G8D, integrated over the forecast
domain, are presented in 6 h intervals in Tables C-1 and
C-2, respectively. The maximum KE attained by G8A, 6.7 x
10^5 J m^{-2}, is about 40% less than the maximum attained by
G8D, 11.1 x 10^5 J m^{-2}. This is in sharp contrast to the
results in Chapter IV that the diabatic effects led to an
order of magnitude increase in KE for G20D. The reason why
G8D does not exhibit a similar increase in magnitude over
G8A can be seen from Fig. C-10, which gives the time-height
cross-sections of KE for G8A and G8D. For the polar low
discussed in Chapter IV, the adiabatic run exhibits a maxi-
mum of KE near the surface with negligible amounts above
600 mb. However, G8A exhibits a maximum KE of 5 x 10^4 J m^{-2}
near 350 mb with a secondary maximum of 3 x 10^4 J m^{-2} near

161
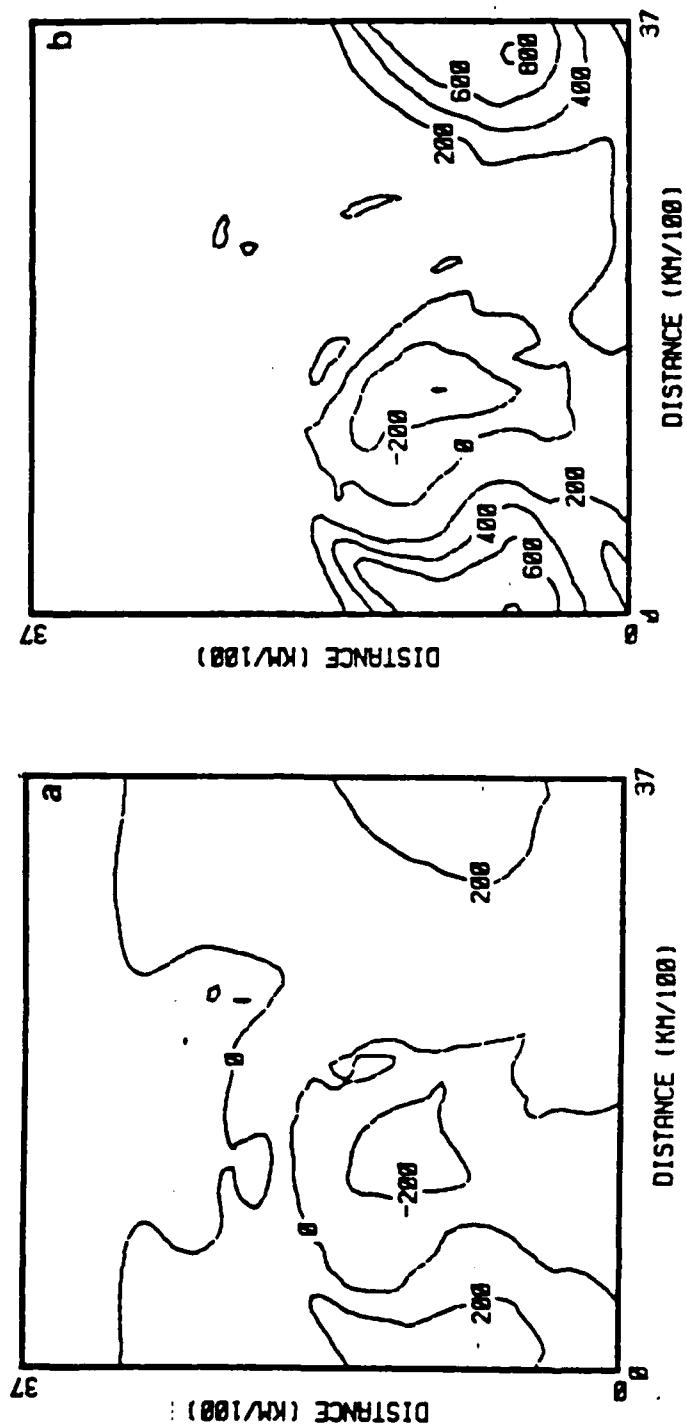
Fig. C-9. Fields of (a) sensible heat flux and (b) latent heat flux at 108 h for G8D. Contour interval is 200 W m-2. Grid placement as in Fig. C-2.

162

Table C-1. KE budgets for G8A. KE in units of 10^3 Jm^{-2}.
All other budget terms in units of Wm^{-2}.

Time (hr)	KE	$\partial KE/\partial t$	CE	HCK	VCK	DE
60	11.9	.29	.31	-.06	.11	-.08
66	19.9	.49	.51	-.11	.18	-.13
72	32.9	.77	.84	-.19	.29	-.22
78	53.0	1.16	1.35	-.34	.44	-.37
84	83.0	1.68	2.10	-.57	.62	-.62
90	125.5	2.33	3.12	-.82	.81	-1.03
96	183.6	3.08	4.36	-1.03	.99	-1.63
102	258.4	3.78	5.73	-1.26	1.16	-2.48
108	346.9	4.22	7.12	-1.71	1.37	-3.60
114	440.8	4.21	8.16	-2.33	1.64	-4.85
120	528.8	3.68	8.46	-2.82	1.85	-5.91
126	600.0	2.77	7.98	-3.09	1.92	-6.55
132	648.3	1.67	6.94	-3.03	1.78	-6.72
138	672.1	.48	5.66	-2.71	1.54	-6.71
144	669.1	-.78	3.93	-2.23	1.27	-6.51
150	638.6	-1.80	2.22	-1.94	1.05	-5.71

in Fig. C-16. Although G8A suggests a maximum near 450 mb and another near 800 mb, both forecasts exhibit large values throughout the 900-300 mb layer. A similar pattern is found for G20D except over a slightly shallower layer.

Noticeable differences exist in the vertical eddy heat transport term, VCA, between G8A and G8D. In the adiabatic run, VCA is positive during the developing stage up to 102 h, which indicates that VCA is a source of AE. After 102 h, VCA is negative and tends to damp the wave. However, values of VCA are generally 4-10 times less than the largest term, HCA. In G8D, VCA is positive through 90 h. While G8D is deepening rapidly from 96-144 h, VCA is negative (except at 120 h) and is very small in magnitude. Even though VCA is negative during this time, the values are not as large in magnitude as in G8A, and therefore more AE is available in G8D. Time-height cross-sections of VCA for G8A and G8D are given in Fig. C-17. Generally, negative values are found above 500 mb. Below 500 mb, G8A is dominated by positive values prior to 108 h and negative values after 108 h. The same tendency exists in G8D except that positive values persist at all times below 800 mb.

The destruction of AE by VCA in G8A and G8D during the growth stage is different from that found in the polar low. In G20D, generation of AE through VCA during the developing stage was found to be approximately the same magnitude as term HCA. The reason for this appears to be the area in
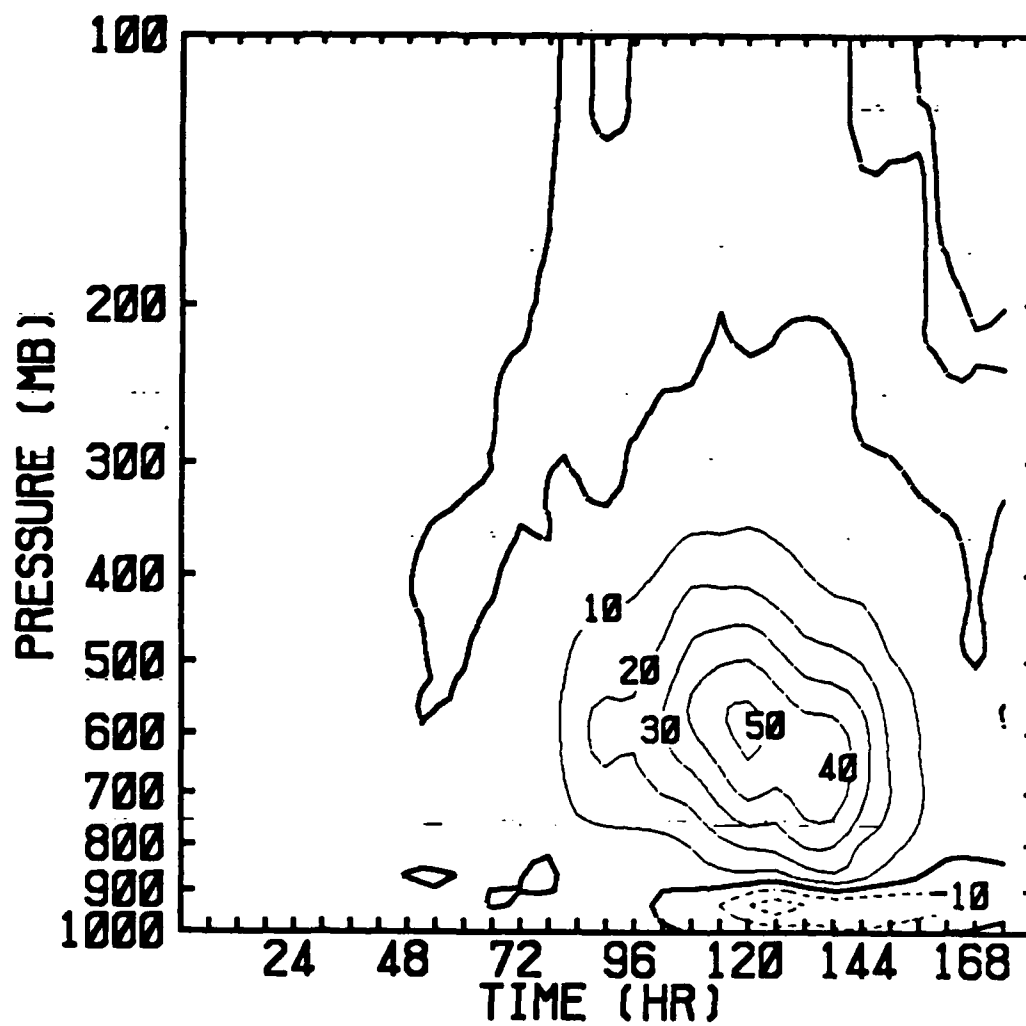
Fig. C-15.   Time-height cross-section of GE for G8D.
Contour interval is 10×10^{-3} W m^{-2}. Format
of contours as in Fig. C-11.

176

and G8D occur in the 700-500 mb layer from 120-132 h (Fig. C-11). This is at the same time and location in which the large increases in AE are observed, which suggests that the disturbance uses the additional AE for baroclinic development of the storm.

The generation of AE by diabatic processes, GE, attains maximum values from 114-138 h. This is consistent with the large increases in AE noted during this time. The time-height cross-section of GE for G8D is given in Fig. C-15. The largest values from 114-138 h are found in the 700-500 mb layer. This is attributed to the latent heat release primarily in the warm sector ahead of the low as discussed above. Negative values of GE in the lowest 100 mb are the result of positive (negative) sensible heat fluxes occurring in the cold (warm) air behind (ahead of) the low. This pattern of GE resembles that for G20D (Fig. 4-17).

The horizontal eddy heat transport, HCA, is positive for both G8A and G8D, which indicates that it is a source of AE. During the developing stages of G8A and G8D, HCA is the largest term in the AE budget. Values of HCA are up to two times larger in G8D, which suggests that the diabatic processes have altered the overall temperature distribution of the disturbance so as to increase the horizontal eddy heat transport. This was shown in Chapter IV to play a significant role in the intensification of the polar low. Time-height cross-sections of HCA for G8A and G8D are given

175
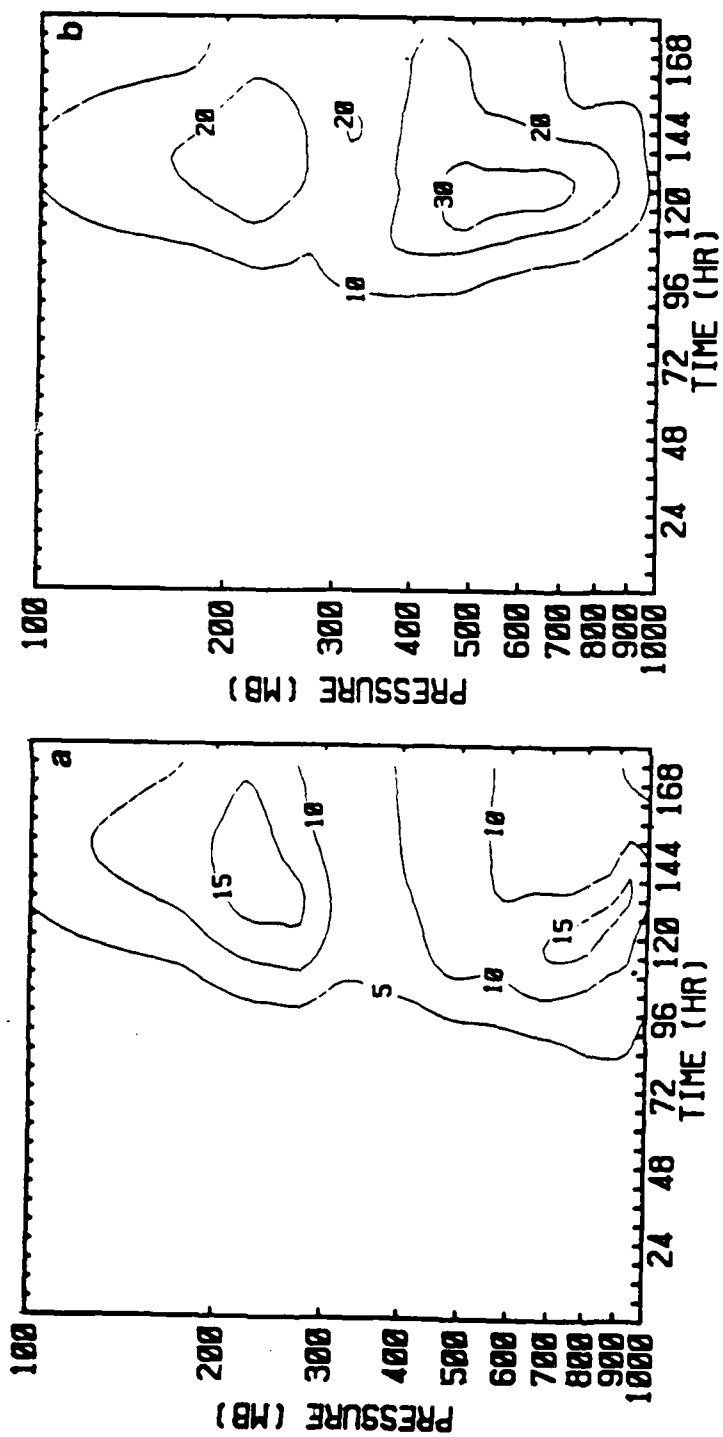
Fig. C-14. Time-height cross-sections of AE for (a) G8A and (b) G8D. Contour interval is 5 x 10-3 J m-2 in (a) and 10 x 10-3 J m-2 in (b).

Table C-4. Similar to Table C-3 except for G8D.

Time (hr)	AE	$\partial AE/\partial t$	CE	GE	HCA	VCA
60	11.7	.37	.70	.10	.53	.52
66	22.2	.63	1.42	.32	1.05	.89
72	38.8	.88	2.01	.52	1.95	.76
78	60.1	1.08	2.69	.33	3.13	.66
84	85.8	1.20	4.28	1.09	4.54	.78
90	111.9	1.36	5.28	1.38	5.82	.07
96	144.5	1.70	5.77	1.48	7.51	-.36
102	185.5	2.39	7.39	1.88	9.65	-.60
108	247.8	3.13	9.58	2.51	12.33	-.44
114	320.9	3.30	12.14	3.08	14.48	-.11
120	390.5	2.47	13.84	3.39	14.97	.22
126	427.7	.82	13.23	2.88	13.95	-.03
132	426.1	-.92	12.81	3.05	11.99	-.90
138	387.8	-2.05	10.63	2.97	8.79	-1.09
144	337.6	-2.22	7.11	2.02	5.18	-.43
150	291.9	-1.92	3.57	1.09	1.68	.37

Table C-3. AE budgets for G8A. AE in units of 10^3 Jm^{-2}. All other budget terms in units of Wm^{-2}.

Time (hr)	AE	$\partial AE/\partial t$	CE	HCA	VCA
60	8.5	.20	.31	.39	.13
66	13.9	.32	.51	.63	.20
72	22.1	.47	.84	1.03	.31
78	34.2	.66	1.35	1.62	.46
84	50.8	.88	2.10	7.49	.62
90	72.2	1.11	3.12	3.68	.76
96	98.8	1.36	4.36	5.29	.76
102	130.8	1.55	5.73	7.29	.51
108	165.7	1.52	7.12	9.38	.00
114	196.4	1.17	8.16	10.89	-.79
120	216.0	.63	8.46	11.54	-1.69
126	223.7	.15	7.98	11.25	-2.36
132	222.6	-.25	6.94	10.04	-2.60
138	212.8	-.59	5.66	8.13	-2.37
144	197.2	-.66	3.93	5.74	-1.82
150	184.2	-.50	2.22	3.48	-1.20
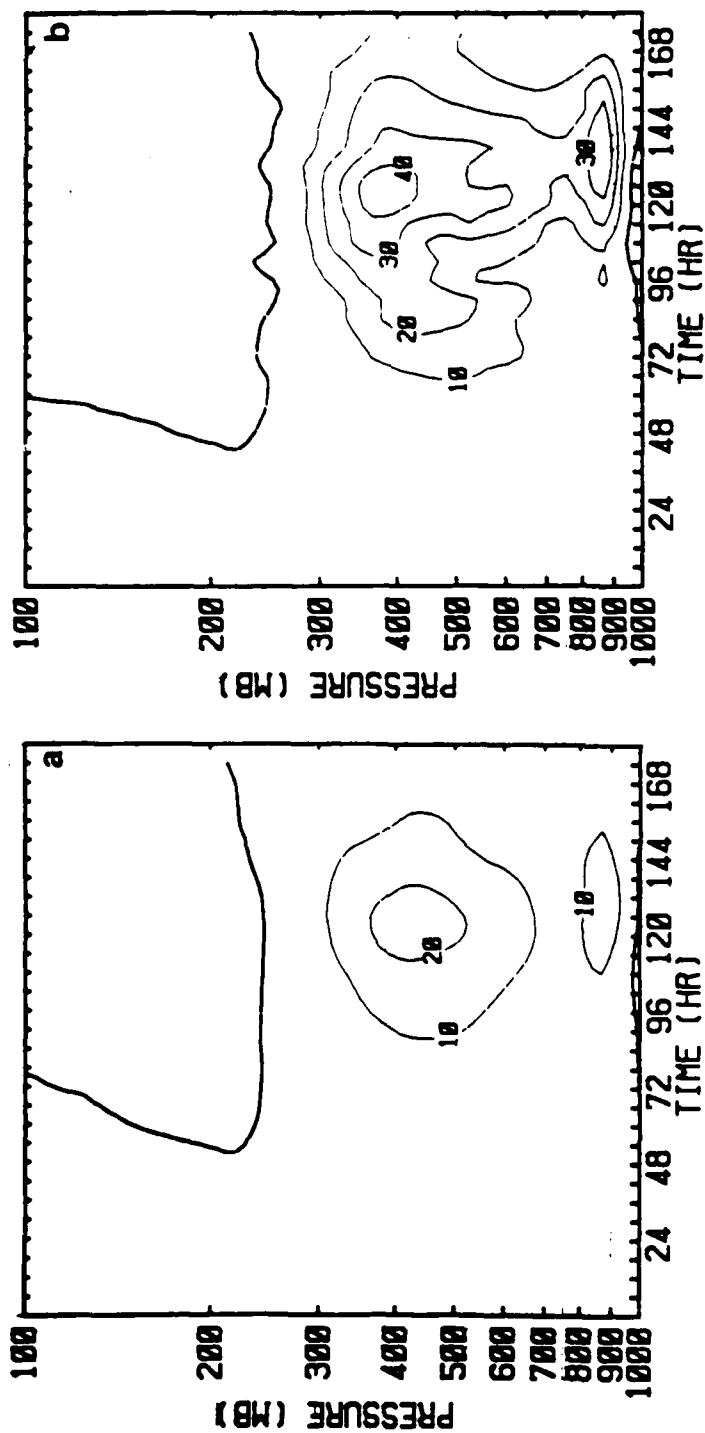
Fig. C-13. Time-height cross-sections of VCK for (a) G8A and (b) G8D. Contour interval is 10×10^{-2} W m^{-2}. Format of contours as in Fig. C-11.

cross-sections of VCK for G8A and G8D are given in Fig. C-13. Both disturbances exhibit maximum values of VCK of approximately the same magnitude between 850-900 mb and near 400 mb.

Frictional dissipation, DE, acts as a sink of KE for both forecasts. DE is the largest term in both G8A and G8D once the disturbance reaches its maximum intensity. This is in contrast to G20D, which exhibited larger values of HCK than DE during the decaying stage of the polar low. However, the trends here are similar since for G8A, DE is 2.2 times larger than HCK at 132 h while for G8D, DE is 1.7 times as large as HCK at the same time. Therefore, barotropic damping is larger relative to DE when diabatic effects are included.

AE budgets integrated over the forecast domain are presented in 6 h intervals for G8A and G8D in Tables C-3 and C-4, respectively. As was the case for the polar low, G8D exhibits more AE than G8A. The maximum values for G8A, 2.2 x 10^5 J m^{-2}, and for G8D, 4.3 x 10^5 J m^{-2}, occur at 126 h. Time-height cross-sections of AE for G8A and G8D are given in Fig. C-14. Although G8D exhibits larger values of AE at all levels, the most significant increase over G8A occurs in the mid-levels from 700-500 mb. AE values for G8D in this layer are three times larger from 120-132 h when the central pressure fell 7 mb in G8D and rose 2 mb in G8A. It was noted earlier that the largest differences in CE between G8A

170
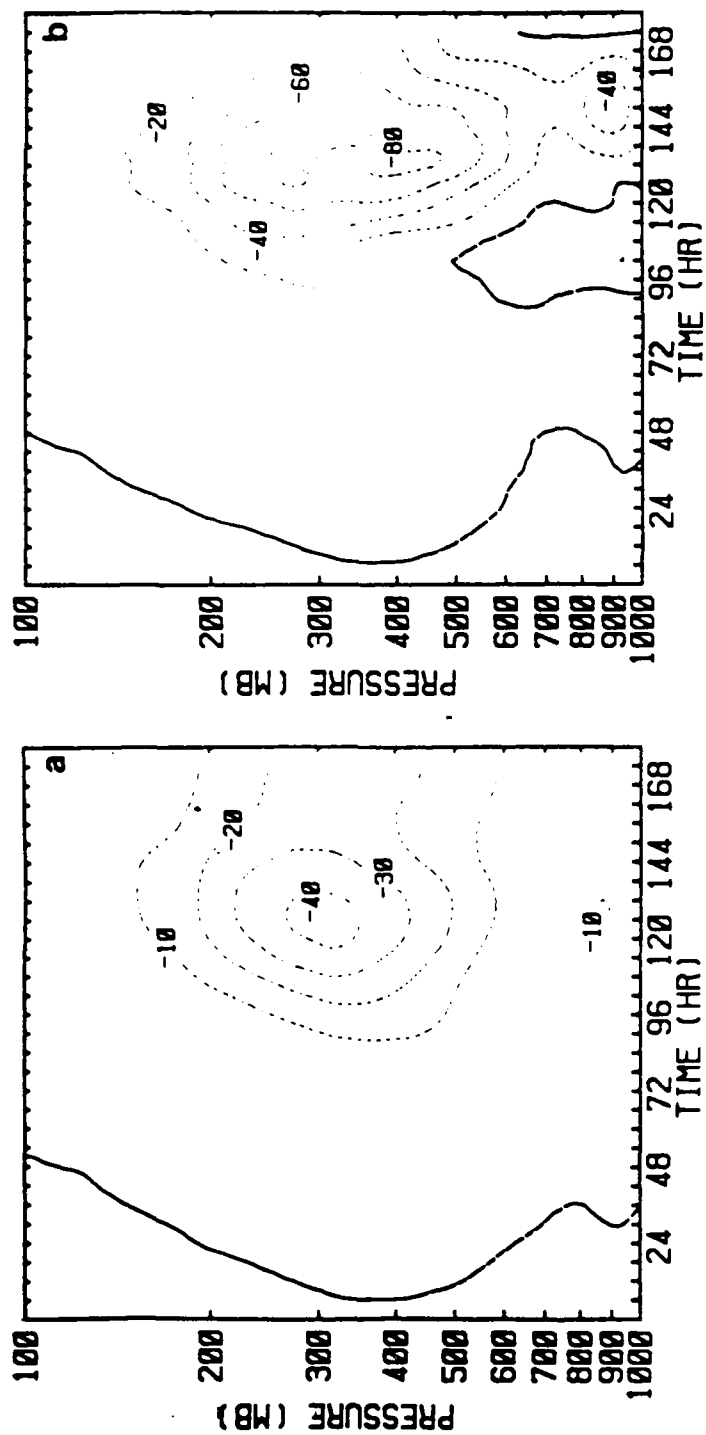
Fig. C-12. Time-height cross sections of HCK for (a) G8A and (b) G8D. Contour interval is 10 x 10-2 W m-2 in (a) and 20 x 10-2 W m-2 in (b). Format of contours as in Fig C-11.

in G8A. The vertical structure of CE is very similar between the diabatic simulations of G20 (cf, Fig. 4-13) and G8.

The horizontal barotropic term, HCK, is a sink of KE in both forecasts. Maximum values of HCK are found at the mature stages of G8A and G8D. Time-height cross-sections of HCK are given in Fig. C-12. The largest values of HCK are found in the upper levels associated with the jet. Also in G8D, positive values of HCK are found below 600 mb from 96-114 h. The reason for this is the southeastward extension of the developing trough forced by convection as seen in the surface pressure field for G8D (Fig. C-3). This pattern implies a positive correlation between u' and v' and hence a conversion of KE to KZ by HCK.

The vertical component of CK, VCK, is positive throughout both forecasts, and therefore represents a source of KE. As with the polar low forecasts, VCK is a maximum 6-12 h after CE reaches its maximum value near the mature stage of the cyclone. This should be expected since u' and ω' are largest then. The fact that VCK attains its largest values at or just after maximum storm intensity suggests that this process is a symptom of the baroclinic disturbance rather than a cause, as is also the case for HCK. Therefore, both G20 and G8 are considered to be disturbances which form through conventional baroclinic instability. Time-height
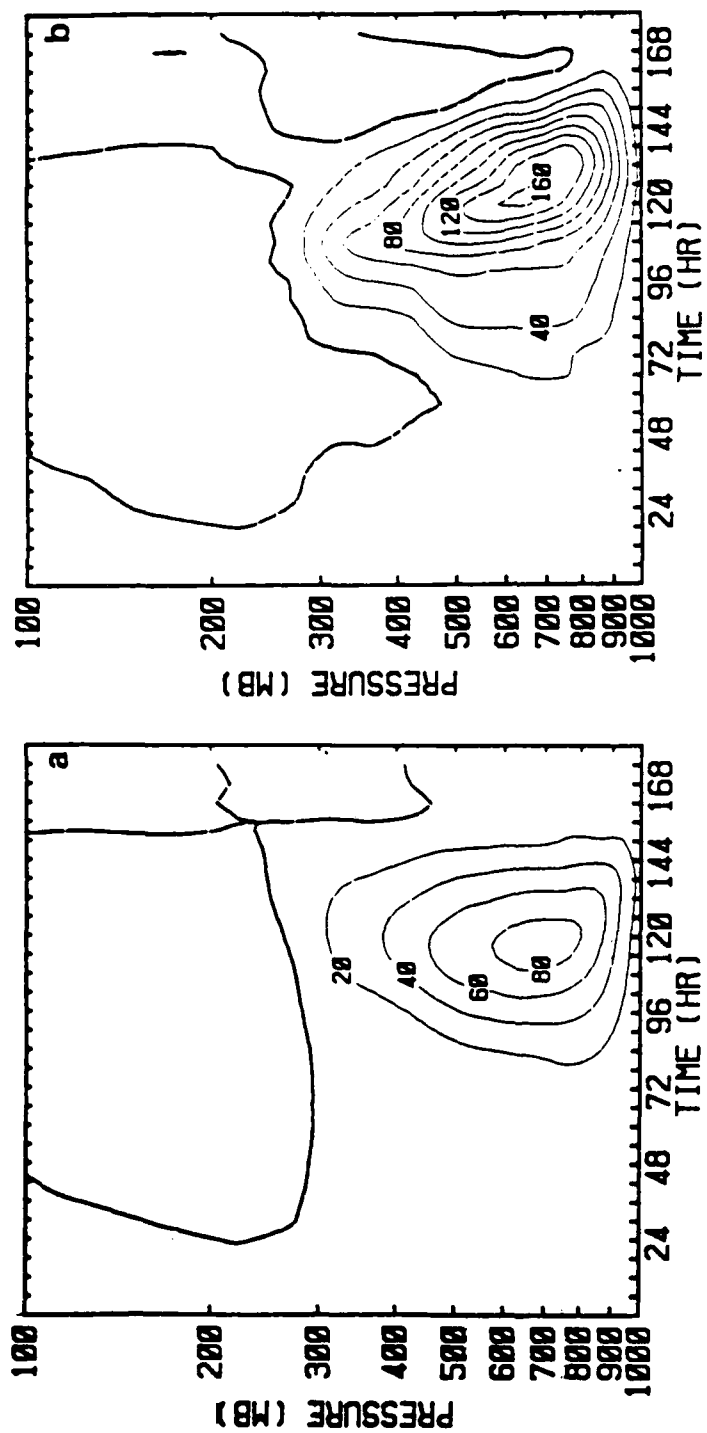
Fig. C-11. Time-height cross-sections of CE for (a) G8A and (b) G8D. Contour interval is 20 x 10-2 W m-2. Heavy solid line is zero contour, light solid line is positive contour and dashed line is negative contour.

167

900 mb. Therefore, the reason G20D realizes such a large
increase of KE when diabatic effects are included is that
G20A is a very shallow system and the domain-integrated KE
is quite small. With diabatic effects, the polar low
extends through a large part of the troposphere and yields
a much larger domain-integrated KE. G8A already extends
through the troposphere and the only other way to increase
the domain-integrated KE is to increase the circulation of
the system. This occurs in G8D and results in KE maxima of
9×10^4 J m^{-2} at 350 mb and 6×10^4 J m^{-2} at 900 mb.

The baroclinic development term, CE, is the largest term
in the budgets for both G8A and G8D through 132 h. During
the developmental stages prior to 120 h, CE is 1-1/2 to 2
times larger in G8D and is the largest term in the KE
budgets. Time-height cross-sections of CE are given in
Fig. C-11. Both forecasts exhibit maximum conversion of AE
to KE at 700 mb, which is near the level of maximum vertical
motion. Large differences exist between the vertical struc-
ture of CE for G8A and G20A. G20A exhibits maximum CE near
900 mb with negative values above 700 mb. This is a result
of the warm air perturbation tilting sharply westward above
750 mb. However, the warm air perturbation in G8A tilts
eastward with height up to 500 mb during the development
stage. This results in positive values of CE up to 300 mb

166
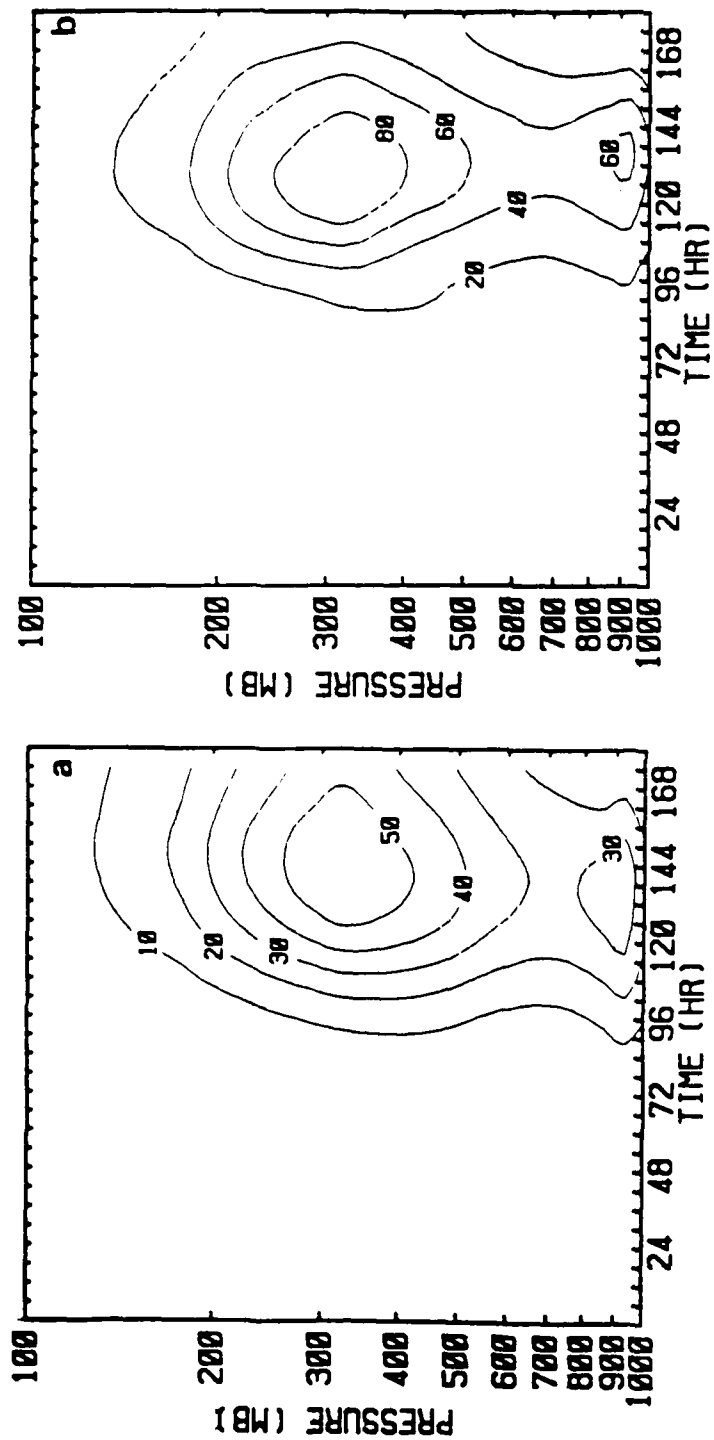
Fig. C-10. Time-height cross-sections of KE for (a) G8A and (b) G8D. Contour interval is 10 x 103 J m-2 in (a) and 20 x 103 J m-2 in (b).

165

Table C-2. Similar to Table C-1 except for 68D.

| Time (hr)	KE	$\partial KE/\partial t$	CE	HCK	VCK	DE
60	21.6	.78	.70	-.10	.39	-.16
66	44.6	1.34	1.42	-.24	.82	-.37
72	79.6	1.81	2.01	-.53	1.20	-.53
78	122.9	2.48	2.69	-.75	1.41	-.80
84	186.6	3.26	4.28	-.94	1.69	-1.26
90	263.7	3.80	5.28	-1.20	1.67	-1.68
96	350.8	4.81	5.77	-1.50	1.52	-2.42
102	471.5	6.16	7.39	.34	1.56	-3.25
108	616.9	7.16	9.58	-.41	1.88	-4.37
114	780.9	7.63	12.14	-2.30	2.55	-5.99
120	946.8	6.45	13.84	-4.10	3.44	-8.02
126	1060.0	3.74	13.23	-5.80	3.60	-10.38
132	1109.0	.52	12.81	-7.43	3.66	-12.67
138	1082.0	-2.88	10.63	-8.49	3.55	-12.83
144	984.0	-5.75	7.11	-8.57	3.07	-10.74
150	833.7	-7.30	3.57	-8.20	2.63	-8.22
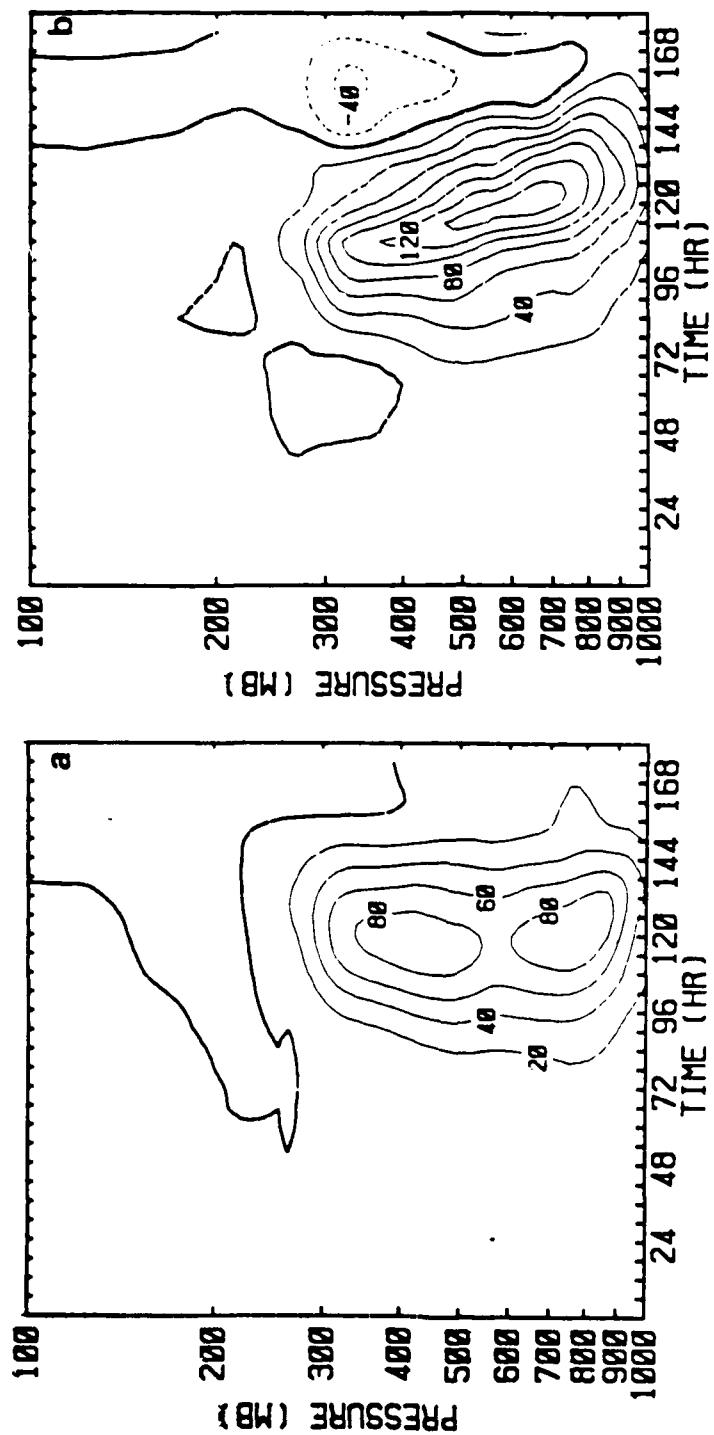
Fig. C-16. Time-height cross-sections of HCA for (a) G8A and (b) G8D.
Contour interval is 20×10^{-3} W m^{-2}. Format of contours
as in Fig. C-11.

178

Fig. C-17. Time-height cross-sections of VCA for (a) G8A and (b) G8D.
Contour interval is 20 x 10-3 W m-2. Format of contours
as in Fig. C-11.

179

which the low develops. VCA is comprised of the four
terms: a) $\overline{\omega'\alpha'}\,\overline{E}/C_p$; b) $\overline{\omega'E'}\,\overline{\alpha}/C_p$; c) $(\overline{\omega'T'}\,\partial\overline{E}/\partial p)$; and d)
$(-\overline{\omega'E'}\,\partial\overline{T}/\partial p)$. Term a is generally an order of magnitude
less than the other terms, so VCA is a balance between term
b, which is typically less than zero, and terms c and d,
which are typically positive. The relative strength of each
term governs the sign of VCA. In G20D, term b tends to be
relatively small since this disturbance forms 250-500 km
farther to the north than in G8 and therefore α is smaller.
This reduces the magnitude of term b and VCA is positive.

The results of the G8 simulations presented here illus-
trate the following points. First, diabatic processes serve
to intensify an extratropical, synoptic-scale disturbance in
a similar manner to the Pacific polar low. Specifically,
the diabatic processes serve to alter the temperature struc-
ture of both G8 and G20 such that eddy heat transport, and
therefore values of AE, are increased. The direct genera-
tion of AE by diabatic processes (GE) is found to be at
least 5 times smaller than the eddy heat transport in both
G8 and G20. Second, patterns of surface pressure, precipi-
tation, wind and temperature for a Pacific polar low are
found to resemble those of synoptic-scale oceanic
disturbances.

LIST OF REFERENCES

Arakawa, A., and V. R. Lamb, 1977: Computational design of the UCLA general circulation model. Methods in Computational Physics, Vol. 17, Academic Press, 173- 265.

Bennetts, D. A., and Hoskins, B. J., 1979: Conditional symmetric instability - a possible explanation for frontal rainbands. Quart. J. R. Meteor. Soc., 105, 945-962.

Brost, R. A., and J. C. Wyngaard, 1978: A model study of the stably stratified boundary layer. J. Atmos. Sci., 35, 1427-1440.

Bullock, B. R., and D. R. Johnson, 1971: The generation of available potential energy by latent heat release in a mid-latitude cyclone. Mon. Wea. Rev., 99, 1-14.

Charney, J. G., 1947: The dynamics of long waves in a baroclinic westerly current. J. Meteor., 4, 135-162.

Crutcher, H. L., and J. M. Meserve, 1970: Selected level heights, temperatures and dew points for the Northern Hemisphere. NAVAIR, Rev., Chief of Naval Operations, Washington, DC, 17pp + charts.

Danard, M. B., and G. V. Rao, 1972: Numerical study of the effects of the Great Lakes on a winter cyclone. Mon. Wea. Rev., 100, 374-382.

Deardorff, J. W., 1972: Parameterization of the planetary boundary layer for use in general circulation models. Mon. Wea. Rev., 100, 93-106.

Duncan, C. N., 1977: A numerical investigation of polar lows. Quart. J. R. Meteor. Soc., 103, 255-267.

Eady, E. T., 1949: Long waves and cyclone waves. Tellus, 1, 33-52.

Forbes, G. S., and J. H. Merritt, 1984: Mesoscale vorticities over the Great Lakes in wintertime. Mon. Wea. Rev., 112, 377-381.

Gall, R. L., 1976a: A comparison of linear baroclinic
    instability theory with the eddy statistics of a
    general circulation model. J. Atmos. Sci., 33, 349-373.
    Gall, R. L., 1976b: Structural changes of growing baro-
    clinic waves. J. Atmos. Sci., 33, 374-390.

Gall, R. L., 1976c: The effects of released latent heat
    growing baroclinic waves. J. Atmos. Sci., 33, 1686-
    1686-1701.

Gall, R. L., R. Blakeslee, and R. C. J. Somerville, 1979:
    Baroclinic instability and the selection of the zonal
    scale of the transient eddies of middle latitudes. J.
    Atmos. Sci., 36, 767-784.

Gambo, K., 1970: The characteristic feature of the medium-
    scale disturbances in the atmosphere (I). J. Meteor.
    Soc. Japan, 48, 173-184.

Gambo, K., 1976: The instability of medium-scale disturb-
    ances in a moist atmosphere. J. Meteor. Soc. Japan, 54,
    191-207.

Harley, D. G., 1960: Frontal contour analysis of a "polar"
    low. Meteor. Mag., 89, 146-147.

Khakimov, I. R., 1976: The wind profile of the neutrally
    stratified atmospheric boundary layer. Atmos. Ocean
    Phys., 12, 628-630.

Kuo, H. L., 1965: On formation and intensification of
    tropical cyclones through latent heat release by cumulus
    convection. J. Atmos. Sci., 22, 40-63.

Lau, N. C., 1978: On the three-dimensional structure of the
    observed transient eddy statistics of the Northern
    Hemisphere wintertime circulation. J. Atmos. Sci., 35,
    1900-1923.

Locatelli, J. D., P. V. Hobbs, and J. A. Werth, 1982:
    Mesoscale structures of vorticities in polar air streams.
    Mon. Wea. Rev., 110, 1417-1433.

London, J., 1957: A study of the atmospheric heat balance.
    Final report, contract AF 19(122)-165, Dept. of
    Meteorology and Oceanography, New York University.

Lorenz, E. N., 1955: Available potential energy and the
    maintenance of the general circulation. Tellus, 7,
    157-167.

Lyall, I. T., 1972: The polar low over Britain. Weather, 27, 378-390.

Madala, R., 1981: Finite difference techniques for vectorized Fluid dynamic calculation, New York, Springer-Verlag , 226pp.

Mansfield, D. A., 1974: Polar lows: the development of baroclinic disturbances in cold air outbreaks. Quart. J. R. Meteor. Soc., 100, 541-554.

Mullen, S. L., 1979: An investigation of small synoptic-scale cyclones in polar air streams. Mon. Wea. Rev., 107, 1636-1647.

Mullen, S. L., 1982: Cyclone development in polar air streams over the wintertime continent. Mon. Wea. Rev., 110, 1664-1676.

Mullen, S. L., 1983: Explosive cyclogenesis associated with cyclones in polar air streams. Mon. Wea. Rev., 111, 1537-1553.

Nieustadt, F. T. M., and H. Tennekes, 1981: A rate equation for the nocturnal boundary layer height. J. Atmos. Sci., 38, 1418-1428.

Orlanski, I., 1968: Instability of frontal waves. J. Atmos. Sci., 25, 178-200.

Petterssen, S., 1956: Weather analysis and forecasting, Vol. I, Motion and motion systems., New York, McGraw-Hill, 428pp.

Phillips, N. A., 1957: A coordinate system having some special advantages for numerical forecasting. J. Meteor., 14, 184-185.

Rao, V. B., and N. J. Ferreira, 1979: Stability properties of medium scale disturbances in a balance model. Instituto de Pesquisas Espaciais, Conselho Nacional de Desenvolimento Cientifico e Technologico, Sao Paulo, Brasil. 20pp.

Rasmussen, E., 1979: The polar low as an extratropical CISK disturbance. Quart. J. R. Meteor. Soc., 105, 531-549.

Rasmussen, E., 1981: An investigation of a polar low with a spiral cloud structure. J. Atmos. Sci., 38, 1785-1792.

Reed, R. J., 1979: Cyclogenesis in polar air streams. <u>Mon. Wea. Rev.</u>, 107, 38-52.

Robert, A. J., 1966: The investigation of a low order spectral form of the primitive meteorological equations. <u>J. Meteor. Soc. Japan</u>, Ser. 2, 44, 237-245.

Robertson, F. R., and P. J. Smith, 1983: The impact of model moist processes on the energetics of extratropical cyclones. <u>Mon. Wea. Rev.</u>, 111, 723-744.

Sanders, F., and J. R. Gyakum, 1980: Synoptic-dynamic climatology of the bomb. <u>Mon. Wea. Rev.</u>, 108, 1589-1606.

Sardie, J. M., and T. T. Warner, 1983: On the mechanism for the development of polar lows. <u>Mon. Wea. Rev.</u>, 40, 869-881.

Shapiro, R., 1970: Smoothing, filtering and boundary effects. <u>Rev. Geophys. and Space Phys.</u>, 8, 359-387.

Simons, T. J., 1972: The nonlinear dynamics of cyclone waves. <u>J. Atmos. Sci.</u>, 29, 38-52.

Staley, D. O., and R. L. Gall, 1977: On the wavelength of maximum baroclinic instability. <u>J. Atmos. Sci.</u>, 34, 1679-1688.

Stevenson, C. M., 1968: The snowfalls of early December 1967. <u>Weather</u>, 23, 156-161.

Stone, P. H., 1966: On non-geostrophic baroclinic instability. <u>J. Atmos. Sci.</u>, 23, 390-400.

Stull, R. B., 1976: Mixed-layer depth model based on turbulent energetics. <u>J. Atmos. Sci.</u>, 33, 1268-1278.

Suttie, T. K., 1970: Portrait of a polar low. <u>Weather</u>, 25, 504-506.

Tokioka, T., 1970: Non-geostrophic and non-hydrostatic stability of a baroclinic fluid. <u>J. Meteor. Soc. Japan</u>, 48, 503-520.

INITIAL DISTRIBUTION LIST

No. Copies

1. Defense Technical Information Center   2
    Cameron Station
    Alexandria, VA 22314

2. Library, Code 0142   2
    Naval Postgraduate School
    Monterey, CA 93943-5100

3. Chairman (Code 63Rd)   1
    Department of Meteorology
    Naval Postgraduate School
    Monterey, CA 93943-5100

4. Director   1
    Naval Oceanography Division
    U.S. Naval Observatory
    34th and Massachusetts Ave., NW
    Washington, DC 20390

5. Commander   1
    Naval Oceanography Command
    NSTL Station
    Bay St. Louis, MS 39522

6. Commanding Officer   1
    Fleet Numerical Oceanography Center
    Monterey, CA 93943-5105

7. Commanding Officer   1
    Naval Environmental Prediction Research
       Facility
    Monterey, CA 93943-5106

8. Chief of Naval Research   1
    800 N. Quincy Street
    Arlington, VA 22217

9. Professor R. L. Elsberry (Code 63Es)   1
    Department of Meteorology
    Naval Postgraduate School
    Monterey, CA 93943-5100

10. Professor R. T. Williams (Code 63Wu)   1
    Department of Meteorology
    Naval Postgraduate School
    Monterey, CA 93943-5100

11. Associate Professor C. H. Wash (Code 63Wu)   1
    Department of Meteorology
    Naval Postgraduate School
    Monterey, CA 93943-5100

12. Professor D. Salinas, (Code 69Zc)   1
    Department of Mechanical Engineering
    Naval Postgraduate School
    Monterey, CA 93943-5100

13. Professor F. D. Faulkner, (Code 53Fa)   1
    Department of Meteorology
    Naval Postgraduate School
    Monterey, CA 93943-5100

14. Richard M. Hodur   1
    Naval Environmental Prediction Research
      Facility
    Monterey, CA 93943-5106

15. Professor R. J. Reed   1
    Department of Atmospheric Sciences, AK-40
    University of Washington
    Seattle, WA 98195

16. Steven L. Mullen   1
    National Center for Atmospheric Research
    P.O. Box 3000
    Boulder, CO 80307

17. Dr. E. Rasmussen   1
    University of Copenhagen
    Haraldsgade 6
    DK-2200 Copenhagen N
    Denmark

18. Dr. Hans von Storch   1
    Universitat Hamburg
    Meteorologisches Institut, Bundesstrasse 55
    2000 Hamburg 13, West Germany

19. S. Businger   1
    Department of Atmospheric Sciences, AK-40
    University of Washington
    Seattle, WA 98195

186

20. Dr. F. R. Robertson   1
    NASA George C. Marshall Space Flight
      Center ED-42
    Marshall Space Flight Center, AL 35812

21. Dr. B. Machenhauer   1
    University of Copenhagen
    Haraldsgade 6
    DK-2000 Copenhagen N
    Denmark

22. Professor C. N. K. Mooers (Code 68Mr)   1
    Department of Oceanography
    Naval Postgraduate School
    Monterey, CA 93943-5100

23. Alan Fox   1
    Code 3253
    PACMISTESTCEN
    Pt. Mugu, CA 93042

END

FILMED

6-85

DTIC